Toward precision galaxy clustering in redshift space: the next loop order

Matthew D. Schwartz
Department of Physics, Harvard University

Mikhail M. Ivanov
Center for Theoretical Physics, Massachusetts Institute of Technology

Siddharth Mishra-Sharma
Anthropic

October 1, 2026

This work is preliminary. Some content remains AI-generated and is still being validated.

PRELIMINARY

Abstract

Galaxy surveys draw much cosmological information from mildly nonlinear scales, where clustering admits a loop expansion that current analyses truncate at one loop. The omitted two-loop term sets their scale cuts and is known mostly for matter or in real space. We compute the two-loop power spectrum and the one-loop bispectrum and trispectrum of biased tracers in redshift space on one complete fifth-order operator basis. The redshift-space kernels, derived recursively, reproduce the known fourth-order kernels in exact rational arithmetic. The two-loop power spectrum decomposes by topology into 149 diagrams. One of the two-loop master integrals is a kite with unit powers on non-adjacent lines, which we obtain in closed form. Because the expanded integrands cancel strongly, we integrate each diagram directly in momentum space, in double and extended precision with a stated error, and tabulate 474 angular components. We renormalize by subtracting each integrand's hard-momentum limits. Infrared resummation damps each term according to its loop order and acts inside the one-loop integrals. The one-loop bispectrum has 568 coefficient functions and the one-loop trispectrum, in nine contraction types, has 5209, with stochastic terms for both and counterterms for the bispectrum in the same scheme. We integrate the bispectrum on a triangle grid and all nine trispectrum types on the 2400 parallelogram configurations of the power-spectrum covariance. The three statistics can then be analyzed jointly at a consistent loop order.

Contents

1 Introduction **2**

2 Review of one-loop galaxy clustering in redshift space **4**

3 Bias basis and redshift-space kernels through fifth order **7**

4 Diagrams and classes of the two-loop power spectrum 13

5 Evaluation of the two-loop integrals 16

6 Renormalization at two loops 19

7 Infrared resummation 25

8 Stochastic terms and the full power spectrum model 28

9 The one-loop bispectrum 31

10 The one-loop trispectrum 36

11 Covariance of the power spectrum, bispectrum and trispectrum 43

12 Sizes of the terms at a fiducial point 45

13 Summary and outlook 46

A Notation and conventions 47

B Counterterm operator lists 50

PRELIMINARY

1 Introduction

Much of the cosmological information in a galaxy redshift survey lies in the clustering of galaxies on mildly nonlinear scales. Between the linear regime and, roughly, the scales of halo formation the density modes couple weakly, and the clustering statistics admit a loop expansion whose terms are momentum integrals over perturbative kernels [3, 68]. Because the loop momenta reach scales where the fluid description fails, the expansion is an effective field theory whose counterterms absorb short-distance physics into free coefficients [7, 14]. This expansion describes the matter density, and two further expansions relate it to the observed galaxy density. First, galaxies trace matter through a bias expansion in local operators with scale-independent renormalized coefficients [2, 28, 56, 69]. Second, a galaxy's redshift includes its peculiar velocity, which displaces its inferred position along the line of sight and mixes density and velocity at every order [50, 62].

For biased tracers in redshift space the one-loop theory of the power spectrum and bispectrum is complete. The redshift-space kernels were constructed through third order [61], with full time dependence [30, 43], and the infrared resummation of the baryon acoustic feature is established [49, 70, 73]. In particular, the one-loop power spectrum, with counterterms and stochastic terms, is implemented in public codes [21, 26] and underlies full-shape analyses of spectroscopic samples [16, 23, 26, 48]. The one-loop bispectrum (which needs the fourth-order kernels) was derived in [11, 25, 60] and has since entered full-shape analyses [20, 24, 46]. In these analyses the two-loop term is omitted, and the scale cuts are chosen to keep it below the statistical uncertainty [20, 26, 48]. One-loop fits to simulated galaxy samples at more aggressive cuts recover the fluctuation amplitude with a systematic shift, which may come from the missing two-loop term [15].

The two-loop matter power spectrum was computed in the effective theory in [6, 13, 18, 53] and with full time and scale dependence in [36, 37]. Once the linear spectrum is decomposed into power laws [71], the loop integrals reduce to master integrals of the massless two-point family, almost all of which are known in closed form through integration by parts and the Gegenbauer polynomial technique [39, 52]. The one two-loop family that the power spectrum requires and that these methods leave unsolved, with unit powers on two non-adjacent lines, has series representations [10, 27, 55, 71]. Taule and Garny extended the two-loop calculation to redshift space with a recursion for the kernels at any order [74]. They also found the expansion to be valid only up to $k \approx 0.2\,h\,\mathrm{Mpc}^{-1}$, where virialized line-of-sight motions (the fingers-of-God effect) become nonperturbative at any loop order. For biased tracers in real space, the bias expansion complete through fifth order has 29 independent operators, of which 17 remain in the renormalized two-loop power spectrum [29, 47, 59, 67]. The two-loop bias renormalization was done by subtraction on the integrands [47] and by the renormalization group [59]. Bakx et al. [5] studied the renormalization of the one-loop bispectrum and trispectrum at fifth order, again in real space. The one-loop matter trispectrum and the non-Gaussian power spectrum covariance it generates are known in real space [8, 9, 72]. In redshift space the galaxy trispectrum has been used at tree level, in the connected covariance of the power spectrum multipoles [51, 65, 66, 75] and, integrated over quadrilateral bins, as an observable in joint analyses with the power spectrum and bispectrum [40, 42].

To our knowledge, however, no calculation gives, in redshift space and on one operator basis, the two-loop galaxy power spectrum together with the one-loop bispectrum and trispectrum. In redshift space the galaxy kernels are known through fourth order on the basis truncated to the one-loop bispectrum operators [11, 25, 60], whereas the two-loop power spectrum needs the fifth-order kernel on the complete basis. Moreover, a joint analysis requires one basis, on which every bias coefficient has the same meaning in all three statistics, and an infrared resummation consistent at each loop order. Each loop integral must also carry a known numerical error, because the two-loop term itself may amount to only a few percent of the power spectrum.

In this paper we construct the two-loop power spectrum and the one-loop bispectrum and trispectrum of biased tracers in redshift space, and evaluate the loop integrals tabulated here. All three statistics share one operator basis complete through fifth order, and the power spectrum and bispectrum share one infrared resummation. On this basis we derive the kernels $Z_1, \ldots, Z_5$ recursively. The deterministic two-loop power spectrum then decomposes into 149 diagrams, classified by topology and by their pair of bias or velocity couplings. Because the diagrams, and the terms within each, cancel strongly, we evaluate every tabulated component (474 in all, 410 nonzero) by direct momentum-space quadrature in double and extended precision and state its numerical error. For the one family of two-loop master integrals known only through series we derive, from its Gegenbauer-series representation [27], a closed form at $d = 3$ in Gamma functions and hypergeometric values at unit argument, complete except for two single sums (Section 5 and the Supplementary Information, Sec. S3). We give the two-loop renormalization conditions in redshift space, with the contact (tadpole) subtractions of the self-looped kernels. The infrared resummation damps each term by a factor set by its loop order, applied inside the loop integrals for the one-loop terms. The power spectrum model then has 20 deterministic and four stochastic parameters, plus the two-loop counterterm coefficients. Two of our expressions differ from printed results: a parity-odd term in one bispectrum counterterm [60] and the Poisson value of one trispectrum shot-noise amplitude [11].

We assemble the one-loop bispectrum in the same scheme as the power spectrum. Its countert-

PRELIMINARY

erms span the contact space of [11] with more free coefficients, its self-loop tadpoles are removed by the power spectrum conditions alone, and we bin-average its tree-level term exactly. The one-loop trispectrum involves 24 of the 29 bias operators and resolves into nine contraction types, which follow from the five partitions of kernel orders. We subtract the contact contributions of its self-looped kernels and dress its tree topologies with stochastic terms in four classes; its counterterms are left to future work [47]. We evaluate the nine types on the 2400 parallelogram configurations of the power spectrum covariance, and three of them on the binned general quadrilaterals of the trispectrum estimator. Finally, we give the trispectrum contribution to the power spectrum covariance (summed here for two of the nine types), the bispectrum–power-spectrum cross block, and the sizes of the evaluated terms at one fiducial point.

The numerical implementation of these expressions, the likelihood built on them and their tests on simulations are described in the companion paper, Paper II [22]; the application to survey data is left to future work. Explicit kernels, the diagram-by-diagram enumeration, integrands, subtraction terms and the evaluated components with their errors are collected in the Supplementary Information, Secs. S1–S8. The machine-readable tables and the code that evaluates the loop integrals will be released with the final version of this paper.

This paper is organized as follows. Section 2 reviews the one-loop theory and fixes notation. In Sections 3–8 we build the two-loop power spectrum: basis and kernels, diagram classes, evaluation, renormalization, infrared resummation, and the stochastic terms with the assembled model of Eq. (8.9). Sections 9 and 10 contain the one-loop bispectrum and trispectrum, Section 11 the covariance expressions and Section 12 the sizes of the terms at the fiducial point. In Section 13 we summarize the results and open problems, and the appendices collect notation, the fiducial parameters and the counterterms of the power spectrum and bispectrum.

2 Review of one-loop galaxy clustering in redshift space

We review the one-loop model of galaxy clustering in redshift space, Eq. (2.16) below, fixing notation. We present no new results in this section.

2.1 Kernels, bias operators and the redshift-space map

The power spectrum $P(k)$ of the matter density contrast $\delta(\mathbf{x},\tau) = \rho(\mathbf{x},\tau)/\bar{\rho}(\tau) - 1$ is defined by

$$\langle \delta(\mathbf{k})\, \delta(\mathbf{k}') \rangle = (2\pi)^3\, \delta_D(\mathbf{k}+\mathbf{k}')\, P(k)\,. \tag{2.1}$$

In standard perturbation theory (SPT) the pressureless-fluid equations for cold dark matter are solved order by order in the linear field δ_1, whose spectrum is $P_{\rm lin}$ [3, 35, 54]. With growth factor D, growth rate $f = d\ln D/d\ln a$ and scaled velocity divergence $\theta \equiv -\nabla\cdot\mathbf{v}/(aHf)$, the solutions read

$$\delta(\mathbf{k},\tau) = \sum_{n\geq 1} D^n(\tau)\, \delta_n(\mathbf{k})\,, \qquad \delta_n(\mathbf{k}) = \int_{\mathbf{q}_1\cdots\mathbf{q}_n}^{\mathbf{k}} F_n(\mathbf{q}_1,\ldots,\mathbf{q}_n)\, \delta_1(\mathbf{q}_1)\cdots\delta_1(\mathbf{q}_n)\,, \tag{2.2}$$

$$\theta(\mathbf{k},\tau) = \sum_{n\geq 1} D^n(\tau)\, \theta_n(\mathbf{k})\,, \qquad \theta_n(\mathbf{k}) = \int_{\mathbf{q}_1\cdots\mathbf{q}_n}^{\mathbf{k}} G_n(\mathbf{q}_1,\ldots,\mathbf{q}_n)\, \delta_1(\mathbf{q}_1)\cdots\delta_1(\mathbf{q}_n)\,, \tag{2.3}$$

PRELIMINARY

where the n momenta sum to $\mathbf{k}$, $\int_{\mathbf{q}} \equiv \int d^3q/(2\pi)^3$, and $\theta_1 = \delta_1$. The D^n scaling of the nth-order terms is the Einstein–de Sitter (EdS) approximation, standard in one-loop analyses [21, 26, 47], with known corrections at one and two loops [30, 37, 74]. We adopt the EdS kernels, with f inside a loop fixed at the redshift of evaluation. For $n \geq 2$, with $F_1 = G_1 = 1$, the kernels follow from the recursion [3, 35]

$$F_n(\mathbf{q}_1,\ldots,\mathbf{q}_n) = \sum_{m=1}^{n-1} \frac{G_m(\mathbf{q}_1,\ldots,\mathbf{q}_m)}{(2n+3)(n-1)} \Big[(2n+1)\,\alpha(\mathbf{k}_1,\mathbf{k}_2)\,F_{n-m}(\mathbf{q}_{m+1},\ldots,\mathbf{q}_n) + 2\,\beta(\mathbf{k}_1,\mathbf{k}_2)\,G_{n-m}(\mathbf{q}_{m+1},\ldots,\mathbf{q}_n)\Big]\,, \tag{2.4}$$

$$G_n(\mathbf{q}_1,\ldots,\mathbf{q}_n) = \sum_{m=1}^{n-1} \frac{G_m(\mathbf{q}_1,\ldots,\mathbf{q}_m)}{(2n+3)(n-1)} \Big[3\,\alpha(\mathbf{k}_1,\mathbf{k}_2)\,F_{n-m}(\mathbf{q}_{m+1},\ldots,\mathbf{q}_n) + 2n\,\beta(\mathbf{k}_1,\mathbf{k}_2)\,G_{n-m}(\mathbf{q}_{m+1},\ldots,\mathbf{q}_n)\Big]\,, \tag{2.5}$$

where $\mathbf{k}_1 = \mathbf{q}_1 + \cdots + \mathbf{q}_m$, $\mathbf{k}_2 = \mathbf{q}_{m+1} + \cdots + \mathbf{q}_n$, $\alpha(\mathbf{k}_1,\mathbf{k}_2) = 1 + \mathbf{k}_1\cdot\mathbf{k}_2/k_1^2$ and $\beta(\mathbf{k}_1,\mathbf{k}_2) = (\mathbf{k}_1+\mathbf{k}_2)^2\,(\mathbf{k}_1\cdot\mathbf{k}_2)/(2\,k_1^2\,k_2^2)$. We use symmetrized kernels throughout.

In the plane-parallel approximation with line of sight $\hat{\mathbf{z}}$, peculiar velocities $\mathbf{v}$ map positions $\mathbf{x}$ to [50, 62, 74]

$$\mathbf{s} = \mathbf{x} + \frac{\mathbf{v}\cdot\hat{\mathbf{z}}}{aH}\,\hat{\mathbf{z}} \;=\; \mathbf{x} - f\,u_z\,\hat{\mathbf{z}}\,, \qquad \mathbf{u} \equiv -\frac{\mathbf{v}}{aHf}\,, \tag{2.6}$$

with $\theta = \nabla\cdot\mathbf{u}$. Mass conservation gives the redshift-space density contrast exactly [3, 62],

$$\delta_s(\mathbf{k}) = \int d^3x\; e^{-i\mathbf{k}\cdot\mathbf{x}}\; e^{\,ifk_z u_z(\mathbf{x})}\,[\delta(\mathbf{x}) + f\,\nabla_z u_z(\mathbf{x})]\,, \tag{2.7}$$

valid while $f\,\nabla_z u_z < 1$. Expanding in δ and θ (at fixed redshift, growth factors absorbed into δ_1), we obtain the redshift-space kernels Z_n,

$$\delta_s(\mathbf{k}) = \sum_{n\geq 1} \int_{\mathbf{q}_1\cdots\mathbf{q}_n}^{\mathbf{k}} Z_n(\mathbf{q}_1,\ldots,\mathbf{q}_n)\,\delta_1(\mathbf{q}_1)\cdots\delta_1(\mathbf{q}_n)\,, \tag{2.8}$$

which are polynomials in f, $\mu = \hat{\mathbf{k}}\cdot\hat{\mathbf{z}}$ and $\mu_i = \hat{\mathbf{q}}_i\cdot\hat{\mathbf{z}}$. The lowest-order kernels are [50, 61, 62]

$$Z_1(\mathbf{q}_1) = 1 + f\mu^2\,, \tag{2.9}$$

$$Z_2(\mathbf{q}_1,\mathbf{q}_2) = F_2(\mathbf{q}_1,\mathbf{q}_2) + f\mu^2\,G_2(\mathbf{q}_1,\mathbf{q}_2) + \frac{f\mu k}{2}\left[\frac{\mu_1}{q_1}\big(1+f\mu_2^2\big) + \frac{\mu_2}{q_2}\big(1+f\mu_1^2\big)\right], \tag{2.10}$$

while Z_3 is given in [21, 61].

Galaxies are biased tracers of matter: the galaxy density contrast is expanded in all operators allowed by the symmetries, each with a free coefficient [2, 28, 56, 69],

$$\delta_g(\mathbf{x},\tau) = \sum_a b_a(\tau)\,O_a(\mathbf{x},\tau)\,. \tag{2.11}$$

Through second order these are δ, δ^2 and the tidal operator $\mathcal{G}_2$, with coefficients b_1, $b_2/2$ and γ_2 [2, 21]. Composite operators must be renormalized [2, 56, 69]. Inside a loop δ^2 contains a contact

PRELIMINARY

term, proportional to the cutoff-dependent variance $\sigma^2(\Lambda) \equiv \int_{\mathbf{q}}^{\Lambda} P_{\rm lin}(q)$, that shifts b_1. Hence we expand in renormalized operators such as $[\delta^2] = \delta^2 - \sigma^2$, whose coefficients are the physical, cutoff-independent parameters [2, 67]. With δ the SPT solution, the expansion defines real-space galaxy kernels K_n analogous to F_n, with $K_1 = b_1$. Substituting δ_g for δ in Eq. (2.7), with the velocity factors still built from G_n, we obtain the galaxy kernels $Z_n^{\rm gal}$, given through third order in [21, 26, 61], with $Z_1^{\rm gal} = b_1 + f\mu^2$.

2.2 Counterterms, infrared resummation and the one-loop model

For Gaussian initial conditions the power spectrum has the loop expansion

$$P(k) = P_{\rm lin}(k) + P_{\text{1-loop}}(k) + P_{\text{2-loop}}(k) + \cdots . \tag{2.12}$$

The one-loop term is the sum of two integrals over one loop momentum,

$$P_{\text{1-loop}} = P_{22} + P_{13}\,, \qquad \begin{aligned} P_{22}(k) &= 2\int_{\mathbf{q}} [F_2(\mathbf{q}, \mathbf{k}-\mathbf{q})]^2\, P_{\rm lin}(q)\, P_{\rm lin}(|\mathbf{k}-\mathbf{q}|)\,, \\ P_{13}(k) &= 6\, P_{\rm lin}(k) \int_{\mathbf{q}} F_3(\mathbf{k}, \mathbf{q}, -\mathbf{q})\, P_{\rm lin}(q)\,, \end{aligned} \tag{2.13}$$

where the prefactors 2 and 6 count the pairings [3, 35, 54, 68]. The loop integrals extend to short scales on which dark matter is not a single-valued fluid. In the effective field theory the contribution of these scales is absorbed into counterterms with free coefficients [7, 14]. Because the kernels fall as k^2/p^2 when two arguments $\pm\mathbf{p}$ become hard, the leading counterterm to P_{13} is an effective sound-speed term of shape $k^2 P_{\rm lin}(k)$ [7, 13]. The velocity products of the redshift-space map require further counterterms [61, 70]: at order k^2, one coefficient c_{2m} per even power μ^{2m} through μ^4 [21, 61].

A long-wavelength displacement moves all points together and cannot alter an equal-time correlator, so the infrared-enhanced parts of P_{22} and P_{13} cancel in their sum [13, 53, 68]. This cancellation fails for the relative displacement of two points separated by the sound horizon; that displacement damps the baryon acoustic oscillations, and its effect is resummed [49, 70, 73]. We split the linear spectrum into a smooth part and an oscillatory remainder,

$$P_{\rm lin}(k) = P_{\rm nw}(k) + P_{\rm w}(k)\,, \tag{2.14}$$

and write $P_X^{\rm w} \equiv P_X[P_{\rm lin}] - P_X[P_{\rm nw}]$ for the wiggly part of any term X. The resummed one-loop redshift-space spectrum is then [21, 49, 73]

$$P^{s,\rm IR}(k,\mu) = P^s_{\rm tree}[P_{\rm nw}] + P^s_{\text{1-loop}}[P_{\rm nw}] + \left(1 + k^2\Sigma^2_{\rm tot}\right) e^{-k^2\Sigma^2_{\rm tot}}\, P^{s,\rm w}_{\rm tree} + e^{-k^2\Sigma^2_{\rm tot}}\, P^{s,\rm w}_{\text{1-loop}}\,, \tag{2.15}$$

where $\Sigma^2_{\rm tot}(z,\mu)$ is the anisotropic damping function of Ref. [49] (the line-of-sight-weighted variance of the relative displacement across the sound horizon). We write the two damping factors as $D_0^{(1)}(x) = (1+x)\, e^{-x}$ and $D_1^{(1)}(x) = e^{-x}$ with $x = k^2\Sigma^2_{\rm tot}(z,\mu)$. They are the $N = 1$ members of a family $D_n^{(N)}$ in which N is the loop order of the calculation and n that of the damped term [49, 73].

Finally, discrete tracers add a stochastic component uncorrelated with the long-wavelength fields [28, 61]. At one loop its spectrum $P_{\rm stoch}$ is a constant plus k^2 and $k^2\mu^2$ terms [21, 48], which we extend to two-loop order in Eq. (8.2); it is not resummed. Thus, inserting galaxy kernels in

PRELIMINARY

Eq. (2.13) and adding counterterms and $P_{\rm stoch}$ gives the one-loop galaxy power spectrum in redshift space [21, 26, 61]

$$\begin{aligned} P_{gg}^{s,\text{1-loop}}(k,\mu) \;&= \big(b_1 + f\mu^2\big)^2 P_{\rm lin}(k) + 2\int_{\mathbf{q}} \big[Z_2^{\rm gal}(\mathbf{k}-\mathbf{q},\mathbf{q})\big]^2 P_{\rm lin}(|\mathbf{k}-\mathbf{q}|)\, P_{\rm lin}(q) \\ &\quad + 6\,\big(b_1 + f\mu^2\big)\, P_{\rm lin}(k) \int_{\mathbf{q}} Z_3^{\rm gal}(\mathbf{k},\mathbf{q},-\mathbf{q})\, P_{\rm lin}(q) \\ &\quad + \sum_{m=0}^{2} c_{2m}\,\mu^{2m}\,k^2 P_{\rm lin}(k) + P_{\rm stoch}(k,\mu)\,, \end{aligned} \tag{2.16}$$

where $P_{\rm lin}$ is taken at the redshift of evaluation. Two operations are implicit in this expression. First, renormalizing the P_{13}-type integral moves its $k^2 P_{\rm lin}$-shaped cutoff dependence into the c_{2m} and leaves the cubic couplings only in the combination b_{Γ_3} of [2, 21]. Second, each term is resummed as in Eq. (2.15), with $D_0^{(1)}$ on the wiggly tree part and $D_1^{(1)}$ on the wiggly loop parts. In this paper we replace the c_{2m} terms with the weighted form $2(b_1+f\mu^2)(c_0+c_2\mu^2+c_4\mu^4)\,k^2 P_{\rm lin}$ of Eq. (6.4), which extends to μ^6 with the three coefficients c_0, c_2, c_4.

With Legendre polynomials $\mathcal{P}_\ell$, the multipoles are

$$P_\ell(k) = \frac{2\ell+1}{2}\int_{-1}^{1} d\mu\; \mathcal{P}_\ell(\mu)\; P^s(k,\mu)\,. \tag{2.17}$$

In forming them we evaluate each overall power f^a multiplying μ^{2m} as $f(k,z)^a$ from the linear Boltzmann solution, including the scale dependence induced by massive neutrinos [31, 34]. The free parameters at fixed cosmology are then b_1, b_2, γ_2 and one cubic coupling, plus the c_{2m} and the stochastic amplitudes $P_{\rm shot}$, a_0, a_2. Up to normalization conventions, this is the model implemented in `CLASS-PT` [21] and `PyBird` [26] and used in related one-loop treatments [30, 34, 61]. We extend each term of Eq. (2.16) by one loop order in the remaining sections and apply the same construction to the three- and four-point functions.

3 Bias basis and redshift-space kernels through fifth order

The two-loop power spectrum and the one-loop trispectrum involve the galaxy kernels through fifth order, and the one-loop bispectrum through fourth order. We construct the redshift-space galaxy kernels $Z_1^{\rm gal}$ to $Z_5^{\rm gal}$ on the complete fifth-order operator basis of [47]. Through fourth order they agree with the published redshift-space kernel of [11] on its truncated basis and with the γ_{31} structure of [46, 60].

3.1 Operator basis through fifth order

We expand the galaxy overdensity, $\delta_g(\mathbf{k}) = \sum_a b_a\, O_a(\mathbf{k})$ [2, 28, 56, 69], on the hybrid Eulerian and Lagrangian basis of [47]. Local-evolution (LE) operators are Eulerian, built from the nonlinear density δ and the velocity potential Φ_v through the Galileons

$$\begin{aligned} \mathcal{G}_2(\Phi_v) &= (\partial_i\partial_j\Phi_v)^2 - (\nabla^2\Phi_v)^2\,, \\ \mathcal{G}_3(\Phi_v) &= 6\det(\partial_i\partial_j\Phi_v) = (\nabla^2\Phi_v)^3 - 3\,\nabla^2\Phi_v\,(\partial_i\partial_j\Phi_v)^2 + 2\,(\partial_i\partial_j\Phi_v)^3\,, \end{aligned} \tag{3.1}$$

PRELIMINARY

whose argument we suppress when it is Φ_v. Non-local-evolution (NLE) operators are Lagrangian Galileons of the Lagrangian perturbation theory (LPT) displacements $\Psi^{(n)} = -\nabla\varphi_n + \nabla\times\mathbf{A}_n$ and their scalar potentials φ_n [32]. The lowest-order NLE operator is

$$\mathcal{G}_2(\varphi_2,\varphi_1) = (\partial_i\partial_j\varphi_2)(\partial_i\partial_j\varphi_1) - (\nabla^2\varphi_2)(\nabla^2\varphi_1)\,, \qquad \nabla^2\varphi_2 = -\mathcal{G}_2(\varphi_1)\,. \tag{3.2}$$

In Fourier space the Galileons reduce to the kernels

$$\mathcal{K}(\mathbf{q}_1,\mathbf{q}_2) = x_{12}^2 - 1\,, \qquad \mathcal{L}(\mathbf{q}_1,\mathbf{q}_2,\mathbf{q}_3) = 1 - x_{12}^2 - x_{23}^2 - x_{31}^2 + 2\,x_{12}\,x_{23}\,x_{31}\,, \tag{3.3}$$

where $x_{ij} = \hat{\mathbf{q}}_i\cdot\hat{\mathbf{q}}_j$. Both vanish when their arguments sum to zero. Through cubic order the expansion reads

$$\delta_g\big|_{\mathcal{O}(\delta^3)} = b_1\,\delta + \frac{b_2}{2}\,\delta^2 + \gamma_2\,\mathcal{G}_2 + \frac{b_3}{6}\,\delta^3 + \gamma_2^\times\,\delta\,\mathcal{G}_2 + \gamma_3\,\mathcal{G}_3 + \gamma_{21}\,\mathcal{G}_2(\varphi_2,\varphi_1)\,. \tag{3.4}$$

We name the coefficients with one $\times$ per extra factor of δ and subscripts giving the LPT orders of the Galileon arguments, as in $\gamma_{31} \leftrightarrow \mathcal{G}_2(\Psi^{(3)},\Psi^{(1)})$. The coefficients b_1, b_2 and $\gamma_2 = b_{\mathcal{G}_2}$ equal their `CLASS-PT` counterparts [21]. The cubic `CLASS-PT` operator $\Gamma_3 = \mathcal{G}_2(\Phi_\delta) - \mathcal{G}_2(\Phi_v)$, with $\nabla^2\Phi_\delta = \delta$, has $-\frac{4}{7}$ times the kernel $K^{(3)}_{\gamma_{21}}$ given below, and $b_{\mathcal{G}_2}$ there multiplies $\mathcal{G}_2(\Phi_\delta) = \mathcal{G}_2(\Phi_v) + \Gamma_3$, so that

$$\gamma_{21} \;=\; -\tfrac{4}{7}\left(b_{\mathcal{G}_2} + b_{\Gamma_3}\right), \qquad b_{\Gamma_3} \;=\; -\tfrac{7}{4}\,\gamma_{21} - b_{\mathcal{G}_2}\,. \tag{3.5}$$

The dictionary to other bases is given in Appendix A.

Eight operators are new at fourth order, four LE and four NLE, and fourteen at fifth: five LE, five NLE products of lower operators with δ_L or with $\mathcal{G}_2(\Phi_v)$, and four new NLE Galileons of $\Psi^{(3)}$ and $\Psi^{(4)}$. The 29 operators (Table 1) [29, 59, 67] are linearly independent at each order [47] and agree with the basis of [59]. We obtain the momentum-space kernels by evolving the LE operators in standard perturbation theory and advecting the NLE operators to the Eulerian frame through second order in the displacement [47]. Complete fifth-order kernels for this basis were given earlier in [29, 59]. Below, $\sum_n$ runs over the n distinct assignments of momenta to the summand's labels, $\mathbf{q}_{ab} = \mathbf{q}_a + \mathbf{q}_b$, $\bar{\mathbf{q}}_i$ is the argument list with $\mathbf{q}_i$ removed and $\mathbf{q}_{\bar{\imath}}$ its sum. The quadratic and cubic kernels are

$$K_2(\mathbf{q}_1,\mathbf{q}_2) = b_1\,F_2(\mathbf{q}_1,\mathbf{q}_2) + \frac{b_2}{2} + \gamma_2\,\mathcal{K}(\mathbf{q}_1,\mathbf{q}_2)\,, \tag{3.6}$$

$$\begin{aligned} K_3(\mathbf{q}_1,\mathbf{q}_2,\mathbf{q}_3) = {} & \underbrace{\frac{b_3}{6} + \frac{\gamma_2^\times}{3}\sum_3 \mathcal{K}(\mathbf{q}_a,\mathbf{q}_b) + \gamma_3\,\mathcal{L}(\mathbf{q}_1,\mathbf{q}_2,\mathbf{q}_3)}_{K^{(3)}_{\rm LE}[b_3,\gamma_2^\times,\gamma_3]} + \underbrace{\gamma_{21}\,K^{(3)}_{\gamma_{21}}(\mathbf{q}_1,\mathbf{q}_2,\mathbf{q}_3)}_{K^{(3)}_{\rm NLE}[\gamma_{21}]} \\ & \underbrace{+\,b_1\,F_3(\mathbf{q}_1,\mathbf{q}_2,\mathbf{q}_3) + \frac{b_2}{3}\sum_3 F_2(\mathbf{q}_a,\mathbf{q}_b) + \frac{2\gamma_2}{3}\sum_3 \mathcal{K}(\mathbf{q}_a,\mathbf{q}_{bc})\,G_2(\mathbf{q}_b,\mathbf{q}_c)}_{K^{(3)}_{\rm evolved}[b_1,b_2,\gamma_2]}\,, \end{aligned} \tag{3.7}$$

where the NLE kernel multiplying γ_{21} is

$$K^{(3)}_{\gamma_{21}}(\mathbf{q}_1,\mathbf{q}_2,\mathbf{q}_3) = \frac{1}{3}\sum_3 \mathcal{K}(\mathbf{q}_a,\mathbf{q}_{bc})\,\mathcal{K}(\mathbf{q}_b,\mathbf{q}_c)\,. \tag{3.8}$$

PRELIMINARY

order	coefficient	operator	type	in $\Delta P_{gg}^{\text{2-loop}}$
1	b_1	δ	LE	yes
2	b_2	$\delta^2/2$	LE	yes
	γ_2	$\mathcal{G}_2$	LE	yes
3	b_3	$\delta^3/6$	LE	yes
	$\gamma_2^\times$	$\delta\,\mathcal{G}_2$	LE	yes
	γ_3	$\mathcal{G}_3$	LE	yes
	γ_{21}	$\mathcal{G}_2(\varphi_2,\varphi_1)$	NLE	yes
4	b_4	$\delta^4/24$	LE	no
	$\gamma_2^{\times\times}$	$\delta^2\,\mathcal{G}_2/2$	LE	no
	$\gamma_3^\times$	$\delta\,\mathcal{G}_3$	LE	no
	γ_2^{sq}	$\mathcal{G}_2^2/2$	LE	no
	$\gamma_{21}^\times$	$\delta\,\mathcal{G}_2(\varphi_2,\varphi_1)$	NLE	yes
	γ_{211}	$\mathcal{G}_3(\varphi_2,\varphi_1,\varphi_1)$	NLE	yes
	γ_{22}	$\mathcal{G}_2(\varphi_2,\varphi_2)$	NLE	yes
	γ_{31}	$\mathcal{G}_2(\Psi^{(3)},\Psi^{(1)})$	NLE	yes
5	b_5	$\delta^5/5!$	LE	no
	$\gamma_2^{\times\times\times}$	$\delta^3\,\mathcal{G}_2/6$	LE	no
	$\gamma_3^{\times\times}$	$\delta^2\,\mathcal{G}_3/2$	LE	no
	$\gamma_2^{\text{sq}\times}$	$\delta\,\mathcal{G}_2^2/2$	LE	no
	$b_{\mathcal{G}_2\mathcal{G}_3}$	$\mathcal{G}_2\,\mathcal{G}_3$	LE	no
	$\gamma_{21}^{\times\times}$	$\delta_L^2\,\mathcal{G}_2(\varphi_2,\varphi_1)$	NLE	no
	$\gamma_{21,2}$	$\mathcal{G}_2(\Phi_v)\,\mathcal{G}_2(\varphi_2,\varphi_1)$	NLE	no
	$\gamma_{211}^\times$	$\delta_L\,\mathcal{G}_3(\varphi_2,\varphi_1,\varphi_1)$	NLE	no
	$\gamma_{22}^\times$	$\delta_L\,\mathcal{G}_2(\varphi_2,\varphi_2)$	NLE	yes
	$\gamma_{31}^\times$	$\delta_L\,\mathcal{G}_2(\Psi^{(3)},\Psi^{(1)})$	NLE	yes
	γ_{23}	$\mathcal{G}_2(\Psi^{(3)},\Psi^{(2)})$	NLE	yes
	γ_{221}	$\mathcal{G}_3(\varphi_2,\varphi_2,\varphi_1)$	NLE	yes
	γ_{311}	$\mathcal{G}_3(\Psi^{(3)},\Psi^{(1)},\Psi^{(1)})$	NLE	yes
	γ_{41}	$\mathcal{G}_2(\Psi^{(4)},\Psi^{(1)})$	NLE	yes

Table 1: The bias basis through fifth order: 29 operators with their coefficients and their LE (local evolution, Eulerian) or NLE (non-local evolution, Lagrangian) type, following [47], eqs. (11), (34) and (38)–(40). The 17 operators marked "yes" have free coefficients in the deterministic two-loop power spectrum after renormalization and form the vector of Eq. (3.24); the 12 marked "no" are redundant there. δ_L is the linear density, Φ_v the velocity potential, φ_n the n-th order Lagrangian perturbation theory (LPT) potential and $\Psi^{(n)}$ the n-th order displacement; $\gamma_{21}^{\times\times}$ carries no factor $1/2$ (it does in [47]).

The braces separate the new LE and NLE operators from the evolved block, where lower-order bias coefficients multiply nonlinear matter kernels.

At third order the displacement ceases to be purely potential. Its scalar kernel, with the Einstein–de Sitter growth ratios $D_{3a}/D^3 = 1/18$ and $D_{3b}/D^3 = 5/42$ absorbed, is

$$S_3(\mathbf{q}_1,\mathbf{q}_2,\mathbf{q}_3) = \frac{1}{18}\left[-\mathcal{L}(\mathbf{q}_1,\mathbf{q}_2,\mathbf{q}_3) + \frac{15}{7}\,K^{(3)}_{\gamma_{21}}(\mathbf{q}_1,\mathbf{q}_2,\mathbf{q}_3)\right], \tag{3.9}$$

PRELIMINARY

and its transverse part, with ratio $D_{3c}/D^3 = 1/14$, is built on the vector kernel

$$\mathbf{W}(\mathbf{k}_1, \mathbf{k}_2) = \frac{(\mathbf{k}_1 \times \mathbf{k}_2)\,(\mathbf{k}_1 \cdot \mathbf{k}_2)}{k_1^2\, k_2^2} \tag{3.10}$$

as the symmetrized kernel $\mathbf{T}_3(\mathbf{q}_1, \mathbf{q}_2, \mathbf{q}_3) = -\frac{1}{3}\sum_{\rm cyc} \mathbf{W}(\mathbf{q}_i, \mathbf{q}_{jk})\,\mathcal{K}(\mathbf{q}_j, \mathbf{q}_k)/14$. Here S_3 and $\mathbf{T}_3$ are defined in the convention $\Psi^{(n)} = iD^n \int \mathbf{L}_n\, \delta_0^n$, $S_n = \mathbf{k}\cdot\mathbf{L}_n$, $\mathbf{T}_n = -\mathbf{k}\times\mathbf{L}_n$ of [47]. The transverse displacement is a polar vector and enters every Galileon built on $\Psi^{(3)}$ through a contraction of two $\mathbf{W}$ vectors, which is even under $\mathbf{q}_i \to -\mathbf{q}_i$ and does not vanish under the loop integrals. We write the kernel of $\mathcal{G}_2(\Psi^{(3)}, \Psi^{(1)})$ as

$$K^{(4)}_{\gamma 31}(\mathbf{q}_1, \ldots, \mathbf{q}_4) = \frac{1}{4}\sum_4 \mathcal{K}(\mathbf{q}_i, \mathbf{q}_{\bar{i}})\, S_3(\mathbf{q}_j, \mathbf{q}_k, \mathbf{q}_l) + \frac{1}{14}\,\mathcal{S}_{(1,3c)}(\mathbf{q}_1, \ldots, \mathbf{q}_4)\,, \tag{3.11}$$

where $\mathcal{S}_{(1,3c)}$ is the $\mathbf{W}\cdot\mathbf{W}$ structure defined with S_4 below, and the sign of the second term is fixed by the identity $\delta_4 = F_4$. The same $\mathbf{W}\cdot\mathbf{W}$ term completes the $\gamma^{\times}_{31}$ and advected-γ_{31} kernels at fifth order. The kernels K_4 and K_5 contain one leading momentum structure for each new operator, denoted $K^{(4)}_{\gamma^{\times}_{21}}$, $K^{(4)}_{\gamma 211}$, $K^{(4)}_{\gamma 22}$ and $K^{(4)}_{\gamma 31}$ for the fourth-order NLE operators, plus evolved and advected lower-order terms. The full expressions of both kernels, with the replacement rules that add the transverse contributions, are given in the Supplementary Information, Sec. S1.

The fourth-order scalar displacement kernel S_4 enters the basis through $\gamma_{41}\,\mathcal{G}_2(\Psi^{(4)}, \Psi^{(1)})$. Normalized as $S_4 \equiv -4!\,\mathbf{k}\cdot\mathbf{L}_4$ with the factor $-4!$ absorbed in γ_{41} ($\gamma_{41}^{\rm here} = -\gamma_{41}^{\mathbf{k}\cdot\mathbf{L}_4}/24$), it reads

$$\begin{aligned}
S_4(\mathbf{q}_1, \ldots, \mathbf{q}_4) =& -\frac{28}{33}\,\mathcal{S}_{(1,3a)} + \frac{20}{11}\,\mathcal{S}_{(1,3b)} + \frac{153}{539}\,K^{(4)}_{\gamma 22} - \frac{78}{77}\,K^{(4)}_{\gamma 211} + \frac{12}{11}\,\mathcal{S}_{(1,3c)}\,,\\
\mathcal{S}_{(1,3a)} =& \frac{1}{4}\sum_4 \mathcal{K}(\mathbf{q}_i, \mathbf{q}_{\bar{i}})\,\mathcal{L}(\bar{\mathbf{q}}_i)\,, \qquad \mathcal{S}_{(1,3b)} = \frac{1}{4}\sum_4 \mathcal{K}(\mathbf{q}_i, \mathbf{q}_{\bar{i}})\,K^{(3)}_{\gamma 21}(\bar{\mathbf{q}}_i)\,,\\
\mathcal{S}_{(1,3c)} =& -\frac{1}{4!}\sum_{\sigma}\left[\mathbf{W}(\mathbf{q}_{\sigma_1}, \mathbf{q}_{\sigma_2\sigma_3\sigma_4})\cdot\mathbf{W}(\mathbf{q}_{\sigma_2}, \mathbf{q}_{\sigma_3\sigma_4})\right]\mathcal{K}(\mathbf{q}_{\sigma_3}, \mathbf{q}_{\sigma_4})\,,
\end{aligned} \tag{3.12}$$

where σ runs over the 24 permutations of the momenta and

$$\mathbf{W}(\mathbf{k}_a, \mathbf{k}_b)\cdot\mathbf{W}(\mathbf{k}_c, \mathbf{k}_d) = \frac{\left[(\mathbf{k}_a\cdot\mathbf{k}_c)(\mathbf{k}_b\cdot\mathbf{k}_d) - (\mathbf{k}_a\cdot\mathbf{k}_d)(\mathbf{k}_b\cdot\mathbf{k}_c)\right](\mathbf{k}_a\cdot\mathbf{k}_b)(\mathbf{k}_c\cdot\mathbf{k}_d)}{k_a^2\, k_b^2\, k_c^2\, k_d^2}\,. \tag{3.13}$$

The momentum dependence of $\mathcal{S}_{(1,3c)}$ does not occur in products of the lower-order scalar potentials, and we have confirmed the sign of its coefficient by solving the Lagrangian equations directly to fourth order and projecting $\mathbf{k}\cdot\mathbf{L}_4$ onto the five structures of S_4.

3.2 Redshift-space galaxy kernels through fifth order

The redshift-space galaxy kernels $Z_n^{\rm gal}$ are defined by the expansion of Eq. (2.8) with the galaxy contrast δ_g^s in place of δ_s. We generate them by the recursion of [74]. We write $\mu = \hat{\mathbf{k}}\cdot\hat{\mathbf{z}}$, $\mu_i = \hat{\mathbf{q}}_i\cdot\hat{\mathbf{z}}$, $q_{1\cdots m} = |\mathbf{q}_1 + \cdots + \mathbf{q}_m|$ and

$$\mu_{1\cdots m} \;=\; \frac{(\mathbf{q}_1 + \cdots + \mathbf{q}_m)\cdot\hat{\mathbf{z}}}{|\mathbf{q}_1 + \cdots + \mathbf{q}_m|}\,. \tag{3.14}$$

PRELIMINARY

Expanding the redshift-space exponential order by order in δ_1, we obtain Z_n in terms of density blocks A_m and pure-velocity blocks $B_m^{(p)}$,

$$Z_n(\mathbf{q}_1,\ldots,\mathbf{q}_n) \;=\; A_n(\mathbf{q}_1,\ldots,\mathbf{q}_n) \;+\; \sum_{m=1}^{n-1} A_m(\mathbf{q}_1,\ldots,\mathbf{q}_m) \sum_{p=1}^{n-m} \frac{(f\mu k)^p}{p!}\, B_{n-m}^{(p)}(\mathbf{q}_{m+1},\ldots,\mathbf{q}_n)\,, \tag{3.15}$$

averaged over the distinct distributions of the n arguments between the two blocks, where

$$B_m^{(1)} \;=\; \frac{\mu_{1\cdots m}}{|\mathbf{q}_1+\cdots+\mathbf{q}_m|}\, G_m\,, \qquad B_m^{(p)} \;=\; \sum_{l=p-1}^{m-1} B_l^{(p-1)}(\mathbf{q}_1,\ldots,\mathbf{q}_l)\, B_{m-l}^{(1)}(\mathbf{q}_{l+1},\ldots,\mathbf{q}_m)\,, \tag{3.16}$$

with the $B_m^{(p)}$ recursion symmetrized in the same way. For matter $A_m = F_m + f\mu_{1\cdots m}^2\, G_m$; for galaxies the density block carries K_m in place of F_m,

$$A_m^{\rm gal} \;=\; K_m + f\,\mu_{1\cdots m}^2\, G_m\,, \tag{3.17}$$

while every velocity block keeps G_m, because we assume no velocity bias, which at this order should enter through counterterms. We normal-order the bias operators, $\langle\delta_g\rangle = 0$, which in redshift space is a nontrivial condition (Section 6.3).

Through third order we obtain

$$Z_1^{\rm gal}(\mathbf{q}_1) = b_1 + f\mu^2\,, \tag{3.18}$$

$$Z_2^{\rm gal}(\mathbf{q}_1,\mathbf{q}_2) = K_2(\mathbf{q}_1,\mathbf{q}_2) + f\mu^2\, G_2(\mathbf{q}_1,\mathbf{q}_2) + \frac{f\mu k}{2}\left[\frac{\mu_1}{q_1}\big(K_1(q_2)+f\mu_2^2\big) + \frac{\mu_2}{q_2}\big(K_1(q_1)+f\mu_1^2\big)\right],$$

$$K_1(q) = b_1 + c_0\, q^2\,, \tag{3.19}$$

$$\begin{aligned} Z_3^{\rm gal}(\mathbf{q}_1,\mathbf{q}_2,\mathbf{q}_3) &= K_3 + f\mu^2\, G_3 + f\mu k\left[K_2(\mathbf{q}_1,\mathbf{q}_2) + f\mu_{12}^2\, G_2(\mathbf{q}_1,\mathbf{q}_2)\right]\frac{\mu_3}{q_3} \\ &\quad + f\mu k\big(b_1+f\mu_1^2\big)\frac{\mu_{23}}{q_{23}}\, G_2(\mathbf{q}_2,\mathbf{q}_3) + \frac{(f\mu k)^2}{2}\big(b_1+f\mu_1^2\big)\frac{\mu_2}{q_2}\,\frac{\mu_3}{q_3}\,, \end{aligned} \tag{3.20}$$

with the symmetrization of $Z_3^{\rm gal}$ left implied. The linear kernel is the Kaiser factor with linear bias. Besides b_1, the kernel K_1 contains the coefficient $c_0 = -\beta_1$ of the $k^2\delta$ counterterm of Section 6.[1] For $c_0 = 0$ the kernel $Z_2^{\rm gal}$ is that of the one-loop analyses [21, 61]. At fourth and fifth order we obtain

$$Z_4^{\rm gal} = A_4 + f\mu k\left[A_3B_1^{(1)} + A_2B_2^{(1)} + A_1B_3^{(1)}\right] + \frac{(f\mu k)^2}{2}\left[A_2B_2^{(2)} + A_1B_3^{(2)}\right] + \frac{(f\mu k)^3}{6}\, A_1B_3^{(3)}\,, \tag{3.21}$$

$$\begin{aligned} Z_5^{\rm gal} &= A_5 + f\mu k\left[A_4B_1^{(1)} + A_3B_2^{(1)} + A_2B_3^{(1)} + A_1B_4^{(1)}\right] \\ &\quad + \frac{(f\mu k)^2}{2}\left[A_3\,B_2^{(2)} + A_2\,B_3^{(2)} + A_1\,B_4^{(2)}\right] + \frac{(f\mu k)^3}{6}\left[A_2\,B_3^{(3)} + A_1\,B_4^{(3)}\right] + \frac{(f\mu k)^4}{24}\, A_1\,B_4^{(4)}\,, \end{aligned} \tag{3.22}$$

[1] This is not the higher-derivative c_0 of [47].

PRELIMINARY

where $A_m = A_m^{\rm gal}$ takes the first m arguments and the B block the rest, averaged over distributions, and $B_1^{(1)} = \mu_1/q_1$ (explicit forms in the Supplementary Information, Sec. S1).

Every term of $Z_n^{\rm gal}$ contains one density block and is thus linear in the vector $c = (v{=}1, b_1, \ldots, b_{17})$ of the pure-velocity weight v and the 17 bias parameters of Eq. (3.24) below. Hence we write the deterministic two-loop spectrum as the bilinear sum

$$P_{gg}^{s,\text{2-loop}}(k,\mu) \;=\; \sum_{\rm topo} \sum_{i\le j} c_i\, c_j\, P_{\rm topo}^{ij}(k,\mu;f) \tag{3.23}$$

of coefficient-independent integrals over the topologies P_{15}, P_{24}, $P_{33,\rm I}$ and $P_{33,\rm II}$, whose coupling pairs (i,j) are enumerated in Section 4.

Setting $b_1 = 1$ and all other coefficients to zero recovers the matter kernels of [74], and $f = 0$ reduces $Z_n^{\rm gal}$ to K_n. The fourth-order kernel on the basis truncated to the one-loop bispectrum operators has been published [11, 25, 60]. Symmetrized over its four arguments, the kernel of [11] agrees with our $Z_4^{\rm gal}$ in all sixteen bias and velocity couplings, in exact rational arithmetic at three random configurations, which tests only the velocity–bias cross structure since both use the same K_n. The density structure $K_{\gamma 31}^{(4)}$, including the transverse term $+\frac{1}{14}\,\mathcal{S}_{(1,3c)}$, coincides term by term under the 24 permutations of its arguments with the γ_{31} structure of eq. (A.1) of [60] and eq. (A5) of [46], in exact rational arithmetic at twelve generic configurations. The kernel $Z_5^{\rm gal}$ on the complete basis, which combines fifth-order bias with the redshift-space map, has to our knowledge not appeared in the literature. Its velocity–bias couplings follow only from the recursion above and have not been checked against any independent result.

All kernels above assume Einstein–de Sitter growth. We use them throughout with a single growth rate f at each redshift. For the bare two-loop matter spectrum the resulting error reaches roughly one percent at $k \simeq 0.17\,h\,\mathrm{Mpc}^{-1}$ [37]. However, we have not measured the corresponding error for galaxies in redshift space. Beyond this approximation the exact-time factorization of [30, 43] separates each kernel into cosmology-independent shape tensors and growth functions. The shape tensors are time independent, and exact time enters entirely through scalar weights. We treat massive neutrinos in the cb prescription, in which only the cold-dark-matter-plus-baryon field is evolved nonlinearly and bias is defined with respect to it [19]. We thereby omit the back-reaction of neutrino clustering on the kernels, which is suppressed by f_ν and whose size at two loops we do not estimate. The growth equations and the neutrino treatment are given in the Supplementary Information, Sec. S1.

3.3 Parameter vector and renormalized bias parameters

The four fourth-order LE operators are redundant in the two-loop power spectrum. At fifth order the five LE operators, the four evolved fourth-order LE terms and the three NLE products $\gamma_{21}^{\times\times}$, $\gamma_{21,2}$, $\gamma_{211}^{\times}$ give no finite contribution to P_{15}. This leaves 17 free bias parameters, 1/2/4/4/6 order by order, marked "yes" in Table 1. Ordered as in eq. (119) of [47], they form the vector

$$b^i = \big(b_1,\, b_2,\, \gamma_2,\, \gamma_{21},\, b_3,\, \gamma_2^{\times},\, \gamma_3,\, \gamma_{211},\, \gamma_{22},\, \gamma_{31},\, \gamma_{21}^{\times},\, \gamma_{23},\, \gamma_{221},\, \gamma_{311},\, \gamma_{41},\, \gamma_{22}^{\times},\, \gamma_{31}^{\times}\big)\,, \tag{3.24}$$

which fixes the (i,j) shape indices used below. The Π-trace basis of [59] leads to the same seventeen free parameters, its twelve operators of the $(\Pi^{[1]})^5$, $(\Pi^{[1]})^4$ and $(\Pi^{[1]})^3\Pi^{[2]}$ families dropping out after renormalization. The basis of 29 operators assumes bias non-local in time, one independent time

PRELIMINARY

kernel per operator [69], whereas a local-in-time ansatz would tie three fifth-order combinations together [29, 57].

The bias parameters are scheme dependent, because loop corrections to composite operators contain powers of the mass variance that are absorbed into lower-order coefficients,

$$b_O + \delta b_O\, \sigma^2 = b_O^{(R)}\,, \qquad \sigma^2 \equiv \int_{\mathbf{q}} P_{\rm L}(q)\,, \tag{3.25}$$

where the finite remainders $b_O^{(R)}$ are the renormalized parameters, fixed here by the subtractions of Section 6. At one loop the linear-bias condition, used repeatedly below, is

$$\delta b_1 = \frac{b_3}{2} + \frac{34}{21}\, b_2 - \frac{4}{3}\,\gamma_2^{\times}\,. \tag{3.26}$$

At two loops we project the single-hard limit of P_{15} onto the cubic basis, which gives the conditions for δb_3, $\delta\gamma_2^{\times}$, $\delta\gamma_3$ and $\delta\gamma_{21}$ of Section 6.3. We keep γ_{21} and b_3 independent although they are degenerate at one loop, where b_3 enters only through δb_1, and at two loops their $P_{33,\rm II}$ contribution is likewise a pure δb_1 counterterm.

At $f = 0$ Eq. (3.23) reduces to the real-space decomposition $\Delta P_{gg}^{\text{2-loop}}(k) = \sum_{i\le j} b_i\, b_j\, P^{ij}(k)$ with 46 nontrivial shapes for the 17 parameters, each shape summed over the topologies that contain its pair, as in eq. (87) of [47]. Grouped by the highest-order operator in the pair, the shapes split as $10 + 18 + 12 + 6$: pairs within the one-loop set $\{b_1, b_2, \gamma_2, \gamma_{21}\}$, then pairs whose higher operator is third-order, fourth-order NLE and fifth-order NLE. In redshift space the coupling pairs (i, j) run over the 18-component vector c, which includes the pure-velocity entry v. Finally, some operators redundant in the power spectrum acquire free coefficients in the bispectrum and the trispectrum. The one-loop trispectrum involves 24 of the 29 operators, so that seven of the twelve operators redundant in the power spectrum are free there; the remaining five are expected to become physical beyond two loops.

4 Diagrams and classes of the two-loop power spectrum

Our power spectrum model is the one-loop model of Eq. (2.16) plus the deterministic two-loop term of Eq. (3.23), renormalized and resummed as in Sections 6 and 7, and combined with counterterms and stochastic terms in Eq. (8.9). The two-loop term is a sum of 149 diagrams in four topologies, of which 134 are evaluated and nonzero; the rest are identified below.

4.1 Topologies and diagram counts

The deterministic two-loop spectrum is the sum of four topologies, one for each pattern of Wick contractions of six linear fields (Fig. 1). In real space, in the notation of [47] and with the symmetry factors absorbed into the P_{nm} following [68], they read

$$P_{24} = 2\int_{\mathbf{p}} K_2(\mathbf{k}-\mathbf{p},\mathbf{p})\, I^{(4)}(\mathbf{k}-\mathbf{p},\mathbf{p})\, P_{\rm lin}(|\mathbf{k}-\mathbf{p}|)\, P_{\rm lin}(p), \tag{4.1}$$

$$I^{(4)}(\mathbf{k}_1,\mathbf{k}_2) = 12\int_{\mathbf{q}} K_4(\mathbf{k}_1,\mathbf{k}_2,\mathbf{q},-\mathbf{q})\, P_{\rm lin}(q), \tag{4.2}$$

PRELIMINARY

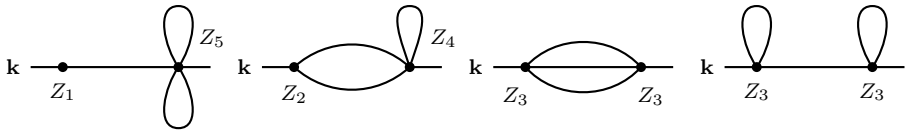

Figure 1: The four topologies of the deterministic two-loop power spectrum, Eqs. (4.1)–(4.5). Each vertex is a kernel, K_n in real space or $Z_n^{\rm gal}$ in redshift space, of the perturbative order in its subscript; each internal line is one linear power spectrum, and the external lines carry $\mathbf{k}$. A closed line on one vertex is a momentum pair $(\mathbf{q}, -\mathbf{q})$ contracted inside one kernel, a tadpole; in P_{24} it is the inner integral $I^{(4)}$, and $P_{33,\mathrm{I}}$ has none. In P_{15} and $P_{33,\mathrm{II}}$ the line joining the vertices is not integrated over and gives the factor $P_{\rm lin}(k)$. Symmetry factors and diagram counts are in Table 2.

$$P_{33,\mathrm{I}} = 6 \int_{\mathbf{p}} \int_{\mathbf{q}} [K_3(\mathbf{k}-\mathbf{p}-\mathbf{q}, \mathbf{p}, \mathbf{q})]^2 \, P_{\rm lin}(|\mathbf{k}-\mathbf{p}-\mathbf{q}|) \, P_{\rm lin}(p) \, P_{\rm lin}(q), \tag{4.3}$$

$$P_{33,\mathrm{II}} = 9 \, P_{\rm lin}(k) \, [\sigma_{13}(k)]^2 \,, \qquad \sigma_{13}(k) = \int_{\mathbf{p}} K_3(\mathbf{k}, \mathbf{p}, -\mathbf{p}) \, P_{\rm lin}(p), \tag{4.4}$$

$$P_{15} = 30 \, b_1 \, P_{\rm lin}(k) \int_{\mathbf{p}} \int_{\mathbf{q}} K_5(\mathbf{k}, \mathbf{p}, -\mathbf{p}, \mathbf{q}, -\mathbf{q}) \, P_{\rm lin}(p) \, P_{\rm lin}(q), \tag{4.5}$$

where K_n are the real-space galaxy kernels, $\int_{\mathbf{p}} = \int d^3p/(2\pi)^3$, and the inner loop $I^{(4)}$ of P_{24} is the loop integral of the one-loop bispectrum term B_{411}. The prefactors count the Wick pairings and agree with [74].

In redshift space the same topologies appear with $Z_n^{\rm gal}$ in place of K_n and unchanged symmetry factors. Each kernel is linear in the coefficient vector $c = (v{=}1, b_1, \ldots, b_{17})$ of Eq. (3.24), and each contribution is an integral $P^{ij}_{\rm topo}(k, \mu; f)$ labeled by a topology and an unordered pair $\{i, j\}$ of entries of c. The two-loop spectrum is their bilinear sum, Eq. (3.23), which at $f = 0$ is the real-space decomposition, eq. (87) of [47]. We call each term of this sum, one topology with one coupling pair, a diagram.

We count the diagrams from the kernels alone. The kernel $Z_n^{\rm gal}$ admits the velocity entry and every operator whose lowest perturbative order is at most n. The sets of admitted couplings are nested: their sizes s_n are 2 for $Z_1^{\rm gal}$ and 4, 8, 12 and 18 for $Z_2^{\rm gal}$ through $Z_5^{\rm gal}$. A topology contracting $Z_a^{\rm gal}$ with $Z_b^{\rm gal}$, $a \le b$, therefore contains $s_a s_b - \binom{s_a}{2}$ unordered pairs: $2 \cdot 18 - 1 = 35$ for P_{15} and $4 \cdot 12 - 6 = 42$ for P_{24}, while each diagonal $Z_3 Z_3$ topology has $\binom{8}{2} + 8 = 36$. Without the velocity entry the sets shrink to 1, 3, 7, 11 and 17 entries, and the same arithmetic gives $17 + 30 + 28 + 28$ real-space diagrams. In all we find 149 diagrams (Table 2), 103 of them present at $f = 0$ and 46 only in redshift space.

4.2 Angular structure and selection rules

Every kernel is a polynomial in the line-of-sight projections μ and $\mu_{1\cdots m}$, and $Z_n^{\rm gal}$ carries at most $2n$ powers of $\hat{\mathbf{z}}$ and n powers of f. Parity under $\hat{\mathbf{z}} \to -\hat{\mathbf{z}}$ with $\mathbf{q}_i \to -\mathbf{q}_i$ removes the odd powers

PRELIMINARY

topology	kernels	symmetry	diagrams	real space ($f = 0$)	redshift space only	identifiers
P_{15}	$Z_1 Z_5$	30	35	17	18	D001–D035
P_{24}	$Z_2 Z_4$	2×12	42	30	12	D036–D077
$P_{33,\mathrm{I}}$	$Z_3 Z_3$	6	36	28	8	D078–D113
$P_{33,\mathrm{II}}$	$Z_3 Z_3$ (tadpole)	9	36	28	8	D114–D149
total			149	103	46	

Table 2: The deterministic two-loop diagrams of the redshift-space galaxy power spectrum by topology. Each topology contracts the two kernels named in the second column, with the symmetry factor of Eqs. (4.1)–(4.5). The diagram column counts the unordered coupling pairs admitted by the two kernels; the next two columns split them into the pairs present at $f = 0$ and the pairs containing at least one velocity entry, which exist only in redshift space. The identifiers number the diagrams topology by topology, within each topology in the order of the coefficient vector c of Eq. (3.24).

of μ, and averaging over loop orientations at fixed $\hat{\mathbf{k}}$ and $\hat{\mathbf{z}}$ we reduce every diagram to

$$P^{ij}_{\mathrm{topo}}(k, \mu; f) \;=\; \sum_{m=0}^{6} \mu^{2m}\, I_m(k; f)\,, \tag{4.6}$$

where each I_m, a polynomial in f of degree at most six, is an isotropic two-loop integral whose integrand is rational in the Gram invariants of $(\mathbf{p}, \mathbf{q}, \mathbf{k})$. We refer to the coefficient $I^{ij}_{m,a}(k)$ of $\mu^{2m} f^{\,a}$ in a diagram, a function of k alone, as a $(\mu^{2m} f^{\,a})$ component of the diagram, and to those with $a \geq 1$, which vanish at $f = 0$, as its velocity components.

Each factor of f in the redshift-space map comes with two line-of-sight indices, one of them carried by $k_z = k\mu$. A term of degree $f^{\,a}$ therefore carries μ^a times a velocities u_z, whose orientation average gives μ^{a-2j} with $0 \leq j \leq \lfloor a/2 \rfloor$. We bound a by counting fields: six powers of the linear field are available at two loops, and a bias operator of lowest perturbative order ℓ uses ℓ of them ($\ell = 0$ for the velocity entry). Hence

$$P^{ij}_{\mathrm{topo}}(k, \mu; f) \;=\; \sum_{a=0}^{6-\ell_i-\ell_j} f^{\,a} \sum_{m=0}^{a} \mu^{2m}\, I^{ij}_{m,a}(k)\,, \qquad \lceil a/2 \rceil \;\leq\; m \;\leq\; a \;\leq\; 6 - \ell_i - \ell_j \;\leq\; 6\,, \tag{4.7}$$

and every component of a diagram is one term $I^{ij}_{m,a}$ of this double sum. The selection rule $\lceil a/2 \rceil \leq m \leq a \leq 6$ admits 16 classes $(\mu^{2m}, f^{\,a})$, all populated. The velocity–velocity diagram of $P_{33,\mathrm{I}}$ saturates the bound, with powers up to μ^{12} and f^6, while the 34 diagrams with $\ell_i + \ell_j = 6$ have no line-of-sight dependence.

We identify two mechanisms by which components vanish identically. Some components are exact zeros of the reduced kernels, among them every component in the classes $\mu^2 f^3$, $\mu^2 f^4$, $\mu^4 f^5$ and $\mu^4 f^6$ that the selection rule excludes: individual velocity blocks generate such terms, which cancel in the symmetrized kernel. Others vanish under the orientation average. A loop momentum $\mathbf{q}$ that enters a kernel only through the tadpole pair $(\mathbf{q}, -\mathbf{q})$, with no other anisotropic factor, has $\langle q_z \rangle = 0$ and $\langle q_z^2 \rangle \to q^2/3$, and so produces no power of μ. On the tadpole topologies this removes the highest power of μ at the highest powers of f, though not at every power. Moreover, the γ_3 kernel is proportional to $[\mathbf{q}_1 \cdot (\mathbf{q}_2 \times \mathbf{q}_3)]^2$ and vanishes for coplanar wavevectors, and the tadpole

PRELIMINARY

configuration $(\mathbf{k}, \mathbf{p}, -\mathbf{p})$ of σ_{13} is always coplanar, so that all eight diagrams $\{i, \gamma_3\}$ of $P_{33,\mathrm{II}}$ vanish. By the same coplanarity the γ_{211} kernel vanishes on the double-tadpole arguments $(\mathbf{p}, -\mathbf{p}, \mathbf{q}, -\mathbf{q})$ of P_{15}, and hence D009 (v, γ_{211}) and D026 (b_1, γ_{211}) are zero in every component.

4.3 Evaluated components and loop-momentum support

We have evaluated components of 136 diagrams, including the vanishing γ_{211} diagrams of P_{15}. Among their 474 components we find 64 that vanish identically, 28 algebraically and 36 under the orientation average, which leaves 410 nonzero components in 134 diagrams. Of the 149 diagrams, the 8 γ_3 diagrams of $P_{33,\mathrm{II}}$ vanish identically, 135 have kernels reduced to scalar integrands, and the remaining 6 are the P_{15} pairs of v and of b_1 with γ_2, γ_3 and γ_{41} (D004, D008, D016, D021, D025 and D033), of which we evaluate the density components of D021, D025 and D033 directly from their kernels at $f = 0$. The 136 evaluated diagrams are the reduced ones other than D003, the (v, b_2) pair of P_{15}, and D037, the (v, b_1) pair and leading redshift-space coupling of P_{24}, together with D021, D025 and D033; of D020, the (b_1, b_2) pair of P_{15}, and D048, the (b_1, b_1) pair of P_{24}, we evaluate the density component only, and the reduced velocity components of these four diagrams are enumerated in the Supplementary Information, Sec. S2.

Two exact identities reduce the number of genuine two-loop integrals. First, since $Z_1(k) = b_1 + f\mu^2$ is an overall factor of P_{15}, every velocity pair satisfies $P_{15}^{v,j} = f\mu^2\, P_{15}^{1,j}$ for $j \notin \{v, b_1\}$. This gives D003 from D020, and D004, D008 and D016 from D021, D025 and D033. Second, every $P_{33,\mathrm{II}}$ component is a product of two one-loop tadpole integrals. With these two identities 53 of the 149 diagrams need no two-loop quadrature. The diagram-by-diagram enumeration with the components of each is given in the Supplementary Information, Sec. S2, and the evaluated components in Sec. S8.

Before renormalization a bare component depends on its loop-momentum support, and apart from the P_{15} components of Section 5 we take one radial support for all four topologies,

$$1.5 \times 10^{-3}\, k \;\le\; q \;\le\; 2000\, k\,. \tag{4.8}$$

Soft cancellations occur only in sums over diagrams. At small k the scaling of a bare component is therefore set by its ultraviolet sensitivity: a double-tadpole component of P_{15} or $P_{33,\mathrm{II}}$ is the external $P_{\mathrm{lin}}(k)$ times a constant multiple of $[\sigma^2(2000k)]^2$, the squared linear variance below the moving cutoff. A bare component of P_{24} or $P_{33,\mathrm{I}}$ behaves instead as k^0, k^2 or k^4 according to whether both, one or neither operator of its pair has a one-point function, times one further $\sigma^2(2000k)$ for P_{24}. The moving cutoff also sets a lowest usable wavenumber. Below roughly $k = 0.017\, h\,\mathrm{Mpc}^{-1}$ the limit $2000\, k$ excludes loop momenta that still contribute; the missing piece has the $k^2 P_{\mathrm{lin}}(k)$ shape of the leading higher-derivative counterterm and is absorbed by it without changing the renormalized spectrum. We accordingly present each component from its lowest grid point inside $0.017 \le k \le 0.2\, h\,\mathrm{Mpc}^{-1}$, whose upper end is the reach of the expansion (Section 12). Below the lowest grid point we continue the bare component analytically with its small-k form instead of extrapolating.

5 Evaluation of the two-loop integrals

We evaluate the two-loop components of Section 4 by direct quadrature in momentum space, each with the error estimate of Eq. (5.6). On a power-law basis the matter integrands reduce to master

PRELIMINARY

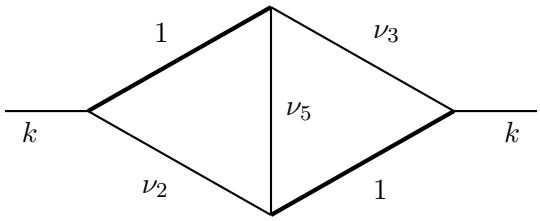

Figure 2: The two-loop kite master integral, Eq. (5.2) at $d = 3$, for the non-adjacent family $K(1, \nu_2, \nu_3, 1, \nu_5)$: the external momentum k enters and leaves at the side vertices, the internal lines carry $\nu_1, \ldots, \nu_5$ in the routing of the text (ν_4 upper left, ν_1 lower right), and the two unit indices sit on the thick lines, which share no vertex. Patterns with the unit indices on adjacent lines have closed forms in Gamma functions and single hypergeometric sums [52]; this non-adjacent family is the one pattern without such a form [39], and Eq. (5.4), derived in the Supplementary Information, Sec. S3, gives it in closed form with two additional single sums.

integrals, one family of which we give in closed form, but the expanded integrands cancel by factors reaching 9.1×10^5 (FFTLog) and 1.3×10^{17} (Laurent monomials). We therefore integrate each diagram's summed kernel directly and measure the remaining round-off by evaluating every component in double and extended precision.

5.1 FFTLog decomposition and the kite master integrals

For the matter loop integrals we expand the linear power spectrum in a finite set of complex power laws [71],

$$P_{\rm lin}(q) \;\approx\; \sum_n c_n \, q^{\nu_n}, \tag{5.1}$$

with frequencies ν_n on a line in the complex plane. Every loop integral then becomes a sum of massless self-energy integrals with complex propagator powers. At one loop these have a closed form in Gamma functions [71]; at two loops the master integral is the kite of Fig. 2,

$$K(\nu_1, \nu_2, \nu_3, \nu_4, \nu_5) \;\propto\; \int \frac{d^3q_1 \, d^3q_2}{(q_1^2)^{\nu_1} \, (q_2^2)^{\nu_2} \left[(q_1 - k)^2\right]^{\nu_3} \left[(q_2 - k)^2\right]^{\nu_4} \left[(q_1 - q_2)^2\right]^{\nu_5}} \bigg|_{|k|=1}, \tag{5.2}$$

evaluated at $d = 3$. We use the normalization of eq. (4.6) of [71], whose index ordering reads $K(\nu_1, \nu_3, \nu_5, \nu_2, \nu_4)$. Integration by parts, the Gegenbauer polynomial technique [52] and uniqueness relations solve almost every index pattern of the kite in Gamma functions and single hypergeometric sums. The exception, listed as an open case in [39], is the family $K(1, \nu_2, \nu_3, 1, \nu_5)$ with unit indices on a non-adjacent pair of lines and the other three indices generic. The two-loop matter spectrum requires this family, for which series representations exist [10, 27, 55, 71]; we give it in closed form at $d = 3$, apart from two single sums, in Eq. (5.4). The prior representations of this family are a double series and single sums of hypergeometric values with summation-dependent parameters, the latter convergent in part of the index space; we obtain a form closed in Gamma functions and hypergeometric values at unit argument with fixed parameters, apart from two explicit single sums, valid for $\Re(\nu_2 + \nu_5) < \frac{3}{2}$ and extended by the kite's symmetries.

The closed form of the non-adjacent family, which we derive in the Supplementary Information, Sec. S3, follows from the Gegenbauer-series representation [27]. Expanding the two angular

PRELIMINARY

propagators in Gegenbauer polynomials gives three blocks, each a double sum over a wedge-shaped index region, and an Abel rearrangement collapses one summation per block exactly. Each block then reduces to Gamma functions, hypergeometric values at unit argument and one single sum,

$$W_j = \sum_{k\geq 0} \hat{\Psi}_j(k) \left[(1-2k)\, Q_j^{(0)}(k-1) + 2\, Q_j^{(1)}(k-1) \right], \qquad W_2 = 0 \text{ exactly}, \tag{5.3}$$

with $\hat{\Psi}_j$ a hypergeometric term and $Q_j^{(0)}$, $Q_j^{(1)}$ partial sums of another (we call W_1 and W_3 wedges). At $d = 3$ and for $\Re(\nu_2 + \nu_5) < \frac{3}{2}$, where every single sum converges absolutely, the kite of the non-adjacent family is

$$K(1, \nu_2, \nu_3, 1, \nu_5)\Big|_{d=3} = \kappa\, \rho\, M_0 \left[\sum_{j=1}^{3} t_j^{00} \left(S_j^a\, Q_j^{(0)} + 2\, S_j^b\, Q_j^{(1)} \right) \; - \; t_1^{00} W_1 \; - \; t_3^{00} W_3 \right]. \tag{5.4}$$

Every factor except W_1 and W_3 is in closed form: the prefactors $\kappa\, \rho\, M_0$ and weights t_j^{00} are Gamma-function products, and S_j^a, S_j^b, $Q_j^{(0)}$, $Q_j^{(1)}$ are ${}_3F_2/{}_4F_3/{}_5F_4$-class values at unit argument. Their defining coefficients, the derivation, its numerical and integer-relation (PSLQ) checks and the analytic continuation are given in the Supplementary Information, Sec. S3. Under the integer index shifts generated by Eq. (5.1), W_1 and W_3 each reduce exactly onto a fixed basis of 25 elements, plus polynomials in hypergeometric values at unit argument. The rank 25 is an upper bound whose minimality is not proven. Within the Gegenbauer representation, at generic rational index points, the wedges are not hypergeometric, and no telescoping of Zeilberger–Gosper type [38, 76] reduces them to single ${}_pF_q(1)$ sums (Supplementary Information, Sec. S3); this is not a proof for all parameter values. However, a closed form through another representation may exist.

5.2 Numerical cancellations and the precision criterion

The two-loop integrands cancel in three ways, and each cancellation limits a different evaluation method. The first cancellation is infrared and occurs between diagrams. Each diagram is finite on a ΛCDM spectrum, but the leading soft contributions cancel only in the equal-time sum of P_{15}, P_{24} and P_{33} [4, 18]. We integrate each diagram separately against the actual linear spectrum, so this cancellation is numerical, tested only in the full sum. The second cancellation is ultraviolet and scheme dependent. In the regulated scheme of the Monte Carlo matter evaluation of [1], only the sum of the two ultraviolet terms given there is finite under that work's continuation of the linear spectrum. Even after regulation, the term that converts between that continuation and the standard one exceeds the whole two-loop result, $|\mathrm{UV}_{\mathrm{tot}}/P_{2\mathrm{L}}| = 1.7$ at $k = 0.2\, h\,\mathrm{Mpc}^{-1}$. Our evaluation agrees with those results at the 10^{-3} level only when that scheme's tabulated screening is used inside our kernels (Supplementary Information, Sec. S3).

The third cancellation occurs inside a single diagram. Expanded into rational monomials, a two-loop kernel is a sum of large terms of alternating sign, and power-law bases amplify their cancellation. On the FFTLog basis the amplification of the connected $P_{33,\mathrm{I}}$ rises from 1.8 to 9.1×10^5 with increasing k and drives that contribution negative above $k = 0.65\, h\,\mathrm{Mpc}^{-1}$, which is impossible for the square of a kernel. The convergence diagnostics of the FFTLog sum do not detect this failure. In Laurent monomials the connected $P_{33,\mathrm{I}}$ matter kernel cancels in double-precision arithmetic by 6×10^{15} at $k = 10^{-3}$ and by 1.3×10^{17} at $k = 1\, h\,\mathrm{Mpc}^{-1}$ (the largest amplification we

PRELIMINARY

have measured). In contrast, two-loop kernels evaluated from the recursion have been integrated by adaptive Monte Carlo to a relative tolerance of 10^{-3} [47, 74]. Therefore we evaluate each diagram's summed kernel directly in momentum space.

The double- and extended-precision evaluations $T^{(\mathrm{d})}$ and $T^{(\mathrm{e})}$ of a component use the same discretized sum, and we require them to satisfy

$$\left|T^{(\mathrm{d})}(k) - T^{(\mathrm{e})}(k)\right| \;\le\; 10^{-6}\left|T^{(\mathrm{e})}(k)\right| \tag{5.5}$$

at every tabulated wavenumber, with a second criterion on the growth of the mismatch. A component failing either criterion is re-evaluated with a regrouped kernel, or its round-off, measured against an arbitrary-precision evaluation, is added to the error estimate. The mismatch of the two evaluations measures round-off only, so their agreement does not by itself bound the quadrature error. In addition, several density components have a second, independent evaluation from the kernels of [47]; for the density component of $P_{24}^{1,3}$ the two evaluations, whose kernels agree exactly, differ by 0.87% at $k = 0.1\,h\,\mathrm{Mpc}^{-1}$, outside both stated errors (Supplementary Information, Sec. S8).

5.3 Numerical error of the evaluated components

Every evaluated component (one $(\mu^{2m} f^{a})$ component of one diagram) is computed at 140 fixed wavenumbers, each with an error estimate. In our direct-quadrature method (Supplementary Information, Sec. S3) we integrate each component at two radial-grid densities and assign it the additive error

$$\epsilon(k) \;=\; \epsilon_{\mathrm{ref}}(k) + \epsilon_{\mathrm{grid}}(k) + \epsilon_{\mathrm{reg}}(k) + \epsilon_{\mathrm{tail}}(k) + \epsilon_{\mathrm{ang}}(k). \tag{5.6}$$

The five terms are, in order, the radial refinement, the difference between the two densities, the sensitivity to the regulator, a bound on the unintegrated tail and an angular term. For the angular term of the P_{24} components we use a polar rule that resolves the soft $|k-q|$ corner, and for the slowly converging tail of some P_{15} components a wider radial support (Supplementary Information, Sec. S3). Some components are given only for $k \ge 0.01\,h\,\mathrm{Mpc}^{-1}$, and we do not extrapolate below that. At fixed shape of the linear spectrum an n-loop component T_n is homogeneous of degree $n+1$ in its amplitude,

$$T_n[A\,P_{\mathrm{lin}}] \;=\; A^{\,n+1}\,T_n[P_{\mathrm{lin}}], \tag{5.7}$$

and an amplitude rescaling is exact.

In the matter limit, a 140-point evaluation of P_{24} made before the galaxy components, with the same quadrature that produces the stated errors of the P_{24} components, differs from our direct-quadrature matter tables by more than the combined errors at 60 of its 140 wavenumbers (Supplementary Information, Sec. S8). Because internal convergence diagnostics can indicate convergence while the result has the wrong sign, every numerically evaluated component has an error built from measured quantities, Eqs. (5.6) and (5.5). The evaluated components, with their wavenumber ranges and error estimates, and those that vanish by symbolic proof are given in the Supplementary Information, Sec. S8.

6 Renormalization at two loops

Loop momenta beyond the validity of the fluid description contribute to the two-loop integrals of Section 4 with the momentum dependence that the counterterms parametrize. We subtract these

PRELIMINARY

contributions from the momentum-space integrands in the Bogoliubov–Parasiuk–Hepp–Zimmermann (BPHZ) sense [12, 44, 77], following [47], so that the bias parameters are identical at one and two loops and coincide with those of the one-loop `CLASS-PT` basis [21].

6.1 Ultraviolet structure and the subtraction forest

The bare two-loop integrals are finite but depend on their loop-momentum support until subtracted. For each diagram we apply the forest formula truncated to the limits that occur at two loops,

$$R[K] \;=\; \big(1 - T_{\rm dh}\big)\big(1 - T_{\rm sh_1}\big)\big(1 - T_{\rm sh_2}\big)\, K(q_1, q_2, k)\,, \tag{6.1}$$

where $T_{\rm sh_i}$ takes the single-hard limit $q_i \to \infty$ at fixed k and $T_{\rm dh}$ takes the double-hard limit $q_1 \sim q_2 \to \infty$ jointly, at fixed ratio q_1/q_2 and fixed angles. The joint limit $T_{\rm dh}K$ then depends on q_1/q_2 and differs from the iterated limit $T_{\rm sh_1}T_{\rm sh_2}K$ for every non-product bias operator. Ref. [47] derives the two-loop conditions of the cubic-bias sector from these limits. We do not inherit its finite-part convention: instead, we fix the finite parts by the two subtractions of Section 6.4.

Every T-term in Eq. (6.1) is itself a loop integral of lower order, evaluated like the bare one. Hence the subtracted integral is the linear combination

$$T_{\rm sub} \;=\; T_{\rm bare} - T_{\rm sh_1} - T_{\rm sh_2} + 2\,T_{\rm sh_1 sh_2} - T_{\rm dh}\,, \tag{6.2}$$

where each T is the integral of the corresponding limit of the kernel and the iterated-limit integral $T_{\rm sh_1 sh_2}$ is the piece that the two single-hard subtractions remove twice. This form holds under the overlap convention $T_{\rm dh}T_{\rm sh_i}K = T_{\rm sh_1}T_{\rm sh_2}K$.

The matter and velocity single-hard limits have exactly the momentum structure of the higher-derivative counterterms, whose leading term is

$$P_{gg}\big|_{\nabla^2\delta} \;=\; -2\,b_1\,\beta_1\,k^2 P_{\rm lin}(k)\,, \qquad \beta_1 \equiv b_1 c_s + b_{\nabla^2\delta}\,, \tag{6.3}$$

with c_s the dark-matter sound speed and $b_{\nabla^2\delta}$ the pure higher-derivative bias [47]. We absorb the double-hard limits into the k^4 and stochastic counterterms and the bias-operator hard limits into lower-order couplings; for matter the corresponding two-loop counterterms are those of [6]. Nested regions that require the full forest occur in P_{15}, whose single-hard regions each contain the double-hard domain. For $P_{33,\rm II}$, an exact square of one-loop factors, we need the one-loop subtraction through order σ^4. The inner loop of P_{24} has the single-hard limit of the B_{411} integral. The outer-momentum limit of P_{24} and the ultraviolet limit of $P_{33,\rm I}$ are Taylor series in k^2, absorbed by the stochastic counterterms [47].

6.2 Counterterm basis at two loops

At order $k^2 P_{\rm lin}$ the redshift-space mapping generates, at every loop order, one three-coefficient structure extending to μ^6,

$$P^s_{gg}\big|_{k^2 P_{\rm lin}} \;=\; 2\,(b_1 + f\mu^2)\,(c_0 + c_2\mu^2 + c_4\mu^4)\,k^2 P_{\rm lin}(k)\,. \tag{6.4}$$

Higher terms of the velocity expansion enter at k^4 and beyond. We take $c_0 = -\beta_1$, the whole μ^0 coefficient of Eq. (6.3). We include two further classes at two loops, $k^2\mu^{0,2,4}P_{\text{1-loop}}$ with coefficient

PRELIMINARY

β_1 and $k^4 P_{\rm lin}$ at μ^0 and μ^2, to which the redshift-space mapping adds the velocity-dispersion term $\tilde{c}$ at higher powers of μ (Section 9).

The single-hard expansion of a two-loop integrand continues past order $k^2 P_{\rm lin}$. Its $O(1/q_2^2)$ part is $(k^2, q_1^2, |\mathbf{k}-\mathbf{q}_1|^2)/q_2^2$ times the one-loop integrand, weighted by the convergent moment

$$\sigma^2_{-2} \;=\; \int \frac{d^3q}{(2\pi)^3}\,\frac{P_{\rm lin}(q)}{q^2} \;=\; 51.4\,(\mathrm{Mpc}/h)^2\,, \tag{6.5}$$

that is, the one-loop integrals with a k^2 insertion on the internal momentum, $(q^2+|\mathbf{k}-\mathbf{q}|^2)/2$ in P_{22} and q^2 in P_{13}. A single coefficient multiplying $k^2 P_{\text{1-loop}}$ cannot generate these terms with the internal insertion, and no finite-part shift of β_1 absorbs them. They form a separate counterterm class with fixed coefficients, products of lower couplings times σ^2_{-2}. Since $\sigma^2_{-2} = 3\sigma_v^2$ (σ_v^2 is the linear velocity dispersion), these coefficients are finite and cutoff-independent.

Through cubic order the local higher-derivative bias operators are those of [47]: $\nabla^2\delta$ with coefficient $b_{\nabla^2\delta}$, four quadratic operators with coefficients $\beta_{2,i}$ and the cubic operators with coefficients $\beta_{3,i}$. Table 9 collects all counterterm structures of the two-loop power spectrum with the status of their coefficients. For the $k^2 P_{\text{1-loop}}$ and $k^4 P_{\rm lin}$ classes we have not constructed the full redshift-space angular dependence.

6.3 Renormalization conditions and contact terms

We define the shifts δb_O of Eq. (3.25) by projecting each hard limit onto the operator basis. The coefficients are exact rationals and, with the remark made below on the $\gamma_{21}^{\times\times}$ column, equal those of [47]. The simplest case is P_{24}: the hard limit $q \gg k_1, k_2$ of its inner loop $I^{(4)}$, the B_{411} integral [32], projects onto the second-order basis,

$$\frac{1}{2}\,I^{(4)}(\mathbf{k}_1,\mathbf{k}_2)\Big|_{\rm hard} \;=\; \delta K_2(\mathbf{k}_1,\mathbf{k}_2) \;=\; \Big[\delta b_1\,F_2(\mathbf{k}_1,\mathbf{k}_2) + \frac{\delta b_2}{2} + \delta\gamma_2\,\mathcal{K}(\mathbf{k}_1,\mathbf{k}_2)\Big]\sigma^2\,. \tag{6.6}$$

It is absorbed by the coupling shifts

$$\delta b_1 = \frac{b_3}{2} + \frac{34\,b_2}{21} - \frac{4\,\gamma_2^{\times}}{3}\,, \tag{6.7}$$

$$\delta b_2 = \frac{b_4}{2} - \frac{8\,\gamma_2^{\times\times}}{3} + \frac{32\,\gamma_{21}^{\times}}{15} + \frac{32\,\gamma_2^{\rm sq}}{15} + \frac{68\,b_3}{21} + \frac{8126\,b_2}{2205} - \frac{208\,\gamma_2^{\times}}{35}\,, \tag{6.8}$$

$$\delta\gamma_2 = \frac{\gamma_2^{\times\times}}{2} - \frac{2\,\gamma_{21}^{\times}}{5} - \gamma_3^{\times} + \frac{4\,\gamma_2^{\rm sq}}{15} + \frac{127\,b_2}{2205} + \frac{92\,\gamma_2^{\times}}{105}\,. \tag{6.9}$$

The first line is Eq. (3.26). Thus one δb_1, with $\langle\delta_g\rangle = 0$ for the velocity components, cancels the hard-limit contributions of P_{13}, $P_{33,\rm II}$ and P_{24}.

For P_{15} the two single-hard limits coincide by the $\mathbf{p} \leftrightarrow \mathbf{q}$ symmetry of Eq. (4.5) and have the T_{5111} trispectrum structure generated by K_5. From this common limit we define the shift of the cubic kernel,

$$\delta K_3(\mathbf{k}_1,\mathbf{k}_2,\mathbf{k}_3) \;=\; 10\int_{\mathbf{q}} K_5(\mathbf{k}_1,\mathbf{k}_2,\mathbf{k}_3,\mathbf{q},-\mathbf{q})\,P_{\rm lin}(q)\Big|_{q\ \text{hard}}\,, \tag{6.10}$$

which projects onto the cubic basis,

$$\delta K_3 \;=\; \Big[\delta b_1\,F_3 + \frac{\delta b_2}{3}\sum_3 F_2 + \delta\gamma_2\,K^{(3)}_{\mathcal{G}_2} + \frac{\delta b_3}{6} + \frac{\delta\gamma_2^{\times}}{3}\sum_3 \mathcal{K} + \delta\gamma_3\,\mathcal{L} + \delta\gamma_{21}\,K_{\gamma_{21}}\Big]\sigma^2\,. \tag{6.11}$$

PRELIMINARY

Here $\sum_3$ runs over the three pairings of the arguments, F_3 is the cubic matter kernel, and $K^{(3)}_{\mathcal{G}_2}$, $K_{\gamma_{21}}$ are the evolved cubic kernels of $\mathcal{G}_2$ and of the $\mathcal{G}_2(\varphi_2,\varphi_1)$ operator. Evaluating this hard limit, we recover the three shifts above coefficient by coefficient and obtain the conditions of the cubic sector,

$$\begin{aligned}\delta b_3 = {}& \frac{b_5}{2} - 4\,\gamma_2^{\times\times\times} + \frac{32\,\gamma_2^{\mathrm{sq}\times}}{5} + \frac{64\,\gamma_{21}^{\times\times}}{5} - \frac{144\,\gamma_{31}^{\times}}{245} - \frac{384\,\gamma_{21,2}}{35} + \frac{34\,b_4}{7} - \frac{624\,\gamma_2^{\times\times}}{35} \\ & + \frac{2304\,\gamma_2^{\mathrm{sq}}}{245} - \frac{32\,\gamma_{21}^{\times}}{5} + \frac{8126\,b_3}{735} - \frac{16504\,\gamma_2^{\times}}{1715} + \frac{286004\,b_2}{56595}\,, \end{aligned} \tag{6.12}$$

$$\begin{aligned}\delta\gamma_2^{\times} = {}& \frac{\gamma_2^{\times\times\times}}{2} - \gamma_3^{\times\times} - \frac{16\,\gamma_2^{\mathrm{sq}\times}}{15} - \frac{4\,\gamma_{21}^{\times\times}}{5} + \frac{8\,b_{\mathcal{G}_2\mathcal{G}_3}}{5} + \frac{32\,\gamma_{22}^{\times}}{15} - \frac{8\,\gamma_{31}^{\times}}{735} + \frac{8\,\gamma_{211}^{\times}}{15} + \frac{16\,\gamma_{21,2}}{105} \\ & + \frac{262\,\gamma_2^{\times\times}}{105} - \frac{78\,\gamma_3^{\times}}{35} - \frac{152\,\gamma_2^{\mathrm{sq}}}{735} - \frac{64\,\gamma_{21}^{\times}}{105} + \frac{127\,b_3}{2205} + \frac{12877\,\gamma_2^{\times}}{5145} + \frac{7229\,b_2}{33957}\,, \end{aligned} \tag{6.13}$$

$$\begin{aligned}\delta\gamma_3 = {}& \frac{\gamma_3^{\times\times}}{2} + \frac{4\,b_{\mathcal{G}_2\mathcal{G}_3}}{5} + \frac{4\,\gamma_{211}^{\times}}{15} + \frac{131\,\gamma_{31}^{\times}}{6615} + \frac{16\,\gamma_{21,2}}{105} + \frac{66\,\gamma_3^{\times}}{35} + \frac{296\,\gamma_2^{\mathrm{sq}}}{735} + \frac{2\,\gamma_{21}^{\times}}{5} \\ & + \frac{3433\,\gamma_2^{\times}}{9261} - \frac{421\,b_2}{101871}\,, \end{aligned} \tag{6.14}$$

$$\delta\gamma_{21} = \gamma_{21}^{\times\times} + \frac{8\,\gamma_{22}^{\times}}{15} - \frac{31\,\gamma_{31}^{\times}}{630} - \frac{2\,\gamma_{211}^{\times}}{3} + \frac{4\,\gamma_{21,2}}{15} - \frac{12\,\gamma_{21}^{\times}}{35} + \frac{142\,\gamma_2^{\times}}{735} + \frac{1262\,b_2}{33957}\,. \tag{6.15}$$

These conditions agree with those of [47] up to the normalization of $\gamma_{21}^{\times\times}$, which carries no factor $1/2$ here. We obtain the $\gamma_{31}^{\times}$ column from the fifth-order $\gamma_{31}^{\times}$ kernel of Section 3.1, transverse term included: its scalar part, built on S_3 alone, gives $(-32/49, -26/735, 158/6615, -4/63)$, and the transverse $\Psi^{(3)}$ term adds $(+\frac{16}{245}, +\frac{6}{245}, -\frac{1}{245}, +\frac{1}{70})$ per unit $\gamma_{31}^{\times}$.

The double-hard limit of P_{15} gives the last condition of the cubic sector, $\delta b_1\big|_{\sigma^4} = \big(-\frac{1}{4}\,\delta b_3 + \frac{2}{3}\,\delta\gamma_2^{\times} - \frac{17}{21}\,\delta b_2\big)\sigma^4$ in the ordered limit $q_1/q_2 \to \infty$, with the relative sign of the BPHZ subtraction [47]. This coefficient is exact only for the product operators (b_4, b_5, $\gamma_2^{\times\times\times}$). For the other couplings the angle-averaged kernel at $k \to 0$ depends on q_1/q_2, and the T_{dh} integrals contain a further constant times $P_{\mathrm{lin}}(k)$, degenerate with b_1. By recovering the rationals of [47] from the hard limits, we test the kernels of 24 of the 29 basis operators. The other five have not been checked.

We also normal-order the bias operators, $\langle\delta_g\rangle = 0$: the unit-operator counterterm removes the mean of every composite operator, $b_2\sigma^2/2$ at order σ^2 and the tadpoles of b_2, b_3, $\gamma_2^{\times}$ and $\gamma_{21}^{\times}$ at order σ^4. In real space that counterterm contributes only at $k = 0$, but in redshift space the $(1+\delta_g)$ weighting of the velocity map multiplies it by the full linear kernel and leaves $\langle\delta_g\rangle\, f\mu^2 P_{\mathrm{lin}}$ times Z_1. No coupling of the 18-component vector c absorbs this term at fixed f. At one loop the P_{13} terms containing b_2 are constants times $\sigma^2(q_{\mathrm{max}})\,P_{\mathrm{lin}}$. The constant is $68/21 = 2 \times 34/21$, twice the b_2 coefficient of the one-loop shift δb_1, for the $b_1 b_2\,\mu^0$ and $b_2 f\mu^2$ terms, and 1, the mean of δ^2 entering through the velocity map, for the $b_1 b_2 f\mu^2$ and $b_2 f^2\mu^4$ terms. Renormalization removes all four exactly, whatever the size of $\sigma^2(q_{\mathrm{max}})$ (145.89 at $q_{\mathrm{max}} = 300\,h\,\mathrm{Mpc}^{-1}$ and $z = 0.61$).

At two loops the one-point functions of the composite operators produce the largest bare terms, the 27 double-tadpole components of P_{15} and $P_{33,\mathrm{II}}$ at or above $10^6\,(\mathrm{Mpc}/h)^3$ at $k = 0.1\,h\,\mathrm{Mpc}^{-1}$, 17 in P_{15} and ten in $P_{33,\mathrm{II}}$. These share the form

$$T(k) \;=\; \kappa\,P_{\mathrm{lin}}(k)\,\big[\sigma^2(2000k)\big]^2\,, \qquad \sigma^2(Q) \;=\; \int_{1.5\times10^{-3}k}^{Q} \frac{d^3q}{(2\pi)^3}\,P_{\mathrm{lin}}(q)\,, \tag{6.16}$$

PRELIMINARY

where κ is a constant of the operator pair and $(\mu^{2m} f^a)$ component, with $|\kappa|$ ranging from 1/4 to approximately 18. They rise relative to $P_{\rm lin}$ as $k^{1.31}$, the cutoff scaling of an unsubtracted contact term, solely because the loop support scales with k. Indeed, the ten $P_{33,\rm II}$ terms are pure contact terms to all orders and vanish in our subtracted scheme. In P_{15} a density component and its velocity partner one power of $\mu^2 f$ higher share one integral; only the $\mu^2 f$ component of (b_1, b_3) has a rational constant, $\kappa = 34/21$, and maps to numerically zero, while the other seven integrals have support-dependent constants and keep finite remainders, whose accuracy at $q \sim k$ is untested.

We exclude from the fixed two-loop sum, and leave to the counterterms, every component whose integrand reduces to a pure single-hard contact term (a constant times $k^2 P_{\rm lin}$ or a σ^2-weighted lower-order shape). These are the 10 double-tadpole $P_{33,\rm II}$ terms, 33 single-hard-only terms, 23 contact-dominated P_{15} components and 51 tadpole-only P_{24} components, those whose contact leg contains b_2, b_3, $\gamma_2^\times$ or $\gamma_{21}^\times$. We give the derivation of each condition, the 27 double-tadpole components, and the classification and subtraction terms of every component in the Supplementary Information, Sec. S4.

6.4 Finite parts and the pivot scale

We fix the finite part of each loop integral by one of two linear subtractions. The first, our subtracted scheme, removes the σ^2 and σ^4 terms that dimensional regularization sets to zero, as in [47]. We construct it from the angle-integrated kernels on a fixed loop support $10^{-5} \le q \le 100\,h\,\mathrm{Mpc}^{-1}$, on which $\sigma^2 = 49.4$. For a P_{15} or $P_{33,\rm II}$ component we apply the two single-hard subtractions and then take the double-hard limit, which splits the integral as

$$T \;=\; T_{\rm dh} + T_{\rm sh} + T_{\rm R}\,, \qquad T_{\rm dh} \;=\; P_{\rm lin}(k)\left(M_0 + k^2 M_2\right). \tag{6.17}$$

Here, $T_{\rm sh}$ is σ^2 times the one-loop integrals of the two hard legs with their common iterated limit removed, (M_0, M_2) are the leading moments of the remaining kernel with both loop momenta hard, and the remainder $T_{\rm R}$ is the subtracted integral. Similarly, we split a P_{24} component on its $\mathbf{q}_2$ tadpole. From a $P_{33,\rm I}$ component we subtract only a $k \to 0$ constant. Twelve of the components that enter the two-loop spectrum are renormalized by the pivot condition below only, without this subtraction (Supplementary Information, Sec. S4).

Two finite-part choices of the subtracted scheme differ from the dimensionally regulated prescription of [47]. First, the σ^2_{-2} class of Eq. (6.5) stays in the remainder with its fixed coefficient. In particular, our β_1 is not the two-loop-renormalized β_1 of [47]. Second, we stop the double-hard subtraction at k^2: the double-hard k^4 moment M_4 stays in the remainder, while the single-hard-type part $\sigma^2 k^4 \sigma^2_{-4}$ (σ^2_{-4} is the $P_{\rm lin}/q^4$ moment, infrared-divergent for $n_s < 1$) is removed with the single-hard piece.

The second subtraction is a pivot condition on every component that enters the spectrum: we require the renormalized component to vanish at $k_* = 0.2\,h\,\mathrm{Mpc}^{-1}$ (Fig. 3),

$$T_{\rm ren}(k) \;=\; T_{\rm bare}(k) - \alpha\, k^2 P_{\rm lin}(k)\,, \tag{6.18}$$

$$\alpha \;=\; \frac{T_{\rm bare}(k_*)}{k_*^2\, P_{\rm lin}(k_*)}\,. \tag{6.19}$$

Here, $T_{\rm bare}$ is the bare integral with no forest terms subtracted, and $P_{\rm lin}$ is the linear spectrum of the cosmology at which the integrals are evaluated, so α should be recomputed for each cosmology. The components tabulated in the Supplementary Information instead carry this subtraction with

PRELIMINARY

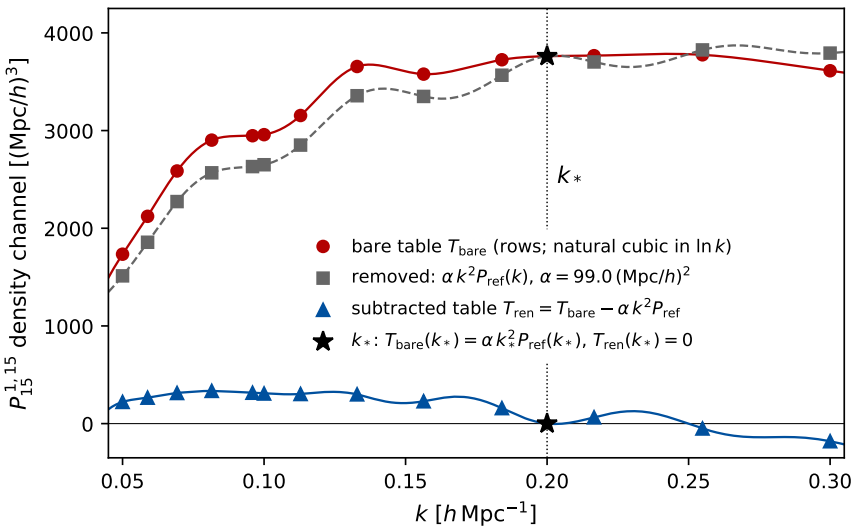

Figure 3: Pivot subtraction, Eq. (6.18), on one two-loop component: the density component of $P_{15}^{1,15}$ ($b_1\gamma_{41}$ pair, diagram D033, evaluated at $f = 0$) at $z = 0.61$. Red circles: bare integral $T_{\rm bare}$. Gray squares: removed part $\alpha\, k^2 P_{\rm ref}$, $\alpha = 99.0\,({\rm Mpc}/h)^2$, with $P_{\rm ref}$ a fixed reference linear spectrum used in place of $P_{\rm lin}$ in this illustration. Blue triangles: renormalized component $T_{\rm ren}$, an order of magnitude smaller and zero at $k_* = 0.2$ (dotted line, stars). Curves interpolate in $\ln k$; per-point errors (a few times 10^{-3} of $T_{\rm bare}$) are below symbol size. Wavenumbers in $h\,{\rm Mpc}^{-1}$, values in $({\rm Mpc}/h)^3$.

one fixed reference spectrum $P_{\rm ref}$, the $z = 0.61$ linear spectrum, at both redshifts (Sec. S4). We apply the pivot to the two-loop integrals as they enter the resummed model of Section 7, so that evaluations with scale-independent f and with exact $f(k)$ use identical renormalized integrals. The residual shape dependence left by the pivot subtraction at $k_* = 0.2\,h\,{\rm Mpc}^{-1}$ has not been quantified.

Each pivot removes $\alpha\, k^2 P_{\rm lin}$ from one coefficient of $\mu^{2m} f^{\,a}$ in Eq. (3.23). At fixed redshift, where f is a number, the total scheme dependence of the spectrum therefore collects into

$$\Delta_{\rm scheme} P^s_{gg}(k,\mu) \;=\; k^2 P_{\rm lin}(k) \sum_{m=0}^{6} \alpha_m\, \mu^{2m}\,, \tag{6.20}$$

a polynomial in μ^2 of degree six whatever the bias coefficients, with α_m the f-weighted sum of the α of the μ^{2m} components; the seven α_m are scheme constants. Projected onto P_0, P_2 and P_4 the seven monomials have rank three, the span of (c_0, c_2, c_4), and under finer angular projections the α_m with $m \geq 3$ stay fixed and add no free parameter. We normalize c_0 by the one-loop σ^2_{-2} on the one-loop support. In the bispectrum, whose loop support differs, the same c_0 shifts by the change in σ^2_{-2}. The pivot condition is identical at both fiducial redshifts, $z = 0.61$ and 0.2954, and only the derived α values differ.

PRELIMINARY

7 Infrared resummation

Long-wavelength displacements at low redshift are comparable to the width of the baryon acoustic feature. Their effect on that feature therefore cannot be left to a fixed order of the loop expansion, whereas their effect on the smooth spectrum cancels order by order [7, 13, 70]. We extend the one-loop prescription of Eq. (2.15) to two loops with the anisotropic damping scale of [49]. We damp each term according to its own loop order and that of the calculation, and apply the damping factor of the one-loop terms inside their loop integrals.

7.1 Damping order and loop order

To leading power in the soft momenta, averaging over the relative displacement from modes softer than k damps the acoustic feature at fixed μ by a Gaussian factor [70, 73]. The resummed wiggly spectrum then reads

$$P_{\rm w}^{\rm res}(k,\mu) = e^{-x}\left[\,P_0^{\rm w} + S_1 + S_2 + S_3 + \cdots\right], \qquad x = k^2\,\Sigma^2_{\rm tot}(z,\mu)\,. \tag{7.1}$$

Here $P_0^{\rm w} = (b_1 + f\mu^2)^2 P_{\rm w}$ is the tree wiggle, S_n is the infrared-safe n-loop wiggle (the n-loop wiggle with its infrared-enhanced part removed) and $\Sigma^2_{\rm tot}$ is defined below. Since the fixed-order terms contain the expansion of e^{-x}, the one-loop and two-loop wiggles are

$$P_1^{\rm w} = S_1 - x\,P_0^{\rm w}\,, \qquad P_2^{\rm w} = S_2 - x\,S_1 + \tfrac{1}{2}\,x^2\,P_0^{\rm w}\,. \tag{7.2}$$

Requiring the net damping of $P_0^{\rm w}$, S_1 and S_2 each to equal e^{-x} through the loop order N of the calculation fixes the damping factor of a term of loop order n,

$$D_n^{(N)}(x) = e^{-x}\sum_{j=0}^{N-n}\frac{x^j}{j!}\,. \tag{7.3}$$

This is the prescription of [70, 73] in real space and of [47, 49] in redshift space. At $N = 2$ the tree, one-loop and two-loop terms carry $D_0^{(2)} = e^{-x}(1 + x + \frac{1}{2}x^2)$, $D_1^{(2)} = e^{-x}(1+x)$ and $D_2^{(2)} = e^{-x}$ [37, 73, 74], and the three net factors become

$$\begin{aligned} P_0^{\rm w}:&\quad e^{-x}\big[(1 + x + \tfrac{1}{2}x^2) - x(1+x) + \tfrac{1}{2}x^2\big] = e^{-x}\,,\\ S_1:&\quad e^{-x}\big[(1+x) - x\big] = e^{-x}\,, \qquad\qquad S_2:\quad e^{-x}\,. \end{aligned} \tag{7.4}$$

Thus the three damped terms sum to $e^{-x}[P_0^{\rm w} + S_1 + S_2]$ identically. Every infrared-enhanced contribution through two loops is resummed exactly once, and the first omitted term is $e^{-x}S_3$. Each counterterm is damped like the diagrams it renormalizes [37]; the change produced by leaving the counterterm shapes undamped is quantified in the Supplementary Information, Sec. S5. By contrast, Ref. [74] damps all counterterms by e^{-x}.

We do not extract the two-loop wiggle $P_2^{\rm w}$ from the two-loop diagrams: its infrared-enhanced part, $-xS_1 + \frac{1}{2}x^2P_0^{\rm w}$ in Eq. (7.2), is determined entirely by the tree and one-loop wiggles and by the displacement scale, and its infrared-safe part S_2 is the truncation error estimated below. We therefore evaluate every two-loop diagram on the smooth spectrum $P_{\rm nw}$ only and add the closed-form completion term

$$P_\ell^{\text{2-loop,IR}}(k) = \frac{2\ell+1}{2}\int_{-1}^{1} d\mu\,\mathcal{P}_\ell(\mu)\,e^{-x}\Big[-x\,S_1(k,\mu) + \tfrac{1}{2}x^2\,P_0^{\rm w}(k,\mu)\Big]\,, \tag{7.5}$$

PRELIMINARY

where $\mathcal{P}_\ell$ is the Legendre polynomial and $S_1 = P_1^{\rm w} + xP_0^{\rm w}$. The completion term thus contains no free amplitude. Together with the damped tree and one-loop wiggles it reproduces $e^{-x}(P_0^{\rm w} + S_1)$ exactly. We estimate the omitted $e^{-x}S_2$ roughly as $\epsilon\, e^{-x}S_1$, with $\epsilon(k)$ the ratio of the root mean squares over μ of S_1 and $P_0^{\rm w}$. The Supplementary Information, Sec. S5, instead carries the two-loop wiggle through components evaluated on damped input spectra (its hybrid form), which retains $e^{-x}S_2$; Paper II uses that form.

On the smooth spectrum each two-loop diagram still carries a bulk-flow enhancement from soft loop momenta, which cancels only in the equal-time sum over the four topologies [13, 53]. To leading power a soft mode enters the kernels Z_n only through the displacement it generates along $\mathbf{k}_s = \mathbf{k} + fk_z\hat{\mathbf{z}}$. Hence each topology D contains a universal dipole term, which we subtract to make each diagram infrared-safe on its own,

$$\widetilde{V}_D(k,\mu) = V_D(k,\mu) - c_D\, k_s^2\, \sigma_W^2\,, \qquad k_s^2 = k^2\big(1 + 2f\mu^2 + f^2\mu^2\big)\,, \tag{7.6}$$
$$c_{15} = -\tfrac{1}{2}\,P_{13}\,,\;\; c_{24} = P_{13} - P_{22}\,,\;\; c_{33,\rm I} = P_{22}\,,\;\; c_{33,\rm II} = -\tfrac{1}{2}\,P_{13}\,,\;\; \textstyle\sum_D c_D = 0\,.$$

Here V_D is the contribution of topology D at fixed operator pair, σ_W^2 is the one-dimensional displacement variance of the soft modes, and P_{13}, P_{22} are the one-loop terms of the same pair. The factor k_s^2 distributes each $\mu^{2m}f^a$ component of P_{13} and P_{22} over three components of the two-loop diagram in the ratio $1 : 2f : f^2$. Because the weights c_D add up to zero, the sum over the four topologies is unchanged, while each $\widetilde{V}_D$ is infrared-safe separately, component by component in $\mu^{2m}f^a$. In particular, a truncated set of the two-loop diagrams of Section 4 with fixed relative amplitudes is infrared-safe only if all four topologies are present in every component to which it contributes.

7.2 Resummation inside the loop integrals

The anisotropic damping scale of [49] is, in our Fourier convention,

$$\Sigma^2_{\rm tot}(z,\mu) = \big[1 + f\mu^2(2+f)\big]\,\Sigma^2 + f^2\mu^2(\mu^2-1)\,\delta\Sigma^2\,, \tag{7.7}$$
$$\Sigma^2(z) = \frac{1}{6\pi^2}\int_0^{k_S} dq\, P_{\rm nw}(q)\Big[1 - j_0(qr) + 2j_2(qr)\Big]\,, \tag{7.8}$$
$$\delta\Sigma^2(z) = \frac{1}{2\pi^2}\int_0^{k_S} dq\, P_{\rm nw}(q)\, j_2(qr)\,.$$

Here j_n are spherical Bessel functions, k_S separates the resummed soft modes from the rest and r is the comoving radius of the acoustic feature [21, 49, 73, 74]. We take $k_S = 0.2\,h\,{\rm Mpc}^{-1}$ and r equal to the drag-epoch sound horizon of the fiducial cosmology, $r_s^d = 147.146\,{\rm Mpc}$ ($99.577\,{\rm Mpc}/h$ at its $h = 0.6767$), both held fixed for every cosmology. We evaluate both integrals on the no-wiggle spectrum of the cosmology at hand, so they vary with the amplitude and shape parameters. The resummation therefore introduces no free parameter. The residual k_S dependence is formally of higher order in the soft displacements.

At $N = 2$ we apply the one-loop factor $D_1^{(2)}$ inside the loop integral rather than at the external wavenumber. We replace every linear spectrum in the one-loop integrands, at its own momentum and line-of-sight angle, by the damped input

$$P_{\rm in}(q,\mu_q) = P_{\rm nw}(q) + D_1^{(2)}\big(q^2\,\Sigma^2_{\rm tot}(z,\mu_q)\big)\,P_{\rm w}(q)\,, \qquad \mu_q = \hat{\mathbf{q}}\cdot\hat{\mathbf{z}}\,, \tag{7.9}$$

PRELIMINARY

as in [49, 73]. Applying $D_1^{(2)}(k^2\Sigma^2_{\rm tot})$ as an outer factor at the external wavenumber gives the same result only to leading power in the soft momenta, up to an anisotropic remainder of the next order. Because $P_{\rm in}$ depends on μ_q, the usual reduction to isotropic integrals multiplying powers of μ no longer applies, and we compute the resummed one-loop term as a function of (k,μ).

We resum the tree term by the replacement $P_{\rm lin} \to P_{\rm nw} + D_0^{(2)}(x)\, P_{\rm w}$ in the Kaiser spectrum and project it onto multipoles with the damped Legendre weights

$$c_\ell(m) = \frac{2\ell+1}{2}\int_{-1}^{1} d\mu\, \mathcal{P}_\ell(\mu)\, \mu^{2m}\,,$$
$$c_\ell^D(m,k) = \frac{2\ell+1}{2}\int_{-1}^{1} d\mu\, \mathcal{P}_\ell(\mu)\, \mu^{2m}\, D_n^{(N)}\big(k^2\Sigma^2_{\rm tot}(z,\mu)\big)\,. \tag{7.10}$$

The resummed two-loop contribution is the sum of the dipole-subtracted diagrams and the completion term,

$$P_\ell^{\text{2-loop,res}}(k) = \sum_c A_c\, c_\ell(m_c)\, \widetilde{V}_c^{\rm nw}(k) + P_\ell^{\text{2-loop,IR}}(k)\,, \tag{7.11}$$

where c runs over the $\mu^{2m_c} f^{a_c}$ components of the diagrams, $\widetilde{V}_c^{\rm nw}$ is the dipole-subtracted component c evaluated on $P_{\rm nw}$, and A_c collects its two bias coefficients from Eq. (3.23), its power of f and its prefactor. At small k we test the infrared cancellation among the four topologies, on which the dipole subtraction relies, by splitting each P_{15} or $P_{33,\rm II}$ component into hard parts and a remainder as in Eq. (6.17). Where numerically resolved, the sum of the remainders over the four topologies at fixed operator pair scales approximately as $k^4[A\,P_{\rm lin}(k) + C]$ (all sums are in the Supplementary Information, Sec. S3).

7.3 Damping scales, the bispectrum and the trispectrum

The isotropic average of $\Sigma^2_{\rm tot}(z,\mu)$ over μ is

$$\bar\Sigma^2(z) = \frac{1}{2}\int_{-1}^{1} d\mu\, \Sigma^2_{\rm tot}(z,\mu) = \Big[1 + \tfrac{f(2+f)}{3}\Big]\Sigma^2 - \tfrac{2}{15}\, f^2\, \delta\Sigma^2\,, \tag{7.12}$$

which for the fiducial cosmology is $25.769\,(\mathrm{Mpc}/h)^2$ at $z = 0.61$ (32.937 at $z = 0.2954$). In the one-loop bispectrum we replace every linear spectrum at its own argument, with the same damping factors $D_n^{(N)}$ as in the power spectrum,

$$P_{\rm lin}(k_i) \;\to\; P_{\rm nw}(k_i) + D_n^{(N_B)}\big(k_i^2\,\bar\Sigma^2\big)\, P_{\rm w}(k_i)\,, \tag{7.13}$$

where N_B is the loop order of the bispectrum calculation. Using the isotropic average $\bar\Sigma^2$ in every term is the leading approximation for the bispectrum monopole. At $N_B = 1$ the tree terms carry $(1+x)e^{-x}$ and all other terms e^{-x}; at $N_B = 0$ (tree bispectrum only) every term carries e^{-x}. Every bispectrum term is linear in each input spectrum through the map K to its coefficients $c = K[P_{\rm lin}]$ on the evaluation basis of Section 5. The replacement is therefore an exact shift of those coefficients,

$$c^{\rm tree} = c + K\big[\big((1+x)e^{-x} - 1\big)P_{\rm w}\big]\,, \qquad c^{\rm loop} = c + K\big[\big(e^{-x} - 1\big)P_{\rm w}\big]\,. \tag{7.14}$$

In an alternative form of the bispectrum tree term, which should be more accurate for configurations along the line of sight [49], the anisotropic scale enters on each leg inside the orientation integrals and the bin average of Section 9.5,

$$P_{\rm lin}(k_i) \;\to\; P_{\rm nw}(k_i) + D_0^{(N_B)}\big(k_i^2\,\Sigma^2_{\rm tot}(z,\mu_i)\big)\, P_{\rm w}(k_i)\,. \tag{7.15}$$

PRELIMINARY

A damping factor that depends on μ_i cannot be written as a shift of the coefficients c as in Eq. (7.14). In this form we evaluate the tree term with the damping scales and f held at fixed reference values at each redshift, and the other terms keep the isotropic shift $c^{\rm loop}$. Either form may be used at tree level (the anisotropic one is written out in the Supplementary Information, Sec. S5).

We estimate the anisotropic remainder left by an outer damping factor as the change in the two-loop components when a single isotropic factor $e^{-k^2\bar{\Sigma}^2}$ is moved from inside the loop integrals to the external wavenumber. These residuals by multipole and the damping scales at seven redshifts are given in the Supplementary Information, Sec. S5. Two contributions are not resummed: the stochastic terms of the power spectrum, which contain no acoustic feature, and the trispectrum (Section 10), whose tree term enters the covariance with bare spectrum factors. We bound the effect of leaving these factors bare using an isotropic damping $e^{-k^2\Sigma^2}$ with $\Sigma^2 = 17.58\,(\mathrm{Mpc}/h)^2$, distinct from the $\Sigma^2(z)$ defined above, and a Savitzky–Golay split of the linear spectrum, both conventions of this bound only. With a wiggle fraction $|w| = |P_{\rm w}/P_{\rm lin}|$ of at most 4.6 percent on the band 0.02 to $0.12\,h\,\mathrm{Mpc}^{-1}$, resumming the three spectrum factors would change the trispectrum by an amount bounded as

$$\left|\frac{\Delta T}{T}\right| \le 3 \max|w| \left(1 - e^{-k^2\Sigma^2}\right) \tag{7.16}$$

at most a few percent of $T_{\rm tree}$ on this band, which we treat as a bound and do not correct for. Where a measurement requires it, the correction could be included by placing the resummed linear spectra on the external legs.

8 Stochastic terms and the full power spectrum model

For discrete tracers the bias expansion is supplemented by a noise field ϵ, uncorrelated with δ_1, whose connected moments generate the stochastic terms of all three statistics. We specify these terms here and then assemble the full two-loop power spectrum.

8.1 Stochastic power spectrum at two-loop order

With primes denoting spectra stripped of momentum-conserving delta functions, we write the noise moments as

$$\langle \epsilon\,\epsilon \rangle' = \frac{1 + P_{\rm shot}}{\bar{n}}, \qquad \langle \epsilon\,\epsilon\,\epsilon \rangle'_c = \frac{A_{\rm shot}}{\bar{n}^2}, \qquad \langle \epsilon\,\epsilon\,\epsilon\,\epsilon \rangle'_c = \frac{T_{\rm shot}}{\bar{n}^3}, \tag{8.1}$$

where $\bar{n}$ is the mean density, $P_{\rm shot}$ the fractional departure of the pair term from Poisson, and $A_{\rm shot}$, $T_{\rm shot}$ the higher connected amplitudes in Poisson units [11]. The Poisson point is $P_{\rm shot} = 0$, $A_{\rm shot} = T_{\rm shot} = 1$. In the power spectrum the noise terms are analytic in k and of degree zero in $P_{\rm lin}$, and through k^4 we write

$$P_{gg}^{s,\rm stoch}(k,\mu) = \frac{1}{\bar{n}}\left[1 + P_{\rm shot} + \left(a_0 + a_2\,\mu^2\right)\frac{k^2}{k_{\rm stoch}^2} + a_4^{(P)}\,\frac{k^4}{k_{\rm stoch}^4}\right], \qquad k_{\rm stoch} = 1\,h\,\mathrm{Mpc}^{-1}, \tag{8.2}$$

where $k_{\rm stoch}$ is a fixed reference scale. The constant and k^2 terms form the one-loop stochastic spectrum $P_{\rm stoch}$ [11], and the quartic term is of two-loop order. Here $P_{\rm shot}$, a_0 and $a_4^{(P)}$ are the three stochastic parameters of the real-space model of [47], whose normalization we adopt. The superscript distinguishes $a_4^{(P)}$ from the bispectrum coefficient a_4 below.

PRELIMINARY

The stochastic terms are partly degenerate with the counterterms. In particular, only the scale dependence of $P_{\rm lin}$ distinguishes $a_0 + a_2\mu^2$ from the $k^2 P_{\rm lin}$ coefficients and $a_4^{(P)}$ from the $k^4 P_{\rm lin}$ ones ($\tilde{c}$ among them). We keep both sets, which arise from different operators. Deterministic loops also generate white noise: the $\mu^0\, b_2^2$ term of the one-loop P_{22}-type integral tends to a constant as $k \to 0$. We keep it in the loop for all three statistics; it could equally be absorbed into $P_{\rm shot}$, as in the common one-loop convention [21]. At two loops the double-hard region of the integrals produces contact terms of the same form, which renormalize the four stochastic parameters above.

8.2 The c_0 image term and the Poisson terms

After renormalization the linear kernel is $K_1(q) = b_1 + c_0\, q^2$ with $c_0 = -\beta_1$ in $({\rm Mpc}/h)^2$, which makes $2b_1c_0$ the μ^0 coefficient of the $k^2 P_{\rm lin}$ counterterm below. Because the redshift-space map acts on the whole galaxy field, $Z_2^{\rm gal}$ contains the image of the $c_0\, q^2$ term,

$$Z_2^{\rm gal} \;\supset\; \frac{f\mu_{12}q_{12}}{2}\, c_0 \left(\frac{q_1^2\,\mu_2}{q_2} + \frac{q_2^2\,\mu_1}{q_1} \right), \qquad \mu_{12}q_{12} = -k_3\mu_3 \text{ under closure}\,, \tag{8.3}$$

and the tree bispectrum contains the additional term $2\, Z_1^{\rm gal}(\mathbf{k}_i)\, Z_1^{\rm gal}(\mathbf{k}_j)\, (f\mu_{12}q_{12}/2)\, c_0\, (k_i^2\mu_j/k_j + k_j^2\mu_i/k_i)\, P_{\rm lin}(k_i) P_{\rm lin}(k_j)$ plus two cyclic permutations, with the same signs as in [11]. This term comes from the long-wavelength product $(1+\delta_g)u_z$. It therefore has no free coefficient and is neither a counterterm nor a combination of the counterterm structures $R_1, \ldots, R_{11}$ of Section 9. We include it at tree level only, its one-loop corrections being of two-loop order. Its coupling monomials $c_0 b_1^2 f$, $c_0 b_1 f^2$, $c_0 f^3$ extend the tree bispectrum from fourteen monomials to seventeen and from 18 weighted tree shapes to 19.

In the bispectrum the noise enters at orders $\bar{n}^{-1}$ and $\bar{n}^{-2}$. We group the stochastic terms of [11], complete under their power counting, into five contributions,

$$B_{\rm stoch} \;=\; B^{\rm tree}_{\rm mixed} \;+\; B^{(\bar{n}^{-2})}_{\rm stoch} \;+\; B^{\rm ctr,I}_{\rm mixed} \;+\; B^{\rm ctr,II}_{\rm mixed} \;+\; B^{\text{1-loop}}_{\rm mixed}\,, \tag{8.4}$$

where the mixed tree term is given by

$$B^{\rm tree}_{\rm mixed} \;=\; \frac{1}{\bar{n}} \sum_{i=1}^{3} Z_1^{\rm gal}(\mathbf{k}_i)\, P_{\rm lin}(k_i) \left[\, B_{\rm shot}\, b_1 + (1 + P_{\rm shot})\, f\mu_i^2 \,\right] \tag{8.5}$$

with $B_{\rm shot}$ the amplitude of the b_1 term in Poisson units. The pure $\bar{n}^{-2}$ term is $A_{\rm shot}/\bar{n}^2$ plus two k^2 corrections with coefficients a_1, a_6. The first mixed counterterm contribution has ten $k^2 P_{\rm lin}/\bar{n}$ terms with coefficients a_0 (shared with the power spectrum, whose a_2 generates no bispectrum term), a_3, a_4, a_5, $a_7, \ldots, a_{12}$. The second is built from $P_{\rm shot}$, $B_{\rm shot}$ and the power-spectrum counterterms ($\tilde{c}$ included) without new parameters. The mixed one-loop contribution consists of the P_{22}- and P_{13}-type loops with one noise leg [11]. Their noise-side kernels carry the coefficients d_1, d_2, $d_{\mathcal{G}_2}$, d_{Γ_3} times $(1 + P_{\rm shot})/\bar{n}$, with d_1 fixed by the identity

$$(1 + P_{\rm shot})\, d_1 \;=\; \tfrac{1}{2}\, b_1 B_{\rm shot}\,, \tag{8.6}$$

which leaves three new parameters.

PRELIMINARY

In total, the power spectrum and bispectrum have nineteen stochastic parameters at one loop, the shared $P_{\rm shot}$, a_0 and a_2 counted once. At the Poisson point ($P_{\rm shot} = 0$, $B_{\rm shot} = A_{\rm shot} = 1$) and with a_1, a_6 set to zero, the mixed tree term and the pure $\bar{n}^{-2}$ term reduce to

$$B_{\rm stoch}\Big|_{\rm Poisson} \;=\; \frac{1}{\bar{n}}\Big[\,P_{gg}^{s,\rm tree}(k_1,\mu_1) + P_{gg}^{s,\rm tree}(k_2,\mu_2) + P_{gg}^{s,\rm tree}(k_3,\mu_3)\,\Big] \;+\; \frac{1}{\bar{n}^2}\,, \tag{8.7}$$

which has no free parameter. However, for real tracers $B_{\rm shot}$ may exceed its Poisson value while $A_{\rm shot}$ remains close to unity, and we treat the Poisson point as a reference. The mixed one-loop stochastic term of the trispectrum contains a further family with more than one mixed leg, whose bispectrum analog, with one deterministic and two mixed legs, is not among the five contributions to $B_{\rm stoch}$. We leave open whether that family enters at the order kept here.

Under a weighted selection with local mean density $\bar{n}$ and weight w per volume element (cell) we define

$$I[a,b] \;=\; \sum_{\rm cells} \bar{n}^{\,a}\, w^{\,b}\,, \qquad c_p^{(N)} \;=\; \frac{I[N-p,\,N]}{I[N,N]}\,, \tag{8.8}$$

and each factor $\bar{n}^{-p}$ of a Poisson term in the N-point statistic becomes $c_p^{(N)}$. We define the amplitudes $P_{\rm shot}$, $A_{\rm shot}$, $B_{\rm shot}$, $T_{\rm shot}$ with these quotients factored out, so that they keep their Poisson-point values under any weighting. The model and the three covariances of Section 11 contain the same quotients and therefore have a common Poisson limit.

8.3 The full power spectrum model and its parameters

The full redshift-space galaxy power spectrum at two-loop order is then

$$\begin{aligned} P_{gg}^{s}(k,\mu) \;=\; & P_{gg}^{s,\rm tree}(k,\mu) \;+\; P_{gg}^{s,22+13}(k,\mu) \;+\; \sum_{i\le j} c_i\,c_j\,\Big(P_{15}^{ij} + P_{24}^{ij} + P_{33,\rm I}^{ij} + P_{33,\rm II}^{ij}\Big)(k,\mu;f) \\ & +\; 2\big(b_1 + f\mu^2\big)\big(c_0 + c_2\mu^2 + c_4\mu^4\big)\,k^2 P_{\rm lin}(k) \;+\; \Delta_{\rm scheme} P_{gg}^{s}(k,\mu) \\ & +\; P^{s,\rm ctr}_{k^4,\,k^2 P_{\text{1-loop}}}(k,\mu) \;+\; P_{gg}^{s,\rm stoch}(k,\mu)\,. \end{aligned} \tag{8.9}$$

The first two terms are the tree spectrum and the bare one-loop integrals; the symbol $P_{gg}^{s,\text{1-loop}}$ of Eq. (2.16) is reserved for the complete one-loop model [21]. The bilinear sum over the four topologies, with c given below, is the deterministic two-loop term, which we evaluate and renormalize as in Sections 4–6. The second line contains the one-loop counterterm, in the weighted form implied by the c_0 convention, and the scheme polynomial $\Delta_{\rm scheme}P_{gg}^{s}$. The third line collects the two-loop counterterm classes $\beta_1 k^2 P_{\text{1-loop}}$ and $k^4 P_{\rm lin}$ ($\tilde{c}$ among the latter), listed in Appendix B, and the stochastic term $P_{gg}^{s,\rm stoch}$. Under the infrared resummation of Section 7, the tree spectrum, the one-loop terms and the counterterms carry the damping factors assigned there, and the deterministic two-loop term is evaluated on the smooth spectrum $P_{\rm nw}$ with the closed-form completion term added. The deterministic parameters are

$$c \;=\; \big(v,\; b_1,\; \ldots,\; b_{17}\big)\Big|_{v=1}\,, \qquad c^{\rm ctr} \;=\; \big(c_0,\; c_2,\; c_4\big)\,, \tag{8.10}$$

per tracer population and redshift, where the b_i are the 17 bias parameters in the order of Eq. (3.24) and $v = 1$ in the absence of velocity bias. Hence we count 20 deterministic parameters before the two-loop counterterm coefficients, plus the four stochastic ones: $P_{\rm shot}$, a_0, a_2, $a_4^{(P)}$. At $f = 0$ the model contains the same operators as the real-space model of [47], with its $17 + 8 + 3 = 28$ parameters. Every term of the model is written out in the Supplementary Information, Sec. S4.

PRELIMINARY

9 The one-loop bispectrum

The one-loop redshift-space galaxy bispectrum with fourth-order bias, counterterms and stochastic terms was constructed in [24, 25, 60], where the counterterms were shown to renormalize the loop, and the real-space bias loops are those of [32]. We compute it at tree level and one loop on the operator basis of Section 3 in the renormalization scheme of Section 6, so that every parameter shared with the power spectrum has the same definition in both statistics. We adopt the kernels of [60] through third order and indicate below where our counterterms differ from those of that work.

9.1 Model, kernels and loop integrals

We define the redshift-space galaxy bispectrum by

$$\langle \delta_g^s(\mathbf{k}_1)\,\delta_g^s(\mathbf{k}_2)\,\delta_g^s(\mathbf{k}_3)\rangle \;=\; (2\pi)^3\,\delta_D(\mathbf{k}_1+\mathbf{k}_2+\mathbf{k}_3)\,B^s_{ggg}(k_1,k_2,k_3;\mu_1,\mu_2)\,, \tag{9.1}$$

a function of five variables, the three side lengths and two of the line-of-sight cosines $\mu_i=\hat{\mathbf{k}}_i\cdot\hat{\mathbf{z}}$, the third following from closure, $k_1\mu_1+k_2\mu_2+k_3\mu_3=0$. At $f=0$ it depends on the side lengths only. We expand the galaxy field as in Eq. (2.8) with the galaxy kernels $Z_n^{\rm gal}$, needed here through $Z_4^{\rm gal}$. At tree level the bispectrum is given by

$$B_{211} \;=\; 2\,Z_2^{\rm gal}(\mathbf{k}_1,\mathbf{k}_2)\,Z_1^{\rm gal}(\mathbf{k}_1)\,Z_1^{\rm gal}(\mathbf{k}_2)\,P_{\rm lin}(k_1)\,P_{\rm lin}(k_2) \;+\; 2\ \text{cyc.}\,, \tag{9.2}$$

which depends on b_1, b_2, γ_2 and f, and on the power-spectrum coefficient c_0 through the image term of Eq. (8.3). The one-loop correction is the sum of four topologies [60],

$$\begin{aligned}
B_{222} &= 8\int_{\mathbf{q}} Z_2^{\rm gal}(\mathbf{k}_1+\mathbf{q},-\mathbf{q})\,Z_2^{\rm gal}(\mathbf{k}_1+\mathbf{q},\mathbf{k}_2-\mathbf{q})\,Z_2^{\rm gal}(\mathbf{k}_2-\mathbf{q},\mathbf{q}) \\
&\qquad\times P_{\rm lin}(q)\,P_{\rm lin}(|\mathbf{k}_1+\mathbf{q}|)\,P_{\rm lin}(|\mathbf{k}_2-\mathbf{q}|)\,, &(9.3)\\
B_{321,\rm I} &= 6\,Z_1^{\rm gal}(\mathbf{k}_1)\,P_{\rm lin}(k_1)\int_{\mathbf{q}} Z_3^{\rm gal}(-\mathbf{q},\mathbf{q}-\mathbf{k}_2,-\mathbf{k}_1)\,Z_2^{\rm gal}(\mathbf{q},\mathbf{k}_2-\mathbf{q}) \\
&\qquad\times P_{\rm lin}(q)\,P_{\rm lin}(|\mathbf{k}_2-\mathbf{q}|) \;+\; 5\ \text{perm.}\,, &(9.4)\\
B_{321,\rm II} &= 6\,Z_2^{\rm gal}(\mathbf{k}_1,\mathbf{k}_2)\,Z_1^{\rm gal}(\mathbf{k}_2)\,P_{\rm lin}(k_1)\,P_{\rm lin}(k_2)\int_{\mathbf{q}} Z_3^{\rm gal}(\mathbf{k}_1,\mathbf{q},-\mathbf{q})\,P_{\rm lin}(q) \;+\; 5\ \text{perm.}\,, &(9.5)\\
B_{411} &= 12\,Z_1^{\rm gal}(\mathbf{k}_1)\,Z_1^{\rm gal}(\mathbf{k}_2)\,P_{\rm lin}(k_1)\,P_{\rm lin}(k_2)\int_{\mathbf{q}} Z_4^{\rm gal}(\mathbf{k}_1,\mathbf{k}_2,\mathbf{q},-\mathbf{q})\,P_{\rm lin}(q) \;+\; 2\ \text{cyc.}\,, &(9.6)
\end{aligned}$$

with $\int_{\mathbf{q}}=\int d^3q/(2\pi)^3$ and integer prefactors counting the Wick pairings. The loops of $B_{321,\rm II}$ and B_{411} are tadpoles of P_{13} and P_{24} type on a tree vertex. Because every kernel is linear in the couplings, each topology is a trilinear form in the coefficient vector c of Section 4,

$$B^{s,\text{1-loop}}_{ggg}(k_1,k_2,k_3;\mu_1,\mu_2) \;=\; \sum_{\rm topo}\sum_{(i,j,l)} c_i\,c_j\,c_l\;B^{ijl}_{\rm topo}(k_1,k_2,k_3;\mu_1,\mu_2;f)\,, \tag{9.7}$$

with coefficient functions $B^{ijl}_{\rm topo}$ polynomial in f and the cosines.

The kernels through third order are eqs. (2.8)–(2.9) of [60] in our operator basis, and $Z_4^{\rm gal}$ follows from the recursion of Eq. (3.15). All eight cubic and quartic bias parameters of Table 3

PRELIMINARY

type	parameters	count
bias, order 1	b_1	1
bias, order 2	b_2, γ_2	2
bias, order 3	b_3, $\gamma_2^\times$, γ_3, γ_{21}	4
bias, order 4	$\gamma_{21}^\times$, γ_{211}, γ_{22}, γ_{31}	4
counterterms, real space	$\beta_{B,a},\dots,\beta_{B,e}$	5
counterterms, redshift space	$C_1,\dots,C_5$, $C_7,\dots,C_{11}$, e_5	11
counterterm, velocity dispersion	$\tilde{c}$	1
stochastic, shared with P_{gg}^s	$P_{\rm shot}$, a_0, a_2	3
stochastic, $\bar{n}^{-2}$	$A_{\rm shot}$, a_1, a_6	3
stochastic, mixed tree	$B_{\rm shot}$	1
stochastic, mixed counterterm	a_3, a_4, a_5, $a_7,\dots,a_{12}$	9
stochastic, mixed one-loop	d_2, $d_{\mathcal{G}_2}$, d_{Γ_3}	3
total		47 (46 enter the bispectrum)

Table 3: Parameters of the one-loop galaxy bispectrum in redshift space: 11 bias parameters through fourth order, 17 counterterm coefficients (five real-space shapes [60], eleven redshift-space structures $R_1,\dots,R_{11}$ of Section 9.2, which the table lists as $C_1,\dots,C_5$, $C_7,\dots,C_{11}$ and e_5, and $\tilde{c}$ of Eq. (9.14)) and the 19 stochastic parameters of [11]. With $P_{\rm shot}$, a_0, a_2 shared with the power spectrum and counted once, the total is 47, of which 46 enter the bispectrum (a_2 does not). The image term of Eq. (8.3) and $B_{\rm ctr,II}$ of Eq. (9.15) use the power-spectrum c_0, c_2, c_4 and add no parameter; $a_4^{(P)}$ of Eq. (8.2) is distinct from a_4.

enter the one-loop bispectrum, and only γ_{21} among them contributes to the renormalized one-loop power spectrum [60]. We call each coefficient function $B_{\rm topo}^{ijl}$ a shape. The four topologies have 568 one-loop shapes in 190 signatures (distinct fillings of the kernel vertices by velocity structures), or 586 in 202 with the 18 tree shapes. Both counts are upper bounds on the number of nonvanishing coefficient functions. We evaluate the coefficient functions on canonically ordered closed triples, $k_1 \le k_2 \le k_3 \le k_1 + k_2$, with sides on the geometric grid

$$k_t \;=\; 0.01 \times 30^{\,(t-1)/23}\; h/\mathrm{Mpc}\,, \qquad t = 1,\dots,24\,, \tag{9.8}$$

which runs from 0.01 to $0.30\,h\,\mathrm{Mpc}^{-1}$ with spacing ratio $30^{1/23} \approx 1.16$. The grid contains 786 closed configurations, listed together with the number of shapes in each topology in the Supplementary Information, Sec. S6.

9.2 Counterterms and renormalization

At order k^2 relative to tree level the counterterms enter through second-order counterkernels on one vertex,

$$B_{\rm ctr} \;=\; 2\,Z_1^{\rm gal}(\mathbf{k}_1)\,Z_1^{\rm gal}(\mathbf{k}_2)\,\big(F_2^{\rm ctr} + Z_2^{\rm ctr}\big)(\mathbf{k}_1,\mathbf{k}_2)\,P_{\rm lin}(k_1)\,P_{\rm lin}(k_2) \;+\; \text{cyc.}\,, \tag{9.9}$$

where $F_2^{\rm ctr}$ is the sum of the five real-space shapes $(k_1^2+k_2^2)F_2$, $k_3^2 F_2$, $(k_1^2+k_2^2)\,\kappa$, $k_3^2\,\kappa$ and $\mathbf{k}_1\cdot\mathbf{k}_2$, with $\kappa = (\hat{\mathbf{k}}_1\cdot\hat{\mathbf{k}}_2)^2 - 1$ [32]. Each of these shapes is divided by $k_{\rm NL}^2$, with the convention $k_{\rm NL} = 0.45\,h\,\mathrm{Mpc}^{-1}$, and multiplied by one of the free coefficients $\beta_{B,a},\dots,\beta_{B,e}$. The redshift-space

PRELIMINARY

counterkernel $Z_2^{\rm ctr}$ contains eleven structures $R_1,\dots,R_{11}$, each divided by $k_{\rm NL}^2$ and multiplied by a free coefficient: ten local line-of-sight contact structures and the nonlocal velocity counterterm e_5 of [11, 25]. Eight of the eleven are structures of eq. (2.12) of [60], $R_1,\dots,R_5 = C_1,\dots,C_5$ and $R_6, R_7, R_8 = C_7, C_8, C_9$. The structure given there as $C_6 = f k_{3z}^3\,[(\mu_1/k_1)(\mu_2 - \frac{1}{3}) + (\mu_2/k_2)(\mu_1 - \frac{1}{3})]$ contains a term odd under the reflection $\hat{\mathbf{z}} \to -\hat{\mathbf{z}}$, which cannot appear in the kernel of a scalar statistic. Instead, the s_{zz} projection of its parent operator $u_{(i}s_{jk)}$ (s_{ij} being the traceless tidal tensor) gives

$$C_6^{\rm corr} \;=\; C_8 \;-\; \tfrac{1}{3}\,C_7 \qquad \text{(with } k_{3z} = k_1\mu_1 + k_2\mu_2 \text{ and the } f\text{-powers absorbed into the coefficients)}\,, \tag{9.10}$$

and the nine structures of that reference then have rank 8. To these eight we add three structures,

$$R_9 \;=\; C_{10} \;=\; k_{3z}^2\left(\mu_1^2 + \mu_2^2 - \tfrac{2}{3}\right), \tag{9.11}$$

$$R_{10} \;=\; C_{11} \;=\; k_{3z}\left[\tfrac{1}{2}\,(\mathbf{k}_1\cdot\mathbf{k}_2)\Big(\frac{\mu_1}{k_1} + \frac{\mu_2}{k_2}\Big) - \tfrac{1}{6}\,k_{3z}\right], \tag{9.12}$$

$$R_{11} \;=\; e_5 \;=\; k_{3z}^2\,\frac{(\mathbf{k}_1\cdot\mathbf{k}_2)(\mathbf{k}_1\cdot\mathbf{k}_3)(\mathbf{k}_2\cdot\mathbf{k}_3)}{k_1^2\,k_2^2\,k_3^2}\,. \tag{9.13}$$

The structures C_{10} and C_{11} descend from $\delta\,s_{ij}$ and $s_{ij}\partial_j\delta$ at f^0. Neither has a linear piece, so the power-spectrum relations of [60] among C_1, C_2, C_5 still hold in principle. However, we do not impose those two relations and keep all eleven coefficients free.

Both C_{10} and C_{11} lie in the span of the fourteen quadratic counterterm kernels $e_i^{K_2}$ of [24, 25]: on closed triangles $C_{10} = -\frac{4}{f^2}\,e_{12}^{K_2} + \frac{4}{3f^2}\,e_{14}^{K_2}$ and $C_{11} = \frac{1}{f}\,e_6^{K_2} + \frac{2}{f^2}\,e_{10}^{K_2} - \frac{2}{f}\,e_{12}^{K_2} + \frac{1}{3f^2}\,e_{14}^{K_2}$. They are absent only from the printed set of [60]; C_{11} also lies in the span of the redshift-space counterterms of [11, 46], and so does C_{10} when the symmetrization of those counterterms is interpreted consistently with the linear counterkernel used there. We do not admit projections of level-two (u_z^2) composites such as $(\partial_z\partial_z\nabla^{-2})(\delta^2)$, which would raise the count to thirteen. We list the structures with their origins in Appendix B.

We add one quartic structure to the linear counterkernel,

$$Z_1^{{\rm ctr}\,(s)} \;\to\; Z_1^{{\rm ctr}\,(s)} \;-\; \frac{\tilde{c}}{2}\,\frac{k^4}{k_{\rm NL}^4}\,\mu^4 f^4\left(b_1 + f\mu^2\right), \tag{9.14}$$

the $k^4\mu^4$ velocity-dispersion term of [11, 74], expected to absorb the leading nonperturbative line-of-sight contamination near the scale cut. In total the counterterms then have 17 free coefficients (five in real space, eleven in redshift space and $\tilde{c}$), two more than the $14 + 1$ of [11]. Both constructions span the same contact space once the powers of f are absorbed into the coefficients, and they agree on the nonlocal velocity term $e_5 = R_{11}$, which we keep free. The two additional parameters are free redshift-space coefficients on that common space, eleven here against nine there. The c_0 image term is of the same order in k and linearly independent of $R_1,\dots,R_{11}$ (joint rank 12, established numerically at random configurations).

We regulate the self-loop topologies $B_{321,\rm II}$ and B_{411} by a hard loop-momentum cutoff. Their hard region $q \gg k_i$ then makes two contributions. The first is the σ^2 tadpole, with $\sigma^2 = 1.888$ on the support $10^{-3} \le q \le 1\,h\,{\rm Mpc}^{-1}$ for the fiducial linear spectrum. Through it the operators on the loop shift b_1, b_2, γ_2 by exactly the constants of the power-spectrum conditions, Eqs. (3.26) and (6.7)–(6.9) (Supplementary Information, Sec. S4). In particular, the renormalized b_1, b_2, γ_2

PRELIMINARY

absorb the bispectrum tadpoles with no new condition, and the velocity mean $f\mu^2 b_2/6$ is removed by $\langle \delta_g \rangle = 0$.

The second hard contribution to the self-loop topologies is the single-hard part, weighted by the moment $\sigma^2_{-2} = 51.36\,(\mathrm{Mpc}/h)^2$ of Eq. (6.5) on the same support. In $B_{321,\mathrm{II}}$ it acts as Z_1^{ctr} with the P_{13} coefficients on the side carrying the loop, and the model therefore contains

$$B_{\mathrm{ctr,II}} \;=\; 2\sum_{(i,j)} Z_1^{\mathrm{ctr}}(\mathbf{k}_j)\, Z_1^{\mathrm{gal}}(\mathbf{k}_i)\, Z_2^{\mathrm{gal}}(\mathbf{k}_i,\mathbf{k}_j)\, P_{\mathrm{lin}}(k_i)\, P_{\mathrm{lin}}(k_j)\,, \tag{9.15}$$

where the sum runs over the six ordered pairs of sides. This term is $B^{\mathrm{ctr.\,II}}$, the last line of eq. (37) of [11]. Its coefficients are the power-spectrum amplitudes c_0, c_2, c_4 of Eq. (8.9), without $\tilde{c}$, and it introduces no new parameter. The loop of $B_{321,\mathrm{II}}$ shifts these coefficients by

$$\begin{aligned} \delta c_0 &= \sigma^2_{-2}\Big[-\tfrac{61}{630}\,b_1 - \tfrac{32}{35}\,\gamma_2 + \tfrac{16}{15}\,\gamma_{21}\Big]\,, \\ \delta c_2 &= \sigma^2_{-2}\Big[-\tfrac{3}{10}\,f + \tfrac{f\,b_1}{105} - \tfrac{8}{35}\,f^2 - \tfrac{f^2 b_1}{6}\Big]\,, \qquad \delta c_4 \;=\; \sigma^2_{-2}\Big[-\tfrac{23}{105}\,f^2 - \tfrac{f^3}{6}\Big]\,, \end{aligned} \tag{9.16}$$

exactly as P_{13} does, so one set of c_0, c_2, c_4, determined by the power-spectrum renormalization conditions alone, absorbs the single-hard parts of P_{13} and of $B_{321,\mathrm{II}}$ together.

In B_{411} the single-hard part lies in the span of the five real-space shapes, $R_1,\dots,R_{11}$ and the image term of Eq. (8.3), to residuals of at most 1.3×10^{-7} on 40 configurations. The image term enters this decomposition with half the coefficient found for $B_{321,\mathrm{II}}$. Hence the subtraction in B_{411} also requires it. If we change the support of P_{lin} inside the loop, c_0, c_2, c_4 shift by a further computable constant and $\tilde{c}$ does not (Supplementary Information, Sec. S6). With two spectra in the loop, $B_{321,\mathrm{I}}$ has no σ^2 tadpole; its hard region gives a P_{22}-type constant, proportional to $\int P_{\mathrm{lin}}^2\, q^2\, dq$, with the momentum structure of the stochastic terms, whose amplitudes absorb it.

9.3 Stochastic bispectrum and parameter count

The stochastic bispectrum arises from the moments of the noise field and consists of the stochastic terms of [11], grouped into the five contributions of Eqs. (8.4)–(8.7) in Section 8. Only the mixed one-loop term contains genuine loop integrals, two-point loops of the P_{22} and P_{13} class with one noise leg [11]. Its three parameters, d_2, $d_{\mathcal{G}_2}$ and d_{Γ_3}, multiply shapes not among the 568 one-loop shapes above; their integrands and evaluation are given in the Supplementary Information, Sec. S6. We list all parameters by type in Table 3. The deterministic bias operators through fourth order number $1+2+4+4=11$. Composite local-evolution operators such as δ^4 and $\delta^2\mathcal{G}_2(\Phi_v)$ never enter the one-loop bispectrum, and we drop them [60]. With the 17 counterterm coefficients and the 19 stochastic parameters the total is $11+17+19=47$, against the 45 of [11], the difference being the two additional redshift-space counterterm coefficients of Section 9.2. Of the 47 parameters, 46 enter the bispectrum, since a_2 appears only in the power spectrum.

9.4 Soft poles and quadrature accuracy

As the loop momentum $\mathbf{q} \to 0$ each of the four integrands develops the eikonal pole of its soft spectrum argument,

$$b_X(\mathbf{q}) \underset{q\to0}{\sim} k^2\big(\hat{\mathbf{k}}\cdot\hat{\mathbf{q}}\big)^2\,\frac{P_{\mathrm{lin}}(q)}{q^2}\,, \qquad \frac{dB_X}{d\ln q} \;\sim\; q^{\,1+n} \quad \text{for} \quad P_{\mathrm{lin}} \propto q^{\,n}\,, \tag{9.17}$$

PRELIMINARY

where b_X is the integrand of topology X and k an external side. The contribution of the pole to the integral diverges only for spectral index $n \leq -1$, in which case the divergences cancel in the sum over topologies as the equivalence principle requires [13]. For the physical soft index $n_{\rm eff}(q \to 0) = +0.96$ each topology is separately integrable. At every triangle, bias point and growth rate the soft coefficients of the two topologies that share the soft $Z_1^{\rm gal}$ leg are equal and opposite,

$$b^{\rm soft}_{321,\rm I} \;=\; -\,b^{\rm soft}_{411}\,, \tag{9.18}$$

an eikonal identity that holds numerically in the b_1^3 class at $q = 10^{-4}\,h\,\mathrm{Mpc}^{-1}$ to 1.2×10^{-5} at the equilateral, scalene and flattened configurations and to 1.3×10^{-4} at the most squeezed one. The pole of the summed integrand at the origin is then that of $b_{321,\rm II} + b_{222}$, and we integrate all four topologies together,

$$B^{s,\text{1-loop}}_{ggg} \;=\; \int_{\mathbf{q}} \Big[\, b_{222} + b_{321,\rm I} + b_{321,\rm II} + b_{411} \,\Big](\mathbf{q})\,. \tag{9.19}$$

Away from the origin, b_{222} and $b_{321,\rm I}$ have integrable singularities at image points, where another spectrum argument vanishes. We integrate each such singularity in a windowed patch in local coordinates (the patches, the cutoff variation and the quadrature depths are given in the Supplementary Information, Sec. S6).

We define the quadrature error of a shape as the relative difference between two quadrature depths of the same integral, with the denominator bounded below by five percent of the median magnitude over the grid so that sign-crossing configurations cannot inflate it. We measure this error configuration by configuration in the b_1^3 coupling class, 4 of the 568 shapes, on all 786 configurations. At the baseline pair of depths the median errors are 1.0×10^{-4} for b_{222} and 2.0×10^{-4} for $b_{321,\rm I}$. Both self-loop integrands are smooth, with no image points. For $b_{321,\rm II}$ and b_{411} we compare the two depths shape by shape at a full-bias point on 20 of the 786 configurations, where the median is 3.2×10^{-4} for both. One shape of b_{411} at a sign-crossing configuration differs by 2.0×10^{-2} under the relative convention and by 7.1×10^{-4} of the shape's own median on the absolute scale, and each topology summed over shapes at that bias point moves by at most 3.19×10^{-4}.

9.5 Tree level and the bin average

The tree bispectrum of Eq. (9.2) [60, 62] is bilinear in the spectrum with closed-form coefficients,

$$B_{211} \;=\; \sum_{(i,j)} P_{\rm lin}(k_i)\, P_{\rm lin}(k_j) \sum_{m=1}^{14} c_m\, T_m^{(ij)}(k_1, k_2, k_3; \mu_1, \mu_2)\,, \tag{9.20}$$

where the outer sum runs over the three cyclic pairs and each $T_m^{(ij)}$ is rational in the sides and cosines. The coupling monomials are

$$c_m \;\in\; \big\{\, b_1^3,\; b_1^2 b_2,\; b_1^2\gamma_2,\; b_1^2 f,\; b_1 b_2 f,\; b_1\gamma_2 f,\; b_1 f^2,\; b_2 f^2,\; \gamma_2 f^2,\; f^3,\; b_1^3 f,\; b_1^2 f^2,\; b_1 f^3,\; f^4 \,\big\}\,, \tag{9.21}$$

ten of total order three and four of order four, plus the three image-term monomials $c_0 b_1^2 f$, $c_0 b_1 f^2$, $c_0 f^3$. We parametrize the second cosine by an azimuth ϕ about $\hat{\mathbf{k}}_1$,

$$\mu_2 \;=\; \mu_1\,(\hat{\mathbf{k}}_1 \cdot \hat{\mathbf{k}}_2) \;+\; \sqrt{1-\mu_1^2}\,\sqrt{1-(\hat{\mathbf{k}}_1 \cdot \hat{\mathbf{k}}_2)^2}\,\cos\phi\,. \tag{9.22}$$

PRELIMINARY

The tree integrand then contains azimuthal harmonics through $\cos 6\phi$ and even powers through μ_1^8. Hence an eight-node Gauss–Legendre rule in μ_1 (exact through degree fifteen) and an eight-point uniform rule in ϕ (exact through the seventh harmonic) integrate every angular monomial of the tree theory exactly for the monopole and the μ_1-referenced quadrupole.

A measured bispectrum is an average over a bin b, a triple of side-length shells, and the prediction is the same average over the fundamental triangles of a periodic volume of side L,

$$\langle B\rangle_b \;=\; \frac{1}{N_b} \sum_{\substack{\mathbf{n}_1+\mathbf{n}_2+\mathbf{n}_3=0 \\ (|\mathbf{k}_{\mathbf{n}_1}|,|\mathbf{k}_{\mathbf{n}_2}|,|\mathbf{k}_{\mathbf{n}_3}|)\in b}} B(\mathbf{k}_{\mathbf{n}_1},\mathbf{k}_{\mathbf{n}_2},\mathbf{k}_{\mathbf{n}_3})\,, \tag{9.23}$$

where $\mathbf{k}_{\mathbf{n}} = k_f\,\mathbf{n}$ with $k_f = 2\pi/L$, moduli are assigned to half-open shells $[k, k+\Delta k)$ and N_b counts the closed triples in the bin. We include multipole weights [62, 64] in the same sum, which contains only closed triangles even for bins straddling the triangle inequality. Point evaluation at effective side lengths differs from this average by a few percent at tree level [58]. Bin quadrature [60] and discreteness-weighted continuum integrals [45] approximate the sum. Instead, we evaluate the discrete sum itself, for loop and tree terms alike, because it factorizes.

After contraction with the spectrum the predicted bispectrum is a finite sum $B = \sum_m S_m(k_1,k_2,k_3)\,\mu_1^{i_m}\mu_2^{j_m}$ with coefficients S_m smooth in the sides. The bin average therefore splits into a geometric part, computed once per volume and binning, and a theory part,

$$\langle B\rangle_b \;=\; \frac{1}{N_b}\sum_m\sum_\nu A_m[b;\nu]\;S_m(\nu)\,, \qquad A_m[b;\nu] \;=\; \sum_{\text{triangles}\,\in\, b} w_\nu(k_1,k_2,k_3)\;\mu_1^{i_m}\mu_2^{j_m}\,, \tag{9.24}$$

where ν runs over the grid configurations of Eq. (9.8), w_ν is the interpolation stencil assigning a triangle's sides to the grid, and each monomial is evaluated at the triangle's own orientation. The operator $A_m[b;\nu]$ is a sparse matrix (its construction and the azimuthal reduction are given in the Supplementary Information, Sec. S6). At tree level we need no stencil: the tree bispectrum of Eq. (9.20) is a closed-form function of the sides, and its bin average is therefore exact.

10 The one-loop trispectrum

On the parallelogram configurations $(\mathbf{k}, -\mathbf{k}, \mathbf{k}', -\mathbf{k}')$ the connected galaxy four-point function in redshift space is the non-Gaussian part of the power spectrum covariance [9, 66], and on general quadrilaterals it is an observable. We construct its one-loop correction, the contact subtraction of its self-loop types and its stochastic sector from the kernels Z_n^{gal}, $n \le 5$.

10.1 Model, operator content and tree level

The redshift-space galaxy trispectrum is the connected four-point function

$$\langle \delta_g^s(\mathbf{k}_1)\,\delta_g^s(\mathbf{k}_2)\,\delta_g^s(\mathbf{k}_3)\,\delta_g^s(\mathbf{k}_4)\rangle_{\mathrm{c}} \;=\; (2\pi)^3\,\delta_D(\mathbf{k}_1+\mathbf{k}_2+\mathbf{k}_3+\mathbf{k}_4)\;T^s_{gggg}(\mathbf{k}_1,\mathbf{k}_2,\mathbf{k}_3,\mathbf{k}_4;\hat{\mathbf{z}})\,, \tag{10.1}$$

a function of six shape variables of the closed quadrilateral and two orientation angles of the line of sight, of which the two angles drop out at $f = 0$. By Wick's theorem we organize the contributions

PRELIMINARY

by the four kernel orders, which form the partitions $(3,1,1,1)$ and $(2,2,1,1)$ of six at tree level and the five partitions of eight at one loop,

$$(5,1,1,1)\,,\quad (4,2,1,1)\,,\quad (3,3,1,1)\,,\quad (3,2,2,1)\,,\quad (2,2,2,2)\,, \tag{10.2}$$

which resolve into nine contraction types. The model is the sum

$$T^s_{gggg} \;=\; T_{\text{tree}}{+}T_{\text{1-loop}}{+}T_{\text{ctr}}{+}T_{\text{stoch}}\,, \qquad T_{\text{tree}} \;=\; T_{3111}{+}T_{2211}\,, \qquad T_{\text{1-loop}} \;=\; \sum_{9\ \text{types}} T_{\text{type}}\,, \tag{10.3}$$

where T_{ctr} denotes the counterterms and we construct T_{stoch} in Section 10.4. We leave the counterterms of the one-loop trispectrum to future work, where they are to be constructed in the operator basis made consistent with the renormalization of the matter kernels [47]. In the multiplicity convention of [8, 72] the tree terms read

$$\begin{aligned} T_{3111} \;&= 6\, Z_3^{\text{gal}}(\mathbf{k}_1,\mathbf{k}_2,\mathbf{k}_3)\, Z_1^{\text{gal}}(\mathbf{k}_1)\, Z_1^{\text{gal}}(\mathbf{k}_2)\, Z_1^{\text{gal}}(\mathbf{k}_3)\, P_{\text{lin}}(k_1)\, P_{\text{lin}}(k_2)\, P_{\text{lin}}(k_3) \;+\; 3\ \text{perm.}\,, \\ T_{2211} \;&= 4\, Z_2^{\text{gal}}(-\mathbf{k}_1-\mathbf{k}_2,\mathbf{k}_2)\, Z_2^{\text{gal}}(\mathbf{k}_1+\mathbf{k}_2,\mathbf{k}_3)\, Z_1^{\text{gal}}(\mathbf{k}_2)\, Z_1^{\text{gal}}(\mathbf{k}_3) \\ &\qquad \times\, P_{\text{lin}}(|\mathbf{k}_1+\mathbf{k}_2|)\, P_{\text{lin}}(k_2)\, P_{\text{lin}}(k_3) \;+\; 11\ \text{perm.}\,, \end{aligned} \tag{10.4}$$

with the momentum routing of Appendix A of [8], $F_n^{(s)} \to Z_n^{\text{gal}}$, and one Z_1^{gal} per external first-order vertex. Under the Alcock–Paczynski distortion with dilation parameters $(q_\parallel, q_\perp)$ the observed trispectrum is

$$T_{\text{obs}}(\mathbf{k}') \;=\; (q_\parallel\, q_\perp^2)^{-3}\, T(\mathsf{A}\,\mathbf{k}')\,, \qquad \mathsf{A} \;=\; \text{diag}\big(1/q_\perp,\ 1/q_\perp,\ 1/q_\parallel\big)\,, \tag{10.5}$$

with one volume factor $(q_\parallel q_\perp^2)^{-1}$ per linear spectrum, three at tree level. We apply this map only at tree level.

Which of the 29 operators of Table 1 enter follows from their renormalized kernels in the nine contraction types below, and the resulting count agrees with the real-space analysis of [5]. The one-loop trispectrum admits 1, 3, 7, 15 and 24 bias operators of order at most one to five, against 1, 3, 7, 11 for the one-loop bispectrum and 1, 3, 7, 11, 17 for the two-loop power spectrum. The trispectrum admits more fourth-order operators than the bispectrum because the four quartic products of $\Pi^{[1]}_{ij} = (\partial_i\partial_j/\nabla^2)\,\delta$, whose renormalized kernels vanish in the self-contracted configurations of P_{24} and B_{411}, survive in T_{4211b} and, through their evolved fifth-order kernels, in T_{5111}. At fifth order Z_5^{gal} enters only T_{5111}, where nine of the 14 new operators contribute and the five fifth-order LE operators (products of five $\Pi^{[1]}$) drop out. Thus the coefficient vector is the 17-vector of Eq. (3.24) extended by seven,

$$b^i_T \;=\; \big(b^i \text{ of Eq. (3.24)};\ b_4,\ \gamma_2^{\times\times},\ \gamma_3^{\times},\ \gamma_2^{\text{sq}};\ \gamma_{21}^{\times\times},\ \gamma_{21,2},\ \gamma_{211}^{\times}\big)\,, \tag{10.6}$$

namely four fourth-order LE operators redundant for the power spectrum and bispectrum and three fifth-order NLE products without a finite P_{15} contribution.

10.2 Contraction types and one-loop integrands

A Wick pairing of the eight linear fields into four linear spectra is a connected multigraph on the four kernel vertices with four internal lines, each vertex of degree equal to its kernel order. We

PRELIMINARY

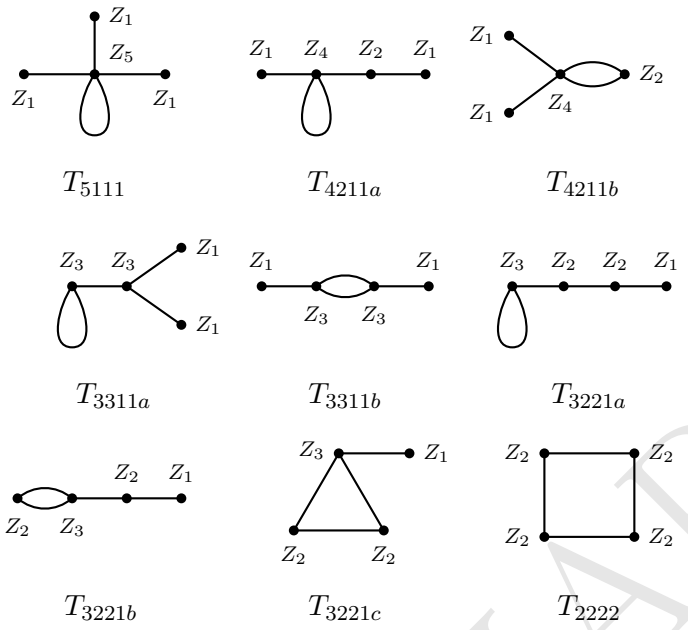

Figure 4: The nine one-loop contraction types of the redshift-space galaxy trispectrum, drawn as connected multigraphs on the four kernel vertices $Z_n = Z_n^{\rm gal}$ with four internal lines, each standing for a linear power spectrum; every vertex also carries one external momentum, not drawn. The one independent cycle of Eq. (10.7) is a self-loop $(\mathbf{q}, -\mathbf{q})$ inside one kernel (T_{5111}, T_{4211a}, T_{3311a}, T_{3221a}), a doubled line (T_{4211b}, T_{3311b}, T_{3221b}), a triangle (T_{3221c}) or a square (T_{2222}). Subscripts give the kernel-order partition of Eq. (10.2), letters distinguish the types within a partition, and the integrands are those of Eq. (10.9).

allow self-loops, $(\mathbf{q}, -\mathbf{q})$ pairings inside one kernel. Connectedness with four vertices and four lines leaves exactly one independent cycle,

$$I - V + 1 \;=\; 4 - 4 + 1 \;=\; 1\,, \tag{10.7}$$

so the loop is a self-loop, a two-cycle (a doubled line), a three-cycle or a four-cycle. The contraction types are its inequivalent placements. The partitions $(5,1,1,1)$ and $(2,2,2,2)$ admit one placement each, the self-loop at the fifth-order vertex and the four-cycle. Both $(4,2,1,1)$ and $(3,3,1,1)$ admit two, a self-loop at a highest-order vertex or a two-cycle between the two vertices of order above one. The partition $(3,2,2,1)$ admits three, a self-loop at the third-order vertex on a path 3–2–2–1, a two-cycle between the third-order and a second-order vertex, or a three-cycle through the three vertices of order at least two. The five partitions thus give

$$1 + 2 + 2 + 3 + 1 \;=\; 9 \tag{10.8}$$

contraction types, T_{5111}, $T_{4211a,b}$, $T_{3311a,b}$, $T_{3221a,b,c}$ and T_{2222} (Fig. 4 and Table 4), matching type by type the nine amplitudes of [8] and the nine diagrams of [72].

With $\int_{\mathbf{q}} = \int d^3q/(2\pi)^3$ and every Z_n standing for $Z_n^{\rm gal}$, the nine one-loop integrands are

$$T_{5111} \;= 60 \int_{\mathbf{q}} Z_5(\mathbf{q}, -\mathbf{q}, \mathbf{k}_2, \mathbf{k}_3, \mathbf{k}_4)\, Z_1(\mathbf{k}_2) Z_1(\mathbf{k}_3) Z_1(\mathbf{k}_4)\; P_{\rm lin}(q) P_{\rm lin}(k_2) P_{\rm lin}(k_3) P_{\rm lin}(k_4) + 3 \text{ perm.}\,,$$

PRELIMINARY

partition	type	cycle	multiplicity	permutations	pieces at the parallelogram	loop-dependent spectra
$(3,1,1,1)$	T_{3111} (tree)	none	$6 = 3!$	4	4	none
$(2,2,1,1)$	T_{2211} (tree)	none	$4 = (2!)^2$	12	8	none
$(5,1,1,1)$	T_{5111}	self-loop in Z_5	$60 = 5!/2!$	4	4	$P_{\rm lin}(q)$
$(4,2,1,1)$	T_{4211a}	self-loop in Z_4; reducible line to Z_2	$24 = 4!$	24	16	$P_{\rm lin}(q)$
	T_{4211b}	doubled line Z_4–Z_2	$24 = 4!$	12	12	$P_{\rm lin}(q)\,P_{\rm lin}(\lvert\mathbf{q}+\mathbf{k}_1\rvert)$
$(3,3,1,1)$	T_{3311a}	self-loop in one Z_3; star at the other	$18 = (3!)^2/2!$	12	12	$P_{\rm lin}(q)$
	T_{3311b}	doubled line Z_3–Z_3	$18 = (3!)^2/2!$	12	12	$P_{\rm lin}(q)\,P_{\rm lin}(\lvert\mathbf{q}+\mathbf{k}_{14}\rvert)$
$(3,2,2,1)$	T_{3221a}	self-loop in Z_3; path 3–2–2–1	$12 = 3!\,2!$	24	16	$P_{\rm lin}(q)$
	T_{3221b}	doubled line Z_3–Z_2; path 2–1	$12 = 3!\,2!$	24	16	$P_{\rm lin}(q)\,P_{\rm lin}(\lvert\mathbf{q}+\mathbf{k}_1\rvert)$
	T_{3221c}	triangle Z_3–Z_2–Z_2; line to Z_1	$24 = 3!\,(2!)^2$	12	12	$P_{\rm lin}(q)\,P_{\rm lin}(\lvert\mathbf{q}+\mathbf{k}_{14}\rvert)\,P_{\rm lin}(\lvert\mathbf{q}-\mathbf{k}_2\rvert)$
$(2,2,2,2)$	T_{2222}	square on the four Z_2	$16 = (2!)^4$	3	3	$P_{\rm lin}(q)\,P_{\rm lin}(\lvert\mathbf{q}-\mathbf{k}_2\rvert)\,P_{\rm lin}(\lvert\mathbf{q}-\mathbf{k}_{23}\rvert)\,P_{\rm lin}(\lvert\mathbf{q}+\mathbf{k}_1\rvert)$
one loop	9 types			127	103	

Table 4: Contraction types of the redshift-space galaxy trispectrum at tree level and one loop, with the one independent cycle of Eq. (10.7) named in the third column. The multiplicity is the Wick symmetry factor multiplying one representative term in Eqs. (10.4) and (10.9); it equals the factorials of eqs. (60)–(70) of [72] and eqs. (A5)–(A15) of [8] in every row. "Permutations" counts the inequivalent external-label permutations, and the next column those that remain nonzero on the parallelogram configurations of Eq. (10.16), where a reducible line can carry zero momentum and $P_{\rm lin}(0) = 0$ removes the piece. The last column lists the linear spectra whose argument depends on the loop momentum $\mathbf{q}$ in the routing of Eq. (10.9), with $\mathbf{k}_{ij} = \mathbf{k}_i + \mathbf{k}_j$.

$$
\begin{aligned}
T_{4211a} &= 24 \int_{\mathbf{q}} Z_4(\mathbf{q}, -\mathbf{q}, \mathbf{k}_2{+}\mathbf{k}_3, \mathbf{k}_4)\, Z_2(-\mathbf{k}_2{-}\mathbf{k}_3, \mathbf{k}_3)\, Z_1(\mathbf{k}_3) Z_1(\mathbf{k}_4) \\
&\qquad \times P_{\rm lin}(q) P_{\rm lin}(|\mathbf{k}_2{+}\mathbf{k}_3|) P_{\rm lin}(k_3) P_{\rm lin}(k_4) + 23 \text{ perm.}\,, \\
T_{4211b} &= 24 \int_{\mathbf{q}} Z_4(\mathbf{k}_1{+}\mathbf{q}, -\mathbf{q}, \mathbf{k}_3, \mathbf{k}_4)\, Z_2(-\mathbf{q}{-}\mathbf{k}_1, \mathbf{q})\, Z_1(\mathbf{k}_3) Z_1(\mathbf{k}_4) \\
&\qquad \times P_{\rm lin}(|\mathbf{q}{+}\mathbf{k}_1|) P_{\rm lin}(q) P_{\rm lin}(k_3) P_{\rm lin}(k_4) + 11 \text{ perm.}\,, \\
T_{3311a} &= 18 \int_{\mathbf{q}} Z_3(\mathbf{q}, -\mathbf{q}, -\mathbf{k}_1)\, Z_3(\mathbf{k}_1, \mathbf{k}_3, \mathbf{k}_4)\, Z_1(\mathbf{k}_3) Z_1(\mathbf{k}_4) \\
&\qquad \times P_{\rm lin}(q) P_{\rm lin}(k_1) P_{\rm lin}(k_3) P_{\rm lin}(k_4) + 11 \text{ perm.}\,, \\
T_{3311b} &= 18 \int_{\mathbf{q}} Z_3(\mathbf{q}, -\mathbf{q}{-}\mathbf{k}_1{-}\mathbf{k}_4, \mathbf{k}_4)\, Z_3(-\mathbf{q}, \mathbf{q}{+}\mathbf{k}_1{+}\mathbf{k}_4, \mathbf{k}_3)\, Z_1(\mathbf{k}_3) Z_1(\mathbf{k}_4) \\
&\qquad \times P_{\rm lin}(q) P_{\rm lin}(|\mathbf{q}{+}\mathbf{k}_1{+}\mathbf{k}_4|) P_{\rm lin}(k_3) P_{\rm lin}(k_4) + 11 \text{ perm.}\,, \\
T_{3221a} &= 12 \int_{\mathbf{q}} Z_3(\mathbf{q}, -\mathbf{q}, -\mathbf{k}_1)\, Z_2(\mathbf{k}_1, \mathbf{k}_3{+}\mathbf{k}_4)\, Z_2(-\mathbf{k}_3{-}\mathbf{k}_4, \mathbf{k}_4)\, Z_1(\mathbf{k}_4) \\
&\qquad \times P_{\rm lin}(q) P_{\rm lin}(k_1) P_{\rm lin}(|\mathbf{k}_3{+}\mathbf{k}_4|) P_{\rm lin}(k_4) + 23 \text{ perm.}\,, \\
T_{3221b} &= 12 \int_{\mathbf{q}} Z_3(\mathbf{q}{+}\mathbf{k}_1, -\mathbf{q}, \mathbf{k}_3{+}\mathbf{k}_4)\, Z_2(-\mathbf{k}_1{-}\mathbf{q}, \mathbf{q})\, Z_2(-\mathbf{k}_3{-}\mathbf{k}_4, \mathbf{k}_4)\, Z_1(\mathbf{k}_4) \\
&\qquad \times P_{\rm lin}(q) P_{\rm lin}(|\mathbf{k}_1{+}\mathbf{q}|) P_{\rm lin}(|\mathbf{k}_3{+}\mathbf{k}_4|) P_{\rm lin}(k_4) + 23 \text{ perm.}\,, \\
T_{3221c} &= 24 \int_{\mathbf{q}} Z_3(\mathbf{q}, -\mathbf{k}_1{-}\mathbf{k}_4{-}\mathbf{q}, \mathbf{k}_4)\, Z_2(-\mathbf{q}, \mathbf{q}{-}\mathbf{k}_2)\, Z_2(\mathbf{k}_2{-}\mathbf{q}, \mathbf{k}_1{+}\mathbf{k}_4{+}\mathbf{q})\, Z_1(\mathbf{k}_4) \\
&\qquad \times P_{\rm lin}(q) P_{\rm lin}(|\mathbf{k}_1{+}\mathbf{k}_4{+}\mathbf{q}|) P_{\rm lin}(|\mathbf{q}{-}\mathbf{k}_2|) P_{\rm lin}(k_4) + 11 \text{ perm.}\,,
\end{aligned}
$$

PRELIMINARY

$$T_{2222} = 16 \int_{\mathbf{q}} Z_2(\mathbf{q}, -\mathbf{k}_1{-}\mathbf{q})\, Z_2(-\mathbf{q}, \mathbf{q}{-}\mathbf{k}_2)\, Z_2(\mathbf{k}_2{-}\mathbf{q}, \mathbf{q}{-}\mathbf{k}_2{-}\mathbf{k}_3)\, Z_2(\mathbf{k}_2{+}\mathbf{k}_3{-}\mathbf{q}, \mathbf{q}{+}\mathbf{k}_1) \times P_{\rm lin}(q) P_{\rm lin}(|\mathbf{q}{-}\mathbf{k}_2|) P_{\rm lin}(|\mathbf{q}{-}\mathbf{k}_2{-}\mathbf{k}_3|) P_{\rm lin}(|\mathbf{q}{+}\mathbf{k}_1|) + 2 \text{ perm.}\,, \tag{10.9}$$

where in T_{3311a} and T_{3221a} the line $P_{\rm lin}(k_1)$ joins the self-contracted third-order vertex to another kernel of order at least two, and no Z_1 takes the argument $\mathbf{k}_1$. For T_{3311a} this routing follows eq. (A10) of [8], as momentum conservation at $Z_3(\mathbf{q}, -\mathbf{q}, -\mathbf{k}_1)$ requires. However, eq. (68) of [72] has $P_{\rm lin}(k_2)$ there, which agrees only where $\mathbf{k}_2 = -\mathbf{k}_1$. We evaluate the four-cycle of T_{2222} in both traversal directions at weight one half, making the sum invariant under $\mathbf{k} \leftrightarrow -\mathbf{k}$ on one opposite pair of parallelogram legs. Each type reduces to one three-dimensional quadrature per configuration. Counting as for the bispectrum (Section 9) and summing over the nine types, we find 1163 signatures and 5209 shapes, both upper bounds on the number of nonvanishing coefficient functions (Supplementary Information, Sec. S7).

10.3 Contact subtraction of the self-loop types

In each of the four self-loop types one vertex carries both loop legs, $Z_3^{\rm gal}(\mathbf{q}, -\mathbf{q}, \mathbf{k}_a)$ in T_{3311a} and T_{3221a}, $Z_4^{\rm gal}(\mathbf{q}, -\mathbf{q}, \mathbf{k}_a, \mathbf{k}_b)$ in T_{4211a} and $Z_5^{\rm gal}(\mathbf{q}, -\mathbf{q}, \mathbf{k}_1, \mathbf{k}_2, \mathbf{k}_3)$ in T_{5111}. There each bias operator of order $|C|$ contributes its kernel K_O on a core C of $|C|$ legs times velocity factors on the other legs. On the core $C = (\mathbf{q}, -\mathbf{q}, \mathbf{k})$ (with $\mu = \hat{\mathbf{q}} \cdot \hat{\mathbf{k}}$) the third-order operator kernels are

$$\begin{aligned} K_{b_3}(\mathbf{q}, -\mathbf{q}, \mathbf{k}) &= \tfrac{1}{6}\,, \\ K_{b_2}(\mathbf{q}, -\mathbf{q}, \mathbf{k}) &= \tfrac{1}{3}\big[F_2(\mathbf{q}, \mathbf{k}) + F_2(-\mathbf{q}, \mathbf{k}) + F_2(\mathbf{q}, -\mathbf{q})\big] = \tfrac{2}{3}\Big(\tfrac{5}{7} + \tfrac{2}{7}\mu^2\Big)\,, \\ K_{\gamma_2^\times}(\mathbf{q}, -\mathbf{q}, \mathbf{k}) &= -\tfrac{2}{3}\,(1 - \mu^2)\,, \qquad K_{\gamma_3}(\mathbf{q}, -\mathbf{q}, \mathbf{k}) = 0\,, \end{aligned} \tag{10.10}$$

none of which depends on $|q|$, a property we call contact-flat. By contrast, a core holding only one loop leg gives a genuine P_{13}-type loop, which we keep. A contact-flat piece integrates to

$$\int \frac{d^3q}{(2\pi)^3}\, P_{\rm lin}(q)\, K_O(\hat{\mathbf{q}} \cdot \hat{\mathbf{k}}) \times (\text{the tree star of the vertex}) \;=\; \sigma^2\, \langle K_O \rangle_\mu \times (\text{the tree star})\,,$$
$$\sigma^2 = \int \frac{d^3q}{(2\pi)^3} P_{\rm lin}(q)\,, \tag{10.11}$$

the tree star being the vertex's tree-level structure with the operator replaced by b_1. The angular means $\langle K_{b_3} \rangle = \frac{1}{6}$, $\langle K_{b_2} \rangle = \frac{34}{63}$ and $\langle K_{\gamma_2^\times} \rangle = -\frac{4}{9}$, times the vertex multiplicity three, are exactly the three terms of δb_1 in Eq. (3.26): a contact-flat core only renormalizes b_1. Left in place, these contact pieces amount to 2.5 to 12.7 times the tree trispectrum and would mimic a cubic-bias signal.

Therefore we define the subtracted form of a type by zeroing, before the loop integral, the operator kernels on every core holding both loop legs. These are the tadpole $K_{b_2} = \frac{1}{2}$ for $|C| = 2$, the kernels of Eq. (10.10) for $|C| = 3$, and the lists for $|C| = 4$ and 5 in the Supplementary Information, Sec. S7. We use the subtracted forms of T_{3311a} and T_{3221a}, in which only $|C| = 2$ and $|C| = 3$ occur. We keep T_{4211a} and T_{5111} unsubtracted, with their $|C| = 4$ and $|C| = 5$ contact contributions absorbed by the renormalized couplings of the tree term as Eq. (10.11) allows, because the flatness of those two lists is established numerically rather than in closed form.

PRELIMINARY

class	structure	$\bar{n}$	$P_{\rm lin}$	parameters	renormalizes
contact $\times$ B	$[c_E]\, b\, b\, B_{[E]CD}(\mathbf{k}_{12},\mathbf{k}_3,\mathbf{k}_4)$ + 5 perm.	$\bar{n}^{-1}$	2	$[c_\delta]$, two $[c_a]$	$T_{4211b}+T_{3311b}+T_{3221b}$
double contact $\times$ P	$[d_E]\, b\, P_{[E]D}(k_4)$ + 3 perm.	$\bar{n}^{-2}$	1	$[d_\delta]$	T_{3221c}
two contacts $\times$ P	$[c_E][c_F]\, P_{[E][F]}(k_{12})$ + 2 perm.	$\bar{n}^{-2}$	1	none new	
quadruple contact	$[e_1]$	$\bar{n}^{-3}$	0	$[e_1]$	T_{2222}
total				5; 7 with P and B	

Table 5: The stochastic sector of the one-loop galaxy trispectrum at contact-term order, Eq. (10.13). Brackets denote renormalized stochastic amplitudes, b bias coefficients, $B_{[E]CD}$ and $P_{[E]D}$ the operator bispectrum and power spectrum with one stochastic contact, and $\mathbf{k}_{12}=\mathbf{k}_1+\mathbf{k}_2$. The $\bar{n}$ and $P_{\rm lin}$ columns give the power of the inverse number density and the number of linear spectra. "Parameters" lists the amplitudes each class introduces for the trispectrum alone, where the two $[c_a]$ belong to the second-order operators and the third class reuses the $[c_E]$ of the first. The last column names the contraction types of Table 4 whose stochastic contributions each amplitude renormalizes; the four self-loop types carry no stochastic amplitude: the contact parts of their self-contracted vertices are removed by the subtraction of Section 10.3, and the remainder belongs to the trispectrum counterterms, left to future work. With the power spectrum and bispectrum the joint count is $5+1+1=7$, because the pure shot amplitudes $[c_1]=P_{\rm shot}$ and $[d_1]=A_{\rm shot}$ enter again from those spectra and $[c_\delta]$ is shared with the bispectrum through $B_{\rm shot}$ of Eq. (8.5).

With $\Delta b_1=\sigma^2\,\delta b_1$ the shift generated by the removed $|C|=3$ set, the unsubtracted and subtracted forms obey, configuration by configuration,

$$T^{\rm raw}[b_1,\,b_O] \;=\; T^{\rm ren}[b_1,\,b_O] \;+\; \big(\Delta b_1+\tfrac{1}{2}b_2\,\sigma^2 f\mu_a^2\big)\,\frac{\partial T^{\rm tree}}{\partial b_1}\Big|_{\rm slot}\,, \tag{10.12}$$

where $\partial T^{\rm tree}/\partial b_1|_{\rm slot}$ is the tree star of the self-looped vertex and μ_a the line-of-sight cosine of its remaining momentum $\mathbf{k}_a$. The term $\frac{1}{2}b_2\,\sigma^2 f\mu_a^2$ is the $f\mu^2$ one-point piece of the $|C|=2$ core, the removed $K_{b_2}=\frac{1}{2}$ times the remaining leg's velocity factor, and enters separately from the shift of b_1. We have checked this identity on bin-averaged evaluations of T_{3311a} in the unsubtracted and subtracted forms: the two forms agree wherever no subtracted core contributes, and the ratios of the b_2 and $\gamma_2^\times$ shifts to the b_3 shift reproduce those of Eq. (3.26) to a relative accuracy of 4.1×10^{-7} or better (Supplementary Information, Sec. S7).

10.4 Stochastic trispectrum and its dressing

At contact-term order the stochastic four-point function of a biased tracer has four classes,

$$\begin{aligned} T_{\rm stoch} \;=\; &\sum_E [c_E]\; b\,b\; B_{[E]CD}(\mathbf{k}_{12},\mathbf{k}_3,\mathbf{k}_4) + 5\text{ perm.} \;+\; \sum_E [d_E]\; b\; P_{[E]D}(k_4) + 3\text{ perm.} \\ &+\; \sum_{E,F} [c_E][c_F]\; P_{[E][F]}(k_{12}) + 2\text{ perm.} \;+\; [e_1]\,, \end{aligned} \tag{10.13}$$

whose orders in $\bar{n}^{-1}$ and $P_{\rm lin}$ are listed in Table 5. Brackets denote renormalized stochastic amplitudes and each b a bias coefficient. The trispectrum alone has five stochastic parameters, seven counting $[c_1]=P_{\rm shot}$ and $[d_1]=A_{\rm shot}$, which already enter the power spectrum and bispectrum.

PRELIMINARY

In redshift space we dress the four classes in the noise-field formulation of [11], with the noise moments of Eq. (8.1) and the mixed field

$$\delta_g^{\rm mix}(\mathbf{k}) \;=\; \sum_n \int \prod_{i=1}^{n} \delta_1(\mathbf{q}_i) \int \epsilon(\mathbf{q}_{n+1})\; \delta_D(\mathbf{k}-\mathbf{q}_{1\cdots n+1})\; \mathcal{Z}_n(\mathbf{q}_1,\ldots,\mathbf{q}_n;\mathbf{q}_{n+1})\,, \tag{10.14}$$

whose last argument is the noise momentum, where $\mathcal{Z}_1(\mathbf{k}_1;\mathbf{k}_2) = d_1 + f k_{12z} k_{1z}/k_1^2$, $\mathcal{Z}_2(\mathbf{k}_1,\mathbf{k}_2;\mathbf{k}_3) = d_1 F_2 + f(k_{123z}k_{12z}/k_{12}^2)G_2 + (f k_{123z} d_1/2)(k_{1z}/k_1^2 + k_{2z}/k_2^2) + (f^2 k_{123z}^2/2)\, k_{1z}k_{2z}/(k_1^2 k_2^2) + d_2/2 + d_{\mathcal{G}_2}\,\mathcal{G}(\mathbf{k}_1,\mathbf{k}_2)$ and $\mathcal{Z}_n(\ldots;\mathbf{0}) = Z_n$. At leading order in k our dressing is exact. Writing (ij) for the pair of legs that carries the noise, (lm) for the other two, μ_{ij} for the line-of-sight cosine of $\mathbf{k}_{ij}$, and $\mathcal{P}_{lm} = Z_1(\mathbf{k}_l)Z_1(\mathbf{k}_m)P_{\rm lin}(k_l)P_{\rm lin}(k_m)$, the dressed classes read

$$\begin{aligned}
T_{1a}(ij) \;&=\; \frac{1}{\bar n}\Big[b_1 B_{\rm shot}^{(T)} + (1+P_{\rm shot})\, f\mu_{ij}^2\Big]\Big[2\, Z_2(\mathbf{k}_{ij},\mathbf{k}_m)\, Z_1(\mathbf{k}_m)\, P_{\rm lin}(k_{ij})\, P_{\rm lin}(k_m) + (l\leftrightarrow m)\Big]\,,\\
T_{1b}(ij) \;&=\; \frac{1+P_{\rm shot}}{\bar n}\; 2\Big[\mathcal{Z}_2(\mathbf{k}_l,\mathbf{k}_m;\mathbf{k}_i) + \mathcal{Z}_2(\mathbf{k}_l,\mathbf{k}_m;\mathbf{k}_j)\Big]\,\mathcal{P}_{lm}\,,\\
T_{1c}(ij) \;&=\; \frac{1}{\bar n}\Big\{E_{\rm shot}^{(T)} - \frac{b_1 B_{\rm shot}^{(T)}}{2}\, f\Big[\frac{k_{iz}k_{lz}}{k_l^2} + \frac{k_{jz}k_{mz}}{k_m^2}\Big] + (1+P_{\rm shot})\, f^2\, \frac{k_{iz}k_{lz}k_{jz}k_{mz}}{k_l^2 k_m^2}\Big\}\,\mathcal{P}_{lm} + (l\leftrightarrow m)\,,\\
T_2(m) \;&=\; \frac{1}{\bar n^2}\Big[D_{\rm shot}^{(T)} + A_{\rm shot}\, f\mu_m^2\Big]\, Z_1(\mathbf{k}_m)\, P_{\rm lin}(k_m)\,,\\
T_3(12|34) \;&=\; \frac{1}{\bar n^2}\Big[b_1 B_{\rm shot}^{(T)} + (1+P_{\rm shot})\, f\mu_{12}^2\Big]^2 P_{\rm lin}(k_{12})\,,\\
T_4 \;&=\; \frac{T_{\rm shot}}{\bar n^3}\,,
\end{aligned} \tag{10.15}$$

with the first class summed over the six pairs, the second over the four legs and the third over the three pairings.

The $f\mu^2$ dressings contain no free parameter. The amplitudes obey $b_1 B_{\rm shot} = 2d_1(1+P_{\rm shot})$ and $B_{\rm shot}^{(T)} = B_{\rm shot}$ when $[c_\delta]$ is shared with the bispectrum, and $E_{\rm shot}^{(T)} = d_1^2(1+P_{\rm shot})$ is exactly degenerate with the d_2 term of $\mathcal{Z}_2$, hence not independent. For a Poisson-like tracer with a modulated rate, every cumulant acquires one power of δ_g, so that $D_{\rm shot}^{(T)} = 2d_1 A_{\rm shot} + \delta_D$, the Poisson value plus a free offset δ_D (not the Dirac delta). We do not use the single-noise convention of [11], which, carried over to the trispectrum, would give $3d_1 A_{\rm shot}$ instead, a factor 3/2 above the Poisson value. By power counting a mixed one-loop stochastic contribution of the same order as $T_{\text{1-loop}}$ also exists. At $\bar n^{-1}$ it is $(1+P_{\rm shot})$ times the one-loop bispectrum topologies with one mixed-kernel leg, at $\bar n^{-2}$ it contains families with one or more mixed legs, and at $\bar n^{-3}$ it reduces to constants absorbed into $T_{\rm shot}$ and its $O(k^2)$ corrections (Supplementary Information, Sec. S7). We give only its functional form: none of its members has been evaluated, and the family with more than one mixed leg might not enter at this order, which we leave open.

10.5 Infrared bound, evaluated configurations and the covariance term

We leave the trispectrum unresummed; Eq. (7.16) bounds the omitted damping. On the parallelogram

$$(\mathbf{k}_1,\mathbf{k}_2,\mathbf{k}_3,\mathbf{k}_4) \;=\; (\mathbf{k},\,-\mathbf{k},\,\mathbf{k}',\,-\mathbf{k}')\,, \qquad k\le k'\,, \qquad x=\hat{\mathbf{k}}\cdot\hat{\mathbf{k}}'\,, \tag{10.16}$$

PRELIMINARY

the argument of $\mathrm{Cov}[\hat{P}(\mathbf{k}), \hat{P}(\mathbf{k}')]$ [66], the tree term and the one-loop types project onto the multipole covariance of Eq. (11.2). We evaluate the nine types with both moduli on the 24-point grid (spacing ratio approximately 1.15)

$$k_t \;=\; 0.01 \times 25^{\,(t-1)/23}\; h\,\mathrm{Mpc}^{-1}\,, \qquad t = 1, \ldots, 24\,, \tag{10.17}$$

giving $\binom{25}{2} = 300$ unordered pairs $k \le k'$; the eight Gauss–Legendre nodes in x on $[-1, 1]$ make $300 \times 8 = 2400$ configurations. The infrared image points differ from those of the bispectrum: pieces of the $P_{\mathrm{lin}}(q)^2$ class at the origin in T_{3311b} and T_{3221c}, a doubly-soft point in two of the three cyclic orderings of T_{2222}, and subsets of kernel arguments that sum identically to zero in T_{5111}, T_{3311a} and T_{4211b}. We quantify the quadrature error of each type by the relative difference δ_q between two quadrature depths, with no floor on the denominator and a target of 3×10^{-3}. The image points, their exponents and regulators, and the distribution of δ_q are listed in the Supplementary Information, Sec. S7. We evaluate all nine types on this grid, and report sizes at a fiducial point in Section 12 and the projection onto the power spectrum covariance in Section 11. On the binned general quadrilaterals of the trispectrum estimator, a configuration set distinct from this grid, we have evaluated T_{2222}, T_{3311a}, T_{3311b} and the subtracted forms of T_{3311a} and T_{3221a}.

On general quadrilaterals every stochastic structure above is nonvanishing. A bin $q = (a, b, c, d; K)$ contains the configurations with $\mathbf{k}_1$ to $\mathbf{k}_4$ in shells a to d and $|\mathbf{k}_1 + \mathbf{k}_2|$ in shell K. We estimate the binned connected trispectrum from the Fourier modes $\delta_{\mathbf{k}}$ on a periodic volume V by

$$\hat{T}_q \;=\; \frac{1}{V\,N_q}\Bigg[\sum_{\substack{\mathbf{k}_1\in a,\ \mathbf{k}_2\in b,\ \mathbf{k}_3\in c,\ \mathbf{k}_4\in d\\ |\mathbf{k}_1+\mathbf{k}_2|\in K}} \delta_{\mathbf{k}_1}\delta_{\mathbf{k}_2}\delta_{\mathbf{k}_3}\delta_{\mathbf{k}_4}\;\delta^{\mathrm{K}}_{\mathbf{k}_1+\mathbf{k}_2+\mathbf{k}_3+\mathbf{k}_4} \;-\; \hat{D}_q\Bigg]\,, \qquad F_q \;=\; \frac{N_q}{V}\,. \tag{10.18}$$

Here δ^{K} is the Kronecker delta, N_q the number of mode quadruples in the bin, $\hat{D}_q$ the disconnected pairings of the measured per-mode power and F_q the ideal-volume normalization (Supplementary Information, Sec. S7). At tree level we model $\hat{T}_q$ by the tree terms $T_{3111} + T_{2211}$ under the Alcock–Paczynski map of Eq. (10.5) plus the stochastic classes of Eq. (10.15), each summed over the bin as in the estimator.

11 Covariance of the power spectrum, bispectrum and trispectrum

We give the covariance of binned estimates of P_ℓ, B and T in terms of $P_{\mathrm{tot}} = b_1^2 P_{\mathrm{lin}} + 1/\bar{n}$. Apart from this shot-noise term, the mean density $\bar{n}(\mathbf{x})$ and weight $w(\mathbf{x})$ enter the covariance only through normalization moments, with no window convolution. For derivations see the Supplementary Information, Secs. S6 and S7.

11.1 Power spectrum covariance and the trispectrum term

The covariance of the multipole estimates $\hat{P}_\ell(k)$ has a Gaussian part, quadratic in P_{tot}, and a connected part, the projection of the parallelogram trispectrum $T(\mathbf{k}, -\mathbf{k}, \mathbf{k}', -\mathbf{k}'; \hat{\mathbf{n}})$ onto multipoles ℓ and ℓ'. We use the plane-parallel approximation with line of sight $\hat{\mathbf{n}}$ and neglect the window. With $\mu = \hat{\mathbf{n}} \cdot \hat{\mathbf{k}}$, $x = \hat{\mathbf{k}} \cdot \hat{\mathbf{k}}'$ and ψ the azimuth of $\hat{\mathbf{k}}'$ about $\hat{\mathbf{k}}$, the line-of-sight cosine of $\mathbf{k}'$ is

PRELIMINARY

$\mu' = \hat{\mathbf{n}}\cdot\hat{\mathbf{k}}' = x\mu + \sqrt{1-\mu^2}\sqrt{1-x^2}\cos\psi$. The projected trispectrum and its covariance term read

$$T_{\ell\ell'}(k,k',x) \;=\; \frac{(2\ell+1)(2\ell'+1)}{2}\int_{-1}^{1} d\mu \int_0^{2\pi}\frac{d\psi}{2\pi}\,\mathcal{P}_\ell(\mu)\,\mathcal{P}_{\ell'}(\mu')\,T\big(\mathbf{k},-\mathbf{k},\mathbf{k}',-\mathbf{k}';\hat{\mathbf{n}}\big)\,, \tag{11.1}$$

$$T_{\ell\ell'}(k,k') \;=\; \frac{1}{2}\int_{-1}^{1} dx\; T_{\ell\ell'}(k,k',x)\,, \qquad \mathrm{Cov}^{T}\big[P_\ell(k),P_{\ell'}(k')\big] \;=\; \frac{I_{44}}{I_{22}^2}\,T_{\ell\ell'}(k,k')\,, \tag{11.2}$$

where $\mathcal{P}_\ell$ is the Legendre polynomial and $I_{ab} = \int d^3x\,\bar{n}^a w^b$ are moments of the weighted selection (I_{22}, I_{44} being the continuum forms of $I[2,2]$, $I[4,4]$ in Eq. (8.8)). The factor I_{44}/I_{22}^2, the four-point normalization of the Feldman–Kaiser–Peacock estimator [33] (in the local approximation [75]), is the inverse of an effective volume

$$V_{\mathrm{eff}} \;=\; \frac{I_{22}^2}{I_{44}} \tag{11.3}$$

of dimension $(\mathrm{Mpc}/h)^3$. In a periodic volume $V_{\mathrm{eff}} = V$. Unlike the power spectrum estimate, which is normalized by I_{22}, the trispectrum term cannot be normalized by I_{22} alone, since T/I_{22} has dimension $(\mathrm{Mpc}/h)^{12}$ and cannot be added to a covariance of P_ℓ.

The reducible pieces of the four-point function, those with a pair sum $\mathbf{k}_a + \mathbf{k}_b \to 0$, vanish only in a periodic volume. Under a window they become the beat-coupling term, which with the local-average term forms the super-sample covariance [75], not included here. Of the nine one-loop trispectrum types, T_{2222} and T_{3221c} are summed into Cov^T here.

11.2 Bispectrum covariance and the cross block

For a Gaussian field the variance of the bispectrum monopole in a bin b follows from mode counting [63],

$$\begin{aligned}\sigma^2_{B_0}(b) \;&=\; s_{123}\,\frac{(2\pi)^6}{V_s\,V_{123}(b)}\,P_{\mathrm{tot}}(k_1)P_{\mathrm{tot}}(k_2)P_{\mathrm{tot}}(k_3) \;=\; \frac{s_{123}\,V_s\,P_{\mathrm{tot}}(k_1)P_{\mathrm{tot}}(k_2)P_{\mathrm{tot}}(k_3)}{N_{\mathrm{tri}}(b)}\,,\\ N_{\mathrm{tri}}(b) \;&=\; \frac{V_s^2\,V_{123}(b)}{(2\pi)^6}\,.\end{aligned} \tag{11.4}$$

Here V_s is the volume on which the Fourier modes are defined, $s_{123} = 6,\ 2,\ 1$ for equilateral, isosceles and scalene bins, and $N_{\mathrm{tri}}(b)$ is the number of ordered fundamental triangles in the bin with one side in each shell. We define the closure-restricted bin volume as

$$V_{123}(b) \;=\; 8\pi^2\int_b dk_1\,dk_2\,dk_3\;k_1k_2k_3\,\mathbb{1}\big[\,|k_1-k_2|\le k_3\le k_1+k_2\,\big]\,. \tag{11.5}$$

For isotropic P_{tot} and uniformly oriented triangles, the quadrupole variance is approximately $2\ell+1 = 5$ times $\sigma^2_{B_0}$.

At leading order $\mathrm{Cov}[\hat{P}_\ell,\hat{B}(b)]$ is linear in the bispectrum. With Gaussian pairings of the remaining fields [41, 63] it reads

$$\begin{aligned}\mathrm{Cov}\big[\hat{P}_\ell(k),\,\hat{B}(b)\big] \;&=\; \frac{2\,(2\ell+1)}{N_k\,N_{\mathrm{ord}}(b)}\sum_{t\in b}N_{\mathrm{fix}}(t)\,\mathrm{mult}(t)\sum_{p=1}^{3}\mathbb{1}\big[\mathrm{side}_p(t)\in k\big]\;X_p(\ell,t)\,,\\ X_p(\ell,t) \;&=\; \frac{1}{4\pi}\int d\mu_1\,d\phi\;\mathcal{P}_\ell(\mu_p)\,P_s(k_p,\mu_p)\,B_s(t;\mu_1,\phi)\,,\end{aligned} \tag{11.6}$$

PRELIMINARY

where N_k is the lattice mode count of the power spectrum shell, $N_{\rm ord}(b)$ the ordered-triangle count of the bin, $N_{\rm fix}(t)\,{\rm mult}(t)$ the exact lattice weight of side-length class t, k_p, μ_p the length and line-of-sight cosine of side p, (μ_1, ϕ) the two orientation angles of the triangle, and P_s, B_s the redshift-space spectra with shot noise kept in P_s. For a bispectrum multipole $\hat{B}_L$ the weight becomes $X_p(\ell, L, t) = \frac{2L+1}{4\pi} \int d\mu_1\, d\phi\, \mathcal{P}_\ell(\mu_p)\mathcal{P}_L(\mu_3) P_s B_s$ (μ_3 on the longest side). At tree level the three multipole pairs containing a quadrupole are correlated comparably to the monopole-monopole pair. Hence a consistent cross block should contain all four pairs $(\ell, L) \in \{0, 2\}^2$. The cross block above omits the window and beat-coupling contributions that dominate it in a survey volume.

Similarly, the Gaussian covariance of the binned trispectrum $\hat{T}_q$ of Eq. (10.18) follows from Gaussian pairings and is quartic in $P_{\rm tot}$. Our parallelogram configurations do not cover the general quadrilaterals of the $P \times T$ term in ${\rm Cov}[B, B]$. The connected $B \times B$, six-point and $P \times T$ terms of the bispectrum covariance, its non-Gaussian shot noise and super-sample response, and the non-Gaussian, window and super-sample terms of the trispectrum covariance are beyond the scope of this paper.

12 Sizes of the terms at a fiducial point

We evaluate the loop terms of the three statistics at one fiducial point in the bias couplings, the growth rate and the linear spectrum. Every loop value below is unrenormalized, with the counterterms omitted; it measures the size of one class of terms and does not describe any particular tracer.

12.1 Fiducial point and the two-loop power spectrum terms

We compute the two-loop power spectrum terms for one flat ΛCDM cosmology with $h = 0.6767$ and $\sum m_\nu = 0.1138\,{\rm eV}$ (Table 8). We evaluate them at two redshifts, $z = 0.61$ and $z = 0.2954$, with the growth rate and damping scales of that cosmology. The bispectrum and trispectrum loop integrals are contracted with one fixed linear spectrum at $z = 0.61$, set to zero above $q = 1\,h\,{\rm Mpc}^{-1}$, at the bias point

$$\begin{aligned} &b_1 = 1.8, \quad b_2 = -0.4, \quad \gamma_2 = -0.3, \quad b_3 = 0.2, \quad \gamma_2^\times = 0.15, \quad \gamma_3 = -0.1, \\ &\gamma_{21} = 0.25, \quad \gamma_{21}^\times = -0.2, \quad \gamma_{211} = 0.1, \quad \gamma_{22} = -0.15, \quad \gamma_{31} = 0.12, \quad f = 0.8\,. \end{aligned} \tag{12.1}$$

We chose this point, which is not modeled on a galaxy sample, to make every coupling contribute, and we set $f = 0.8$ independently of the fiducial cosmology. For the trispectrum we extend the point by the quartic couplings (0.08, −0.06, 0.05, −0.04) and the quintic couplings (0.03, −0.03, 0.02, −0.02, 0.02, −0.015, 0.015, −0.01, 0.01), in the operator order of Section 10.

The two-loop diagrams are not individually infrared-safe, because their soft parts cancel only in sums over diagrams. Hence single-diagram values do not estimate the two-loop correction; the components of every diagram at $k = 0.1\,h\,{\rm Mpc}^{-1}$ and $z = 0.61$, with their relative errors, can be found in the Supplementary Information, Sec. S8. With the bias coefficients applied, the loop terms amount to roughly 0.1 to 0.2 of P over $k \simeq 0.1$–$0.2\,h\,{\rm Mpc}^{-1}$ at the fiducial point.

The loop expansion is expected to hold up to the fingers-of-God scale $k_{\rm FoG}$, at which the rms line-of-sight displacement from linear velocities equals the wavelength of the mode [74],

$$k_{\rm FoG}^2\, f^2\, \sigma_v^2 \;=\; 1\,, \qquad \sigma_v^2 \;\equiv\; \frac{1}{3} \int_{\mathbf{q}} \frac{P_{\theta\theta}(q)}{q^2}\,, \tag{12.2}$$

PRELIMINARY

	T_X, finer depth, 2400 configurations [$(\mathrm{Mpc}/h)^9$]				quadrature disagreement δ_q			
type	median	min	max	fraction < 0	median	95th percentile	max	fraction $> 3 \times 10^{-3}$
T_{3311a}	2.42×10^{14}	-1.86×10^{13}	2.96×10^{16}	0.098	3.1×10^{-4}	3.2×10^{-4}	5.1×10^{-4}	0.000

Table 6: Unrenormalized one-loop trispectrum of the contraction type T_{3311a}, one of the nine types, at the bias point of Eq. (12.1) with its quartic and quintic extension, on the 2400 parallelogram configurations of the power spectrum covariance ($k \le k'$ from 0.01 to $0.25\,h\,\mathrm{Mpc}^{-1}$), contracted with the fixed $z = 0.61$ linear spectrum at one line of sight. The values are those of the unsubtracted form, which retains the σ^2 contact pieces (σ^2 times lower-order kernels). Columns 2–5 refer to the finer of two quadrature depths; δ_q (columns 6–9) is the relative disagreement between the two depths.

where $P_{\theta\theta}$ is the velocity-divergence power spectrum. The estimate of [74] is $k_{\mathrm{FoG}} \approx 0.2\,h\,\mathrm{Mpc}^{-1}$ for $z = 0$ to 0.5. With the linear spectrum for $P_{\theta\theta}$ the condition gives a higher scale, $0.30\,h\,\mathrm{Mpc}^{-1}$ for the $z = 0.57$ spectrum of [1] at $f = 0.78$, and $0.2\,h\,\mathrm{Mpc}^{-1}$ is therefore a conservative convention. A prediction beyond k_{FoG} would require a nonperturbative treatment of the small-scale velocity dispersion, which a third loop would not supply, so no claim in this paper extends past $k \sim 0.2\,h\,\mathrm{Mpc}^{-1}$. In the real-space two-loop analysis of [47] the stochastic terms set the same limit.

12.2 One-loop bispectrum and trispectrum terms

We contract all one-loop bispectrum shapes with the fixed linear spectrum on all 786 triangles for a single line of sight, $\hat{\mathbf{n}} = (0.28, -0.45, 0.848)$ relative to the triangle wavevectors. The resulting values are not multipole moments. On the equilateral configurations the self-loop topology $B_{321,\mathrm{II}}$ dominates $B_{321,\mathrm{I}}$ by two orders of magnitude at $k = 0.01\,h\,\mathrm{Mpc}^{-1}$. This hierarchy is ultraviolet in origin: approximately 99 percent of it at $k \lesssim 0.08\,h\,\mathrm{Mpc}^{-1}$ is the constant-times-P_{lin} part that renormalization absorbs into b_1, b_2 and γ_2 (Section 9.2). At the equilateral $k = 0.01\,h\,\mathrm{Mpc}^{-1}$ the tree-level B_{211} at the same couplings is $3.05 \times 10^9\,(\mathrm{Mpc}/h)^6$ and $B_{321,\mathrm{II}}$ is $-4.30 \times 10^9\,(\mathrm{Mpc}/h)^6$.

For the trispectrum we evaluate all nine contraction types on the 2400 parallelogram configurations of Section 10.5, at the extended bias point and one line of sight. Each value is computed at two quadrature depths, whose relative disagreement is δ_q. Table 6 summarizes the distribution of the values and of δ_q for one of them, T_{3311a}. The values of the bispectrum topologies $B_{321,\mathrm{I}}$ and $B_{321,\mathrm{II}}$ are given in the Supplementary Information, Sec. S6, and the distributions of the trispectrum values by type, with δ_q and the covariance projection, in Sec. S7.

13 Summary and outlook

We have constructed the two-loop power spectrum and the one-loop bispectrum and trispectrum of biased tracers in redshift space, and evaluated the loop integrals tabulated here and in the Supplementary Information. The three statistics share one bias basis complete through fifth order and one set of redshift-space kernels, and the power spectrum and bispectrum share one infrared resummation. Every tabulated two-loop component is evaluated in both double and extended precision, with its numerical error stated beside it. For the bispectrum and trispectrum the stated error is the relative difference between two quadrature depths. For the one family of two-loop kite master integrals that had only series representations we give a closed form at $d = 3$, complete

PRELIMINARY

except for two single sums (Section 5). Some of our expressions differ from printed results: relative to [60], we remove a parity-odd term from one quadratic bispectrum counterterm and include three structures absent from its printed set, all contained in the counterterm bases of [11, 25]. For the double-contact trispectrum shot-noise amplitude our reference is the Poisson value; the single-noise convention of [11] gives a larger value. The full expressions and the evaluated components with their numerical errors are given in the Supplementary Information, the power spectrum and bispectrum counterterm operators in Appendix B.

Several parts of the calculation are left open. We leave the counterterms of the one-loop trispectrum to future work, where they are to be constructed in the operator basis made consistent with the renormalization of the matter kernels [47]. The trispectrum contribution to the power spectrum covariance (on parallelogram configurations) has been summed for only two of the nine types, T_{2222} and T_{3221c}. No infrared resummation is applied to the trispectrum; the omitted correction is at most a few percent of the tree trispectrum over the band of wavenumbers containing the acoustic feature (Section 7) and can be included by using resummed linear spectra on the external legs. We include the Alcock–Paczynski map in the tree trispectrum but do not apply it to the evaluated components.

Twelve two-loop components on which the assembled power spectrum depends have not been mapped to the subtracted scheme, which removes their single-hard and double-hard limits. Two approximations have errors that we do not quantify at this order: Einstein–de Sitter growth coefficients in the two-loop components and the neglect of neutrino back-reaction on the nonlinear kernels. Below the lowest tabulated wavenumber the analytic low-k limits of Section 4 apply, and we have not extended the tabulation below it. The application of these expressions to survey data is left to future work.

One-loop analyses of redshift surveys [20, 26, 48] have so far included the two-loop galaxy term only through an estimate of its size, used to place their scale cuts. The calculation presented here can replace that estimate. Over each fitted range the k^2 counterterm has absorbed part of the omitted term, and fitting the one-loop model to the two-loop prediction shows how large that part is. In particular, fits that include the term could test the proposal of [15] that the upward shift in σ_8 found by one-loop fits at aggressive scale cuts comes from the missing two-loop term. The scale cuts of the equilateral non-Gaussianity analyses, set where the omitted term falls below the statistical error [17, 20, 23], may likewise be revisited. Including the two-loop term does not extend the range of wavenumbers over which the expansion applies, since nonperturbative velocities set that range at every loop order. Instead, it reduces the theoretical error inside that range. Because the bispectrum and trispectrum are built on the same kernels, bias parameters and stochastic terms as the power spectrum, all three statistics can be analyzed jointly at a consistent loop order once the trispectrum counterterms are constructed on the same basis. We expect the one-loop trispectrum to enter such analyses first through its contribution to the covariance of the power spectrum and bispectrum.

A Notation and conventions

We collect here the conventions of the main text, the recurring symbols, the relation of our bias coefficients to other bases and the parameters at which the loop terms are evaluated.

PRELIMINARY

A.1 Fourier, multipole and normalization conventions

We define the Fourier transform with the factor $(2\pi)^3$ in the momentum measure and abbreviate the constrained loop measures of Eq. (2.2) as

$$\begin{aligned}
&\delta(\mathbf{k}) = \int d^3x\, e^{-i\mathbf{k}\cdot\mathbf{x}}\,\delta(\mathbf{x})\,, \qquad \delta(\mathbf{x}) = \int_{\mathbf{q}} e^{i\mathbf{q}\cdot\mathbf{x}}\,\delta(\mathbf{q})\,, \qquad \int_{\mathbf{q}} \equiv \int \frac{d^3q}{(2\pi)^3}\,,\\
&\int^{\mathbf{k}}_{\mathbf{q}_1\cdots\mathbf{q}_n} \equiv \int_{\mathbf{q}_1}\cdots\int_{\mathbf{q}_n} (2\pi)^3\,\delta_D\big(\mathbf{k}-\mathbf{q}_{1\cdots n}\big)\,, \qquad \mathbf{q}_{1\cdots n}\equiv \mathbf{q}_1+\cdots+\mathbf{q}_n\,.
\end{aligned} \tag{A.1}$$

The spectra are defined with a single overall momentum-conserving delta function,

$$\begin{aligned}
\langle\delta(\mathbf{k})\,\delta(\mathbf{k}')\rangle &= (2\pi)^3\,\delta_D(\mathbf{k}+\mathbf{k}')\,P(k)\,,\\
\langle\delta(\mathbf{k}_1)\,\delta(\mathbf{k}_2)\,\delta(\mathbf{k}_3)\rangle &= (2\pi)^3\,\delta_D(\mathbf{k}_{123})\,B(\mathbf{k}_1,\mathbf{k}_2,\mathbf{k}_3)\,,\\
\langle\delta(\mathbf{k}_1)\cdots\delta(\mathbf{k}_4)\rangle_{\rm c} &= (2\pi)^3\,\delta_D(\mathbf{k}_{1234})\,T(\mathbf{k}_1,\ldots,\mathbf{k}_4)\,,
\end{aligned} \tag{A.2}$$

where the subscript c denotes the connected part. The redshift-space galaxy spectra P^s_{gg}, B^s_{ggg} and T^s_{gggg} of Eqs. (2.1), (9.1) and (10.1) follow the same normalization. Moreover, they depend on the orientation of their arguments relative to the line of sight $\hat{\mathbf{z}}$ of the distant-observer approximation. A loop term such as P_{mn} is the contribution of the correlator of the order-m and order-n fields, Wick multiplicity included, as in $P_{22} = 2\int_{\mathbf{q}}[F_2]^2 P_{\rm lin}P_{\rm lin}$ and $P_{13} = 6P_{\rm lin}\int_{\mathbf{q}} F_3 P_{\rm lin}$ of Eq. (2.13). Roman numerals, as in $P_{33,\rm I}$ and $P_{33,\rm II}$, distinguish topologies at equal orders. Throughout, $P_{\rm lin}$ denotes the linear spectrum at the redshift of evaluation, with the growth factors absorbed into the linear field.

We define the scaled velocity divergence and velocity, the two potentials, the growth rate and the direction cosines with respect to the line of sight by

$$\begin{aligned}
&\theta \equiv -\frac{\nabla\cdot\mathbf{v}}{aHf}\,, \qquad \mathbf{u} \equiv -\frac{\mathbf{v}}{aHf}\,, \qquad \nabla^2\Phi_v \equiv \theta\,, \qquad \nabla^2\Phi_\delta \equiv \delta\,,\\
&f \equiv \frac{d\ln D}{d\ln a}\,, \qquad \mu \equiv \hat{\mathbf{k}}\cdot\hat{\mathbf{z}}\,, \qquad \mu_i \equiv \hat{\mathbf{q}}_i\cdot\hat{\mathbf{z}}\,,
\end{aligned} \tag{A.3}$$

where D is the linear growth factor. With these normalizations $\theta = \delta$ and $\Phi_v = \Phi_\delta$ at linear order. The map from real space to redshift space is then $\mathbf{s} = \mathbf{x} - f u_z \hat{\mathbf{z}}$, as in Eq. (2.6). In Section 3.2 the redshift-space map is expanded with the opposite sign of the scaled velocity, $\mathbf{u} \to -\mathbf{u}$, so that there $u_z(\mathbf{q}) = iq_z\delta_1(\mathbf{q})/q^2$, $\theta = -\delta$ at linear order and the expansion generates the factors $(-ifk_z)^m$. No kernel, counterterm or evaluated loop term depends on this choice. Multipoles $P_\ell(k)$ are the projections of $P^s(k,\mu)$ onto the Legendre polynomials $\mathcal{P}_\ell(\mu)$ over $-1 \le \mu \le 1$ with weight $(2\ell+1)/2$, as in Eq. (2.17). In the kernel displays we write $x_{ij} \equiv \hat{\mathbf{q}}_i\cdot\hat{\mathbf{q}}_j$ and $\mathbf{q}_{ab} \equiv \mathbf{q}_a + \mathbf{q}_b$. The symbol $\sum_n$ denotes a sum that runs once over each of the n distinct assignments of the argument momenta to the labels of its summand. We write $\bar{\mathbf{q}}_i$ for the argument list with $\mathbf{q}_i$ removed and $\mathbf{q}_{\bar{\imath}}$ for the sum of its momenta.

We give wavenumbers in $h\,\mathrm{Mpc}^{-1}$ and power spectra in $(\mathrm{Mpc}/h)^3$. The counterterm coefficients c_0, c_2, c_4 and the subtraction constants α of Section 6 have units of $(\mathrm{Mpc}/h)^2$. The bare and pivot-subtracted forms of a single loop component differ by $\alpha\,k^2 P_{\rm lin}(k)$ (Eqs. (6.18) and (6.20)). Table 7 collects the recurring symbols.

PRELIMINARY

symbol	meaning	defined in
δ, θ, $\mathbf{u}$; Φ_δ, Φ_v	matter overdensity, scaled velocity divergence, scaled velocity; density and velocity potentials	Eq. (A.3); Section 2
δ_g, δ_g^s	galaxy overdensity in real space and in redshift space	Section 3; Eq. (2.7)
D, f, a, H	linear growth factor, growth rate, scale factor, Hubble rate	Eq. (A.3)
$P_{\rm lin}$; $P_{\rm nw}$, $P_{\rm w}$	linear spectrum at the redshift of evaluation; its smooth and oscillatory parts in the infrared resummation	Section 2; Section 7
P, B, T; P_{gg}^s, B_{ggg}^s, T_{gggg}^s	power spectrum, bispectrum, connected trispectrum; the same for galaxies in redshift space	Eqs. (A.2), (2.1), (9.1), (10.1)
P_{mn}, B_{lmn}, T_{klmn}; I, II	loop terms labeled by the orders of the paired fields, Wick multiplicity included; topologies at equal orders	Eq. (2.13); Sections 4, 9, 10
F_n, G_n; Z_n; K_n, $K_\gamma^{(n)}$	density and velocity kernels of perturbation theory; redshift-space galaxy kernels; real-space galaxy kernels and the order-n kernel of the operator with coefficient γ	Eqs. (2.4), (2.8); Section 3, Eq. (3.8)
$\mathcal{G}_2$, $\mathcal{G}_3$; Γ_3	Galileon operators of Φ_v; the cubic operator $\mathcal{G}_2(\Phi_\delta) - \mathcal{G}_2(\Phi_v)$ of the one-loop basis	Eq. (3.1); Eq. (3.5)
$\mathcal{K}$, $\mathcal{L}$; x_{ij}, $\mathbf{q}_{ab}$, $\sum_n$	momentum kernels of $\mathcal{G}_2$ and $\mathcal{G}_3$; direction cosines, momentum sums and the symmetrization sum	Eq. (3.3); this appendix
b_1, b_2, b_3, …; γ_2, $\gamma_2^\times$, γ_3, γ_{21}, …	bias coefficients: b_n multiplies δ^n with the normalization of Eq. (3.4); each γ multiplies a Galileon, a superscript $\times$ marking one further factor of δ and numerical subscripts giving the Lagrangian orders of its arguments	Eq. (3.4); Table 1
$b_{\mathcal{G}_2}$, b_{Γ_3}	coefficients of $\mathcal{G}_2(\Phi_\delta)$ and Γ_3 in the one-loop basis of [21]	Eq. (3.5)
c_0, c_2, c_4; $\tilde{c}$	counterterm coefficients multiplying $k^2 P_{\rm lin}$ at successive even powers of μ in the weighted form of Eq. (6.4), in $(\mathrm{Mpc}/h)^2$; the coefficient of the velocity-dispersion counterterm	Eqs. (6.4), (8.9), (9.14)
β_1, c_s, $b_{\nabla^2\delta}$	the combination $b_1 c_s + b_{\nabla^2\delta}$ of the dark-matter sound speed and the higher-derivative bias	Eq. (6.3)
α, α_m, k_*	subtraction constant of one component, the sum of such constants at order μ^{2m}, and the subtraction wavenumber	Eqs. (6.18), (6.20)
Σ^2, $\delta\Sigma^2$, $\bar{\Sigma}^2$, $\Sigma^2_{\rm tot}(\mu)$; r_s^d, k_S	damping scales of the infrared resummation; the drag-epoch sound horizon at which they are evaluated and the separation scale of the long-short split	Eq. (7.8); Section 7
$\hat{\mathbf{z}}$, μ, μ_i; $\mathcal{P}_\ell$, P_ℓ	line of sight and direction cosines; Legendre polynomials and multipoles	Eqs. (A.3), (2.17)
S_n, $\mathbf{T}_n$, $\mathbf{L}_n$; $\mathbf{W}$	longitudinal and transverse Lagrangian displacement kernels and the displacement vector kernel, in the conventions of [47]; the vector kernel from which $\mathbf{T}_3$ is built	Section 3

Table 7: Recurring symbols, their meaning in words and the place where each is defined. Loop momenta are denoted $\mathbf{q}$ or $\mathbf{q}_i$ and external momenta $\mathbf{k}$ or $\mathbf{k}_i$. A superscript s marks redshift space and a subscript g the galaxy field.

A.2 Dictionary and fiducial parameters

The bias coefficients b_1, b_2 and $\gamma_2 = b_{\mathcal{G}_2}$ equal their counterparts in the one-loop basis of [21], and γ_{21} is related to $b_{\mathcal{G}_2}$ and b_{Γ_3} of that basis by Eq. (3.5). For bases whose quadratic bias operators are $\delta^2/2$ and the squared traceless tidal field s^2 built from Φ_δ, with coefficients that we denote b_2^E and b_s^E, the second-order identity $\mathcal{G}_2 = s^2 - \frac{2}{3}\,\delta^2$ gives $b_s^E = \gamma_2$ and $b_2 = b_2^E + \frac{4}{3}\,b_s^E$. The counterterm coefficient $c_0 = -\beta_1$ of Eq. (6.3) is neither the coefficient c_0 of the higher-derivative terms $P_0^{\rm HD}, \ldots, P_7^{\rm HD}$ of [47] nor the constant trace term of the composite velocity operator of that reference. That trace term is fixed by the one-point renormalization of the operator and is not a free parameter. The remaining relations between our basis and the bases of [47] and [21], including the Lagrangian displacement conventions used for S_n, $\mathbf{T}_n$ and S_4, are given in the Supplementary Information, Sec. S1.

Table 8 lists the cosmological parameters, redshifts, growth rates and bias couplings at which

PRELIMINARY

quantity	symbol	value
Cosmology of the fiducial linear spectrum for which the loop terms are evaluated		
dimensionless Hubble rate	h	0.6767
neutrino mass sum	$\sum m_\nu$	0.1138 eV
baryon and cold-matter densities, tilt, amplitude	ω_b, ω_c, n_s, A_s	held fixed at the same fiducial point
Redshifts of evaluation and growth rates		
first redshift (two-loop power-spectrum components and damping scales)	z	0.61
second redshift (two-loop power-spectrum components and damping scales)	z	0.2954
growth rate of this cosmology at $z = 0.61$ from the growth equation	f	0.7879
growth rate used in the infrared-damped input spectrum at $z = 0.61$	f	0.7926
growth rate used in the infrared-damped input spectrum at $z = 0.2954$	f	0.6811
Bias point at which the bispectrum and trispectrum sizes are evaluated		
linear, quadratic, cubic density biases	b_1, b_2, b_3	1.8, −0.4, 0.2
Galileon biases	γ_2, $\gamma_2^\times$, γ_3	−0.3, 0.15, −0.1
nonlocal-in-time biases	γ_{21}, $\gamma_{21}^\times$, γ_{211}, γ_{22}, γ_{31}	0.25, −0.2, 0.1, −0.15, 0.12
growth rate used with this bias point	f	0.8

Table 8: Parameters held fixed in evaluating the loop components, the damping scales and the bispectrum and trispectrum sizes. The linear spectrum is that of the clustering species (cold dark matter plus baryons) in a single cosmology with massive neutrinos, evaluated at the two listed redshifts. The sizes of the two-loop power-spectrum components are quoted at the first redshift, with no bias coefficients or powers of f applied. The bias point, Eq. (12.1), is chosen to make every term of the bispectrum and trispectrum models contribute, and it is not meant to resemble a real galaxy sample. For the trispectrum sizes it is supplemented by the small quartic and quintic couplings listed in Section 12.

Notes: Each infrared-damped input spectrum is evaluated with the growth rate given in its own row; the growth-equation value refers to the clustering species alone and does not include the massive neutrinos; the growth rate listed with the bias point is one of the couplings that define that point and is unrelated to the growth rates of the other rows.

we evaluate the loop terms of the power spectrum, the infrared damping scales and the bispectrum and trispectrum sizes.

B Counterterm operator lists

In this appendix we list the counterterm operators of the two-loop power spectrum and the one-loop bispectrum of galaxies in redshift space. For each coefficient we state whether it is a free parameter, is fixed by the renormalization conditions of Section 6.3, or equals a power-spectrum coefficient. We omit the stochastic terms, which are not counterterms in this sense, and set $k_{\rm NL} = 0.45\,h\,{\rm Mpc}^{-1}$ throughout.

B.1 Power spectrum counterterms at two loops

We list the structures in Table 9. At order $k^2 P_{\rm lin}$ the redshift-space map generates at every loop order the structure $2(b_1 + f\mu^2)(c_0 + c_2\mu^2 + c_4\mu^4)\,k^2 P_{\rm lin}$ of Eq. (6.4), which reaches μ^6. Its coefficients c_0, c_2, c_4 are free. Here $c_0 = -\beta_1 = -(b_1 c_s + b_{\nabla^2\delta})$ (in $({\rm Mpc}/h)^2$), with c_s the dark-matter sound speed and $b_{\nabla^2\delta}$ the pure higher-derivative bias. The seven coefficients $\alpha_0, \ldots, \alpha_6$ of the scheme polynomial are subtraction constants and add no counterterm. At two loops β_1 also multiplies the one-loop spectrum, forming the class $\beta_1 k^2 P_{\text{1-loop}}$, and $k^4 P_{\rm lin}$ terms appear [47], which in redshift space include the velocity-dispersion term $\tilde{c}$. The subleading single-hard terms of the two-loop

PRELIMINARY

structure	coefficients	status
$2(b_1+f\mu^2)(c_0+c_2\mu^2+c_4\mu^4)\,k^2P_{\rm lin}$, Eq. (6.4)	c_0, c_2, c_4	free; $c_0=-(b_1c_s+b_{\nabla^2\delta})$
$\beta_1\,k^2P_{\text{1-loop}}$	$\beta_1=-c_0$	no new coefficient; μ structure not constructed here
$k^4P_{\rm lin}$ terms, including the $\tilde{c}$ term of Eq. (9.14)	$\tilde{c}$ and the k^4 coefficients	free; μ structure not constructed here
scheme polynomial $k^2P_{\rm lin}\sum_{m=0}^{6}\alpha_m\mu^{2m}$, Eq. (6.20)	$\alpha_0,\ldots,\alpha_6$	scheme constants, not counterterms
$\nabla^2\delta$; the four quadratic and the cubic local higher-derivative operators of [47]	$b_{\nabla^2\delta}$; $\beta_{2,1\ldots4}$; $\beta_{3,i}$	free; on the real-space two-loop spectrum they enter through $P_0^{\rm HD},\ldots,P_7^{\rm HD}$
coupling shifts δb_1, δb_2, $\delta\gamma_2$, …, Eqs. (6.7)–(6.9) and Section 6.3	exact rationals in the bare couplings	fixed by the renormalization conditions
unit operator	$\langle\delta_g\rangle=0$	fixed; removes the composite means and their $f\mu^2P_{\rm lin}$ image

Table 9: Counterterm structures of the redshift-space galaxy power spectrum at two loops. "Free" marks an independent coefficient of the effective theory and "fixed" a quantity determined by the renormalization conditions. The higher-derivative operators are local in the sense that they contain no inverse Laplacian acting on a product of fields. The stochastic terms are not listed.

integrals, weighted by σ^2_{-2} (Eq. (6.5)), carry fixed coefficients and add no counterterm.

Through cubic order the local higher-derivative bias operators are those of [47], $\nabla^2\delta$ with coefficient $b_{\nabla^2\delta}$, four quadratic operators with coefficients $\beta_{2,i}$ and the cubic operators with coefficients $\beta_{3,i}$, which enter the real-space two-loop power spectrum through the eight shapes $P_0^{\rm HD},\ldots,P_7^{\rm HD}$ of that reference. The coupling shifts δb_1, δb_2, $\delta\gamma_2$ and their fifth-order counterparts that absorb the σ^2 hard limits are exact rationals in the bare couplings, and we do not vary them. Finally, the mean of the composite operators, whose image under the velocity map is an $f\mu^2P_{\rm lin}$ term, is removed by the condition $\langle\delta_g\rangle=0$.

B.2 Bispectrum counterterms

The one-loop bispectrum counterterm of Eq. (9.9) is bilinear in the linear spectrum and contains two counterkernels, whose structures we collect in Table 10. The real-space kernel $F_2^{\rm ctr}$ is a sum of five shapes, $(k_1^2+k_2^2)F_2$, $k_3^2F_2$, $(k_1^2+k_2^2)\,\kappa$, $k_3^2\,\kappa$ and $\mathbf{k}_1\cdot\mathbf{k}_2$ with $\kappa=(\hat{\mathbf{k}}_1\cdot\hat{\mathbf{k}}_2)^2-1$, each over $k^2_{\rm NL}$ with coefficients $\beta_{B,a},\ldots,\beta_{B,e}$ in that order [32, 60]. The redshift-space kernel $Z_2^{\rm ctr}$ is the sum of eleven structures $R_1,\ldots,R_{11}$ in $k_{3z}=k_3\mu_3$, the μ_i and f, each over $k^2_{\rm NL}$. They are the line-of-sight contact operators of the renormalized composites $[(1+\delta_g)u_z^m]_R$, $m=1,\ldots,4$, of the redshift-space map, together with the nonlocal velocity counterterm e_5 [11, 25].

Eight of the eleven redshift-space structures are those of eq. (2.12) of [60], $R_1,\ldots,R_5=C_1,\ldots,C_5$ and $R_6,R_7,R_8=C_7,C_8,C_9$. However, the C_6 given there is odd under the line-of-sight reflection, and its corrected form $C_8-\frac{1}{3}C_7$ is not an independent direction. The remaining three are $R_9=C_{10}$, $R_{10}=C_{11}$ and $R_{11}=e_5$ of Section 9.2. The first two, from $\delta\,s_{ij}$ and $s_{ij}\partial_j\delta$ at order f^0, complete the local contact space at $O(k^2\delta^2)$, which at fixed f is ten-dimensional and spanned by $R_1,\ldots,R_{10}$. The third, the longitudinal projection $\partial_z\partial_i\partial_j\nabla^{-2}$ of the tidal-squared tensor, is the only direction that the velocity counterterm adds to the local contact space. All eleven coefficients are free, and in particular we do not impose the two relations among C_1, C_2 and

PRELIMINARY

symbol	structure	origin	status
$\beta_{B,a},\dots,\beta_{B,e}$	$(k_1^2{+}k_2^2)F_2$, $k_3^2F_2$, $(k_1^2{+}k_2^2)\kappa$, $k_3^2\kappa$, $\mathbf{k}_1{\cdot}\mathbf{k}_2$, each over $k_{\rm NL}^2$	real space, $F_2^{\rm ctr}$ [32]	free (5)
$R_1,\dots,R_5$	$C_1,\dots,C_5$ of eq. (2.12) of [60]	contact operators of $[(1+\delta_g)u_z^m]_R$, $m=1,\dots,4$	free
R_6, R_7, R_8	C_7, C_8, C_9 of eq. (2.12) of [60]	as above	free
$R_9 = C_{10}$	$k_{3z}^2(\mu_1^2+\mu_2^2-\frac{2}{3})$, Eq. (9.11)	$\delta\, s_{ij}$ at the second composite level, f^0	free
$R_{10} = C_{11}$	Eq. (9.12)	$s_{ij}\partial_j\delta$ at the first composite level, f^0	free
$R_{11} = e_5$	$k_{3z}^2(\mathbf{k}_1\cdot\mathbf{k}_2)(\mathbf{k}_1\cdot\mathbf{k}_3)(\mathbf{k}_2\cdot\mathbf{k}_3)/(k_1^2k_2^2k_3^2)$, Eq. (9.13)	longitudinal-projection velocity counterterm [11, 25]	free
(none)	C_6 of [60]; corrected form $C_8-\frac{1}{3}C_7$, Eq. (9.10)	parity-odd as given there; redundant once corrected	omitted
$\tilde{c}$	$-\frac{\tilde{c}}{2}\,(k^4/k_{\rm NL}^4)\,\mu^4 f^4(b_1+f\mu^2)$ in $Z_1^{\rm ctr}$, Eq. (9.14)	velocity dispersion [11]	free; shared with the power spectrum
c_0, c_2, c_4 in $B_{\rm ctr,II}$	$Z_1^{\rm ctr}$ on an external leg, Eq. (9.15)	power spectrum, Eq. (6.4)	equal to the power-spectrum coefficients; shifts $\delta c_{0,2,4}$ of Eq. (9.16) fixed
c_0 image	second-order image of $k^2\delta$ in $Z_2^{\rm gal}$	the map acting on $K_1 = b_1 + c_0q^2$	equal to the power-spectrum c_0
δb_1, δb_2, $\delta\gamma_2$	σ^2 tadpoles of $B_{321,\rm II}$, B_{411}	Eqs. (6.7)–(6.9)	fixed by the renormalization conditions

Table 10: Counterterm structures of the one-loop galaxy bispectrum in redshift space. The upper rows list the 17 free coefficients ($5+11$ plus $\tilde{c}$): five real-space shapes, eleven redshift-space contact structures and the velocity-dispersion term. The lower rows give the structures whose coefficients are those of the power spectrum or are fixed by the renormalization conditions. Here $\kappa = (\hat{\mathbf{k}}_1\cdot\hat{\mathbf{k}}_2)^2-1$, $k_{3z}=k_3\mu_3$ with μ_i the cosine of $\mathbf{k}_i$ with the line of sight, and $k_{\rm NL}=0.45\,h\,{\rm Mpc}^{-1}$.

C_5 that the power spectrum implies in principle. In total, the bispectrum counterterms have 17 free coefficients: five for the real-space shapes, eleven for the redshift-space structures that replace the nine of [60], and the velocity-dispersion coefficient $\tilde{c}$.

Two further groups of terms take their coefficients from the power spectrum and add no parameter. In $B_{\rm ctr,II}$ we insert the first-order counterkernel with the power-spectrum c_0, c_2, c_4 on an external leg of the tree. The shifts that the loop leg of $B_{321,\rm II}$ induces on these coefficients are exactly the P_{13} shifts of the power spectrum. Thus the same renormalized c_0, c_2, c_4 enter both statistics. The kernel $Z_2^{\rm gal}$ also contains the second-order image of the $k^2\delta$ operator, generated by the map from $K_1 = b_1 + c_0q^2$ with the power-spectrum c_0 and no additional contact structure. We remove the σ^2 tadpoles of the self-loop classes $B_{321,\rm II}$ and B_{411} with the same constants δb_1, δb_2, $\delta\gamma_2$ that renormalize the power spectrum, and the renormalized bias parameters are therefore common to the two statistics.

Acknowledgments

Funding for this project was provided by Anthropic. This is not an official Anthropic project and results and views are not endorsed by Anthropic.

PRELIMINARY

References

[1] C. Anastasiou, A. Favorito, M. Lewandowski, L. Senatore and H. Zheng, "Efficient evaluation of the dark-matter two-loop power spectrum in the EFT of LSS," arXiv:2509.05187.

[2] V. Assassi, D. Baumann, D. Green and M. Zaldarriaga, "Renormalized Halo Bias," JCAP **08** (2014) 056, arXiv:1402.5916.

[3] F. Bernardeau, S. Colombi, E. Gaztañaga and R. Scoccimarro, "Large-scale structure of the Universe and cosmological perturbation theory," Phys. Rept. **367** (2002) 1, astro-ph/0112551.

[4] D. Blas, M. Garny and T. Konstandin, "On the non-linear scale of cosmological perturbation theory," JCAP **09** (2013) 024, arXiv:1304.1546.

[5] T. Bakx, M. Garny, H. Rubira and Z. Vlah, "Galaxy bias renormalization: Two-loop Power Spectrum, One-loop Trispectrum and Bispectrum," arXiv:2606.31280.

[6] T. Baldauf, L. Mercolli and M. Zaldarriaga, "Effective field theory of large scale structure at two loops: The apparent scale dependence of the speed of sound," Phys. Rev. D **92** (2015) 123007, arXiv:1507.02256.

[7] D. Baumann, A. Nicolis, L. Senatore and M. Zaldarriaga, "Cosmological non-linearities as an effective fluid," JCAP **07** (2012) 051, arXiv:1004.2488.

[8] D. Bertolini, K. Schutz, M. P. Solon, J. R. Walsh and K. M. Zurek, "Non-Gaussian Covariance of the Matter Power Spectrum in the Effective Field Theory of Large Scale Structure," Phys. Rev. D **93** (2016) 123505, arXiv:1512.07630.

[9] D. Bertolini, K. Schutz, M. P. Solon and K. M. Zurek, "The Trispectrum in the Effective Field Theory of Large Scale Structure," JCAP **06** (2016) 052, arXiv:1604.01770.

[10] I. Bierenbaum and S. Weinzierl, "The massless two-loop two-point function," Eur. Phys. J. C **32** (2003) 67, hep-ph/0308311.

[11] T. Bakx, M. M. Ivanov, O. H. E. Philcox and Z. Vlah, "One-Loop Galaxy Bispectrum: Consistent Theory, Efficient Analysis with COBRA, and Implications for Cosmological Parameters," Phys. Rev. D **114** (2026) 063532, arXiv:2507.22110. Equation numbers refer to arXiv version 5.

[12] N. N. Bogoliubow and O. S. Parasiuk, "Über die Multiplikation der Kausalfunktionen in der Quantentheorie der Felder," Acta Math. **97** (1957) 227.

[13] J. J. M. Carrasco, S. Foreman, D. Green and L. Senatore, "The Effective Field Theory of Large Scale Structures at two loops," JCAP **07** (2014) 057, arXiv:1310.0464.

[14] J. J. M. Carrasco, M. P. Hertzberg and L. Senatore, "The effective field theory of cosmological large scale structures," JHEP **09** (2012) 082, arXiv:1206.2926.

[15] A. Chudaykin, M. M. Ivanov and T. Nishimichi, "Priors and scale cuts in EFT-based full-shape analyses," Phys. Rev. D **113** (2026) 063524, arXiv:2410.16358.

PRELIMINARY

[16] A. Chudaykin, M. M. Ivanov and O. H. E. Philcox, "Reanalyzing DESI DR1. I. ΛCDM constraints from the power spectrum and bispectrum," Phys. Rev. D **113** (2026) 063502, arXiv:2507.13433.

[17] G. Cabass, M. M. Ivanov, O. H. E. Philcox, M. Simonović and M. Zaldarriaga, "Constraints on Single-Field Inflation from the BOSS Galaxy Survey," Phys. Rev. Lett. **129** (2022) 021301, arXiv:2201.07238.

[18] J. J. M. Carrasco, S. Foreman, D. Green and L. Senatore, "The 2-loop matter power spectrum and the IR-safe integrand," JCAP **07** (2014) 056, arXiv:1304.4946.

[19] E. Castorina, E. Sefusatti, R. K. Sheth, F. Villaescusa-Navarro and M. Viel, "Cosmology with massive neutrinos II: on the universality of the halo mass function and bias," JCAP **02** (2014) 049, arXiv:1311.1212.

[20] A. Chudaykin, M. M. Ivanov and O. H. E. Philcox, "Reanalyzing DESI DR1. III. Constraints on inflation from galaxy power spectra and bispectra," Phys. Rev. D **113** (2026) 063552, arXiv:2512.04266.

[21] A. Chudaykin, M. M. Ivanov, O. H. E. Philcox and M. Simonović, "Nonlinear perturbation theory extension of the Boltzmann code `CLASS`," Phys. Rev. D **102** (2020) 063533, arXiv:2004.10607.

[22] M. D. Schwartz, M. M. Ivanov and S. Mishra-Sharma, "KITE: a two-loop galaxy clustering pipeline at stated precision," companion paper (Paper II), in preparation.

[23] G. D'Amico, M. Lewandowski, L. Senatore and P. Zhang, "Limits on primordial non-Gaussianities from BOSS galaxy-clustering data," Phys. Rev. D **111** (2025) 063514, arXiv:2201.11518.

[24] G. D'Amico, Y. Donath, M. Lewandowski, L. Senatore and P. Zhang, "The BOSS bispectrum analysis at one loop from the Effective Field Theory of Large-Scale Structure," JCAP **05** (2024) 059, arXiv:2206.08327.

[25] G. D'Amico, Y. Donath, M. Lewandowski, L. Senatore and P. Zhang, "The one-loop bispectrum of galaxies in redshift space from the Effective Field Theory of Large-Scale Structure," JCAP **07** (2024) 041, arXiv:2211.17130.

[26] G. D'Amico, J. Gleyzes, N. Kokron, K. Markovic, L. Senatore, P. Zhang, F. Beutler and H. Gil-Marín, "The cosmological analysis of the SDSS/BOSS data from the Effective Field Theory of Large-Scale Structure," JCAP **05** (2020) 005, arXiv:1909.05271.

[27] S. E. Derkachev, A. V. Ivanov and L. A. Shumilov, "Mellin–Barnes Transformation for Two-Loop Master-Diagram," J. Math. Sci. **264** (2022) 298, arXiv:2303.09203.

[28] V. Desjacques, D. Jeong and F. Schmidt, "Large-Scale Galaxy Bias," Phys. Rept. **733** (2018) 1, arXiv:1611.09787.

[29] Y. Donath, M. Lewandowski and L. Senatore, "Direct signatures of the formation time of galaxies," Phys. Rev. D **109** (2024) 123510, arXiv:2307.11409.

PRELIMINARY

[30] Y. Donath and L. Senatore, "Biased Tracers in Redshift Space in the EFTofLSS with exact time dependence," JCAP **10** (2020) 039, arXiv:2005.04805.

[31] A. Aviles, A. Banerjee, G. Niz and Z. Slepian, "Clustering in Massive Neutrino Cosmologies via Eulerian Perturbation Theory," JCAP **11** (2021) 028, arXiv:2106.13771.

[32] A. Eggemeier, R. Scoccimarro and R. E. Smith, "Bias Loop Corrections to the Galaxy Bispectrum," Phys. Rev. D **99** (2019) 123514, arXiv:1812.03208.

[33] H. A. Feldman, N. Kaiser and J. A. Peacock, "Power-spectrum analysis of three-dimensional redshift surveys," Astrophys. J. **426** (1994) 23, astro-ph/9304022.

[34] P. Bansal, A. Aviles, H. E. Noriega, C. Guandalin, I. Garzon, G. Niz, M. S. Wang, *et al.*, "FolpsD: combining EFT and phenomenological approaches for joint power spectrum and bispectrum analyses," arXiv:2604.08895.

[35] M. H. Goroff, B. Grinstein, S.-J. Rey and M. B. Wise, "Coupling of modes of cosmological mass density fluctuations," Astrophys. J. **311** (1986) 6.

[36] M. Garny and P. Taule, "Loop corrections to the power spectrum for massive neutrino cosmologies with full time- and scale-dependence," JCAP **01** (2021) 020, arXiv:2008.00013.

[37] M. Garny and P. Taule, "Two-loop power spectrum with full time- and scale-dependence and EFT corrections: impact of massive neutrinos and going beyond EdS," JCAP **09** (2022) 054, arXiv:2205.11533.

[38] R. W. Gosper, Jr., "Decision procedure for indefinite hypergeometric summation," Proc. Nat. Acad. Sci. **75** (1978) 40.

[39] A. G. Grozin, "Massless two-loop self-energy diagram: Historical review," Int. J. Mod. Phys. A **27** (2012) 1230018, arXiv:1206.2572.

[40] D. Gualdi, H. Gil-Marín and L. Verde, "Joint analysis of anisotropic power spectrum, bispectrum and trispectrum: application to N-body simulations," JCAP **07** (2021) 008, arXiv:2104.03976.

[41] D. Gualdi and L. Verde, "Galaxy redshift-space bispectrum: the Importance of Being Anisotropic," JCAP **06** (2020) 041, arXiv:2003.12075.

[42] D. Gualdi and L. Verde, "Integrated trispectrum detection from BOSS DR12 NGC CMASS," JCAP **09** (2022) 050, arXiv:2201.06932.

[43] M. Hartmeier and M. Garny, "Minimal Basis for Exact Time Dependent Kernels in Cosmological Perturbation Theory and Application to ΛCDM and w_0w_aCDM," JCAP **12** (2023) 027, arXiv:2308.06096.

[44] K. Hepp, "Proof of the Bogoliubov–Parasiuk theorem on renormalization," Commun. Math. Phys. **2** (1966) 301.

[45] M. M. Ivanov, O. H. E. Philcox, T. Nishimichi, M. Simonović, M. Takada and M. Zaldarriaga, "Precision analysis of the redshift-space galaxy bispectrum," Phys. Rev. D **105** (2022) 063512, arXiv:2110.10161.

PRELIMINARY

[46] M. M. Ivanov, J. M. Sullivan, R. de Belsunce, S.-F. Chen, A. Chudaykin, M. Maus and O. H. E. Philcox, "Reanalyzing DESI DR1: IV. Percent-level cosmological constraints from combined probes and robust evidence for the normal neutrino mass hierarchy," Phys. Rev. D **114** (2026) 063526, arXiv:2601.16165.

[47] M. M. Ivanov, "Galaxy Power Spectrum at Two-Loop Order: Implications for Weak Lensing Surveys and New Physics," arXiv:2606.30713, MIT-CTP/6054. Equation numbers refer to arXiv version 2 (15 September 2026).

[48] M. M. Ivanov, M. Simonović and M. Zaldarriaga, "Cosmological parameters from the BOSS galaxy power spectrum," JCAP **05** (2020) 042, arXiv:1909.05277.

[49] M. M. Ivanov and S. Sibiryakov, "Infrared Resummation for Biased Tracers in Redshift Space," JCAP **07** (2018) 053, arXiv:1804.05080.

[50] N. Kaiser, "Clustering in real space and in redshift space," Mon. Not. Roy. Astron. Soc. **227** (1987) 1.

[51] Y. Kobayashi, "Fast computation of the non-Gaussian covariance of redshift-space galaxy power spectrum multipoles," Phys. Rev. D **108** (2023) 103512, arXiv:2308.08593.

[52] A. V. Kotikov, "The Gegenbauer Polynomial technique: the evaluation of a class of Feynman diagrams," Phys. Lett. B **375** (1996) 240, hep-ph/9512270.

[53] M. Lewandowski and L. Senatore, "IR-safe and UV-safe integrands in the EFTofLSS with exact time dependence," JCAP **08** (2017) 037, arXiv:1701.07012.

[54] N. Makino, M. Sasaki and Y. Suto, "Analytic approach to the perturbative expansion of nonlinear gravitational fluctuations in cosmological density and velocity fields," Phys. Rev. D **46** (1992) 585.

[55] S. V. Mikhailov and N. Volchanskiy, "Two-loop kite master integral for a correlator of two composite vertices," JHEP **01** (2019) 202, arXiv:1812.02164.

[56] P. McDonald and A. Roy, "Clustering of dark matter tracers: generalizing bias for the coming era of precision LSS," JCAP **08** (2009) 020, arXiv:0902.0991.

[57] A. Edison, M. Lewandowski and L. Senatore, "Non-local-in-time structure formation and sixth-order galaxy bias," arXiv:2512.19578.

[58] A. Oddo, E. Sefusatti, C. Porciani, P. Monaco and A. G. Sánchez, "Toward a robust inference method for the galaxy bispectrum: likelihood function and model selection," JCAP **03** (2020) 056, arXiv:1908.01774.

[59] T. Bakx, M. Garny, H. Rubira and Z. Vlah, "Two-loop renormalization and running of galaxy bias," JCAP **03** (2026) 056, arXiv:2507.13905.

[60] O. H. E. Philcox, M. M. Ivanov, G. Cabass, M. Simonović, M. Zaldarriaga and T. Nishimichi, "Cosmology with the Redshift-Space Galaxy Bispectrum Monopole at One-Loop Order," Phys. Rev. D **106** (2022) 043530, arXiv:2206.02800.

PRELIMINARY

[61] A. Perko, L. Senatore, E. Jennings and R. H. Wechsler, "Biased Tracers in Redshift Space in the EFT of Large-Scale Structure," arXiv:1610.09321.

[62] R. Scoccimarro, H. M. P. Couchman and J. A. Frieman, "The Bispectrum as a Signature of Gravitational Instability in Redshift-Space," Astrophys. J. **517** (1999) 531, astro-ph/9808305.

[63] E. Sefusatti, M. Crocce, S. Pueblas and R. Scoccimarro, "Cosmology and the Bispectrum," Phys. Rev. D **74** (2006) 023522, astro-ph/0604505.

[64] N. S. Sugiyama, S. Saito, F. Beutler and H.-J. Seo, "A complete FFT-based decomposition formalism for the redshift-space bispectrum," Mon. Not. Roy. Astron. Soc. **484** (2019) 364, arXiv:1803.02132.

[65] N. S. Sugiyama, S. Saito, F. Beutler and H.-J. Seo, "Perturbation theory approach to predict the covariance matrices of the galaxy power spectrum and bispectrum in redshift space," Mon. Not. Roy. Astron. Soc. **497** (2020) 1684, arXiv:1908.06234.

[66] R. Scoccimarro, M. Zaldarriaga and L. Hui, "Power Spectrum Correlations Induced by Non-Linear Clustering," Astrophys. J. **527** (1999) 1, astro-ph/9901099.

[67] F. Schmidt, "Sigma-Eight at the Percent Level: The EFT Likelihood in Real Space," JCAP **04** (2021) 032, arXiv:2009.14176.

[68] R. Scoccimarro and J. Frieman, "Loop Corrections in Non-Linear Cosmological Perturbation Theory," Astrophys. J. Suppl. **105** (1996) 37, astro-ph/9509047.

[69] L. Senatore, "Bias in the Effective Field Theory of Large Scale Structures," JCAP **11** (2015) 007, arXiv:1406.7843.

[70] L. Senatore and M. Zaldarriaga, "The IR-resummed Effective Field Theory of Large Scale Structures," JCAP **02** (2015) 013, arXiv:1404.5954.

[71] M. Simonović, T. Baldauf, M. Zaldarriaga, J. J. Carrasco and J. A. Kollmeier, "Cosmological perturbation theory using the FFTLog: formalism and connection to QFT loop integrals," JCAP **04** (2018) 030, arXiv:1708.08130.

[72] T. Steele and T. Baldauf, "Precise Calibration of the One-Loop Trispectrum in the Effective Field Theory of Large Scale Structure," Phys. Rev. D **103** (2021) 103518, arXiv:2101.10289.

[73] D. Blas, M. Garny, M. M. Ivanov and S. Sibiryakov, "Time-Sliced Perturbation Theory II: Baryon Acoustic Oscillations and Infrared Resummation," JCAP **07** (2016) 028, arXiv:1605.02149.

[74] P. Taule and M. Garny, "The two-loop power spectrum in redshift space," JCAP **11** (2023) 078, arXiv:2308.07379.

[75] D. Wadekar and R. Scoccimarro, "Galaxy power spectrum multipoles covariance in perturbation theory," Phys. Rev. D **102** (2020) 123517, arXiv:1910.02914.

[76] D. Zeilberger, "The method of creative telescoping," J. Symb. Comput. **11** (1991) 195.

[77] W. Zimmermann, "Convergence of Bogoliubov's method of renormalization in momentum space," Commun. Math. Phys. **15** (1969) 208.

PRELIMINARY